



저작자표시-비영리-변경금지 2.0 대한민국

이용자는 아래의 조건을 따르는 경우에 한하여 자유롭게

- 이 저작물을 복제, 배포, 전송, 전시, 공연 및 방송할 수 있습니다.

다음과 같은 조건을 따라야 합니다:



저작자표시. 귀하는 원저작자를 표시하여야 합니다.



비영리. 귀하는 이 저작물을 영리 목적으로 이용할 수 없습니다.



변경금지. 귀하는 이 저작물을 개작, 변형 또는 가공할 수 없습니다.

- 귀하는, 이 저작물의 재이용이나 배포의 경우, 이 저작물에 적용된 이용허락조건을 명확하게 나타내어야 합니다.
- 저작권자로부터 별도의 허가를 받으면 이러한 조건들은 적용되지 않습니다.

저작권법에 따른 이용자의 권리는 위의 내용에 의하여 영향을 받지 않습니다.

이것은 [이용허락규약\(Legal Code\)](#)을 이해하기 쉽게 요약한 것입니다.

[Disclaimer](#)

공학박사학위논문

# Synthesis of Functional Nanoparticles Using Flame Metal Combustion and Spark Discharge Method

화염금속연소법과 스파크 방전법을 이용한  
기능성 나노입자 합성

2016 년 2 월

서울대학교 대학원

기계항공공학부

채 석 병



# 화염금속연소법과 스파크방전법을 이용한 기능성 나노입자 합성

Synthesis of Functional Nanoparticles Using Flame  
Metal Combustion and Spark Discharge Method

지도교수 최 만 수

이 논문을 공학박사 학위논문으로 제출함

2015년 11월

서울대학교 대학원  
기계항공공학부  
채 석 병

채석병의 공학박사 학위논문을 인준함

2015년 12월

위원장 : 이 준 식 (인)

부위원장 : 최 만 수 (인)

위원 : 전 누 리

위원 : 고 승 환

위원 : 김 형 철





# **Synthesis of Functional Nanoparticles Using Flame Metal Combustion and Spark Discharge Method**

Sukbyung Chae

Department of Mechanical and Aerospace Engineering

The Graduate School

Seoul National University

## **Abstract**

Nanoparticles with unique properties have been widely studied and synthesizing methods of nanomaterials have been one of the main research field of nanotechnology. Various functional nanomaterials are utilized in electronics, photonics, catalysts, renewable energy devices and biotechnology. Up to now, various synthesis methods for nanoparticles have been reported and used to produce such functional nanomaterials. The aerosol-based gas phase synthesizing methods are considered as clean and efficient methods for producing those functional nanomaterials, which could not fully satisfied with existing sol-gel methods. Many of aerosol-based gas phase methods have been studied and used such as electrical discharge, laser ablation, evaporation-condensation and synthesizing in flame and each method has been studied and utilized to produce nanomaterials. With these motivation, in this thesis, we describe the method for synthesizing oxide nanoparticles with different properties with high selectivity and introduce a novel spark generator for stable sub-10 nm nanoparticle generation.

The flame metal combustion method, which utilizes solid metal powder as precursors and oxy-hydrogen diffusion flame of extremely high

temperature, is one of the facile and effective aerosol-based gas phase synthesizing method of nanoparticles. This method can be used for producing various oxide nanoparticles such as ZnO, MgO, SnO<sub>2</sub>. Using this method, we discovered that terraced and spherical MgO nanoparticles which have unique optical property could be generated. We investigated the optimized flame condition for the selective production of terraced and spherical MgO nanoparticles over conventional cubic ones. The size distribution of the produced MgO nanoparticles was measured to understand the growth condition of the nanoparticles. Furthermore, one was able to control the proportion of the morphology of generated MgO nanoparticles using different carrier gases. From the size distribution and the percentage of generated MgO nanoparticles, we found the dominant mechanism of terraced and spherical nanoparticles to be the fast surface defect-induced growth, which should be different from the growth mechanism of cubic MgO nanoparticles. We investigated the change of cathodoluminescence spectra of MgO nanoparticles doped with transition metals such as manganese and chromium to probe the nanoparticle morphology.

In order to generate sub-10 nm particles, spark discharge generation method is considered as an appropriate manner. Moreover, this method is a very effective method for producing charged aerosols which can be used as building blocks for nanofabrication. The electrode configuration in a spark discharge generator (SDG) plays a critical role in the characteristics of the process. For instance, the rod-to-rod configuration is unable to prevent nanoparticles from agglomerating due to slow local carrier gas velocity. On the other hand, the recently developed pin-to-plate configuration can produce unagglomerated nanoparticles, however, the geometric mean diameter and the number concentration of nanoparticles change over time as the pin gets eroded. To address the issue, a novel wire-in-hole type spark discharge generator (WH-SDG) that is able to generate unagglomerated nanoparticles with a constant size distribution over a long time was introduced. The WH-

SDG, which consists of a metal wire and a grounded plate with a hole in which the metal wire is located in the center, effectively suppressed changes in the electrode morphology and the gap distance, which cause the minimal variation of the spark discharge voltage and frequency in time. Therefore, the WH-SDG was able to maintain a constant size distribution of the generated nanoparticles for 12 hours. Additionally, it was found that the WH-SDG could control the diameter of nanoparticles by regulating the gas flow rate into the generator and produce nanoparticles out of various metals such as copper and palladium.

**Keywords: Aerosol-based nanoparticle synthesis; Flame metal combustion; Terraced MgO nanoparticles; Spark discharge; Wire-in-hole type spark discharge generator**

**Student Number: 2008-22895**

# Contents

<b>Abstract</b> .....	<b>i</b>
<b>List of Figures</b> .....	<b>vi</b>
<b>Nomenclature</b> .....	<b>x</b>
<b>Chapter 1. Introduction</b> .....	<b>1</b>
1.1. Background of Research .....	<b>2</b>
1.2. Objectives for Research .....	<b>6</b>
<b>Chapter 2. Flame Metal Combustion Method for Magnesium Oxide Nanoparticle Synthesis of Unique Morphology</b> .....	<b>9</b>
2.1. Introduction .....	<b>10</b>
2.2. Background of Research .....	<b>11</b>
2.2.1. Synthesis of MgO Nanoparticles .....	<b>11</b>
2.2.2. Flame Metal Combustion Method for Producing Oxide Nanoparticles .....	<b>14</b>
2.3. Experimental Details .....	<b>17</b>
2.4. Result and Discussions .....	<b>22</b>
2.4.1. Synthesis of Unique Terraced and Spherical MgO nanoparticles .....	<b>22</b>
2.4.2. Particle Size Distribution of MgO nanoparticles .....	<b>24</b>
2.4.3. Growth Mechanism of Terraced/spherical and cubic MgO nanoparticles .....	<b>38</b>
2.4.4. Cathodoluminescence of undoped and transition metal doped MgO nanoparticles .....	<b>45</b>

2.4.5. Oxidative Conversion of Methane Reaction of Flame-made MgO catalyst nanoparticles .....	49
2.5. Conclusion .....	53
<b>Chapter 3. Long-time Consistent Generation of sub-10 nm Nanoparticles using Wire-in-hole Type Spark Discharge Generator ...</b>	<b>55</b>
3.1. Introduction .....	56
3.2. Background of Research .....	58
3.2.1. Spark Discharge Nanoparticle Generator for Stable Nanoparticle Production .....	59
3.3. Experimental Details .....	60
3.4. Results and Discussion .....	66
3.4.1. Long-time Stability of Pin-to-Plate and Rod-to-Rod Type Spark Discharge Generator .....	67
3.4.2. 12-hour Continuous Generation of Ag Nanoparticles using Wire-in-Hole Type Spark Discharge Generator .....	72
3.4.3. Control of Particle Size Distribution and Synthesis of Various Metal Nanoparticles .....	78
3.5. Conclusion .....	84
<b>Chapter 4. Concluding Remarks .....</b>	<b>85</b>
<b>References .....</b>	<b>89</b>
<b>국문초록 .....</b>	<b>99</b>

## List of Figures

- Figure 2.1** (a) Schematic of flame metal combustion method (b) conventional metal combustion method.
- Figure 2.2.** Image of flame for synthesizing MgO nanoparticles. (a) Conventional Metal Combustion Method (self-ignition in ambient air) (b) Long flame ( $\text{H}_2 + \text{Ar}$  7+1 lpm,  $\text{O}_2$  2 lpm,  $\text{O}_2$  gas 1.5 lpm as carrier gas) (c) Middle-sized flame ( $\text{H}_2 + \text{Ar}$  4 lpm,  $\text{O}_2$  2 lpm,  $\text{O}_2$  gas 1.5 lpm as carrier gas) (d) Short flame with dilution gas ( $\text{H}_2 + \text{Ar}$  2+6 lpm,  $\text{O}_2$  2 lpm,  $\text{O}_2$  gas 1.5 lpm as carrier gas).
- Figure 2.3.** (a) TEM image of cube MgO nanoparticles (b) TEM image of Terraced MgO nanoparticles (c) X-ray diffraction of MgO nanoparticles. (d) Cathodoluminescence spectra of cube and terraced MgO
- Figure 2.4.** TEM images of nanoparticles synthesized from long flame condition ( $\text{H}_2 + \text{Ar}$  7+1 lpm,  $\text{O}_2$  2 lpm, carrier gas  $\text{O}_2$  1.5 lpm). Particles are collected at 10, 50, 100, 150, 200, 250 mm from the burner.
- Figure 2.5.** (a) Temperature distribution with the height in flame  $\text{H}_2/\text{Ar} = 7/1$  lpm along with the ratio of the number of terraced nanoparticles over cubic ones. (b) Diameters of terraced and cubic nanoparticles vs the height. The dashed zones in both plates mark the fast growth region of spherical nanoparticles. Dotted lines are guides for eye.
- Figure 2.6.** TEM images of nanoparticles synthesized from short flame condition ( $\text{H}_2 + \text{Ar}$  2+6 lpm,  $\text{O}_2$  2 lpm, carrier gas  $\text{O}_2$  1.5 lpm). Particles are collected at 10, 50, 100, 150, 200, 250 mm from the burner.
- Figure 2.7.** (a) Temperature distribution with the height in “short” flame ( $\text{H}_2/\text{Ar} = 2/6$  lpm) along with the ratio of the number of terraced nanoparticles over cubic ones. (b) Diameters of terraced and cubic nanoparticles vs the height in flame. The dashed zones in both plates mark the fast growth region of

spherical nanoparticles.

- Figure 2.8.** TEM images of nanoparticles generated varying the flowrate of fuel and dilution gas. Particles are collected at 250 mm from the burner.
- Figure 2.9.** (a) The ratio of terraced over cubic nanoparticles vs hydrogen flow rate. (b) Sizes of nanoparticles at 250 mm vs the flow rate of hydrogen for terraced and cubic nanoparticles. The dotted lines are guides for eye.
- Figure 2.10.** (a) TEM images of nanoparticles collected at different heights for argon carrier gas. (b) Proportion of terraced nanoparticles vs the height in flame for oxygen and argon carrier gas. (c) The CL spectra for nanoparticles produced with oxygen or argon carrier gases show very different light emission bands.
- Figure 2.11.** (a) TEM images of terraced nanoparticles reveal the proportionality law between the sizes of terraced nanoparticles vs the height of terrace steps. (b) The illustration of the growth mechanism that leads either to perfect spherical nanoparticles (mode II growth) or to terraced nanoparticles (when mode I growth follows mode II growth).
- Figure 2.12.** All possible cases of CL bands from cubic and terraced nanoparticles, including the dopant bands. Doping with  $\text{Cr}^{3+}$  ion produces characteristic 730 nm band with R and N zero phonon lines distinguished above 700 nm even at room temperature. Doping with  $\text{Mn}^{2+}$  may produce 610 nm and 750 nm bands.
- Figure 2.13.** (a) TEM image of flame-made Li/MgO catalyst particles (b) Methane conversion (c)  $\text{C}_2$  selectivity (d) Total  $\text{C}_2$  hydrocarbon yield of of flame-made Li/MgO particles.
- Figure 2.14.** Comparison of catalytic methane conversion of flame-made Li/MgO catalyst particles, terrace/ball MgO particles with wet-impregnated lithium and commercial MgO with wet-impregnated lithium.

(a) Methane conversion (b) C<sub>2</sub> selectivity (c) Total C<sub>2</sub> hydrocarbon yield of flame-made/ Li/MgO particles.

- Figure 3.1.** Spark discharge system and experimental setup (a) experimental schematic of the particle generation and measurement system. (b) Schematic of the electric circuit in a spark discharge generator.
- Figure 3.2.** Four different types of spark discharge generator. (a) Rod-to-rod type electrode configuration. (b) Pin-to-plate type electrode configuration. (c) Wire-in-hole type electrode configuration. (d) Wire-to-plate electrode configuration.
- Figure 3.3.** TEM images of Ag nanoparticles generated via two different types of spark discharge generator. (a) Nanoparticles generated by rod-to-rod type SDG at the beginning of the experiment. (b) After 12 hours from the beginning. (c) Nanoparticles generated by pin-to-plate type SDG at the beginning of the experiment. (d) After 12 hours from the beginning.
- Figure 3.4.** Size distribution of Ag nanoparticles generated via two different types of spark discharge generator measured every 3 hours. (a) rod-to-rod type SDG (b) pin-to-plate type SDG.
- Figure 3.5.** (a) ~ (e) Morphological changes in the tip of the pin electrode in a pin-to-plate type SDG. Changes in (f) spark discharge voltage and (g) frequency versus time for both SDGs.
- Figure 3.6.** Ag nanoparticles produced via wire-in-hole type SDG. (a) A TEM image of nanoparticles at the beginning. (b) A TEM image of nanoparticles after 12 hours from the beginning. (c) Size distributions of produced nanoparticles measured every 3 hours.
- Figure 3.7.** (a) ~ (e) Morphological changes in the wire electrode in wire-in-hole type SDG. Changes in (f) spark discharge voltage and (g) frequency versus time for WH-SDG.
- Figure 3.8.** Characteristics of particles generated via WH-SDG,

PP-SDG and WP-SDG versus time. (a) Geometric mean diameter. (b) Total number concentration. (c) Geometric standard deviation.

**Figure 3.9.** Size distributions of generated nanoparticles with different gas flow rate. (a) Geometric mean diameter. (b) Total number concentration (c) Geometric standard deviation

**Figure 3.10** Geometric mean diameters and total number concentrations of various metal nanoparticles generated by WH-SDG over 12 hours. (a) Silver (b) Copper (c) Palladium

## List of Tables

**Table 2.1.** Flame conditions for selective generation of terraced and spherical MgO nanoparticles

## Nomenclature

$C_{ext}$	External capacitance
$d_g$	Geometric mean diameter
$E_{spark}$	Energy dissipated during spark discharge
$R$	Charging resistance
$V_{discharge}$	Discharge voltage between electrodes
$V_{electrode}$	Potential applied to electrode
$V_{input}$	Applied setting potential from HV power supply
$\sigma_g$	Geometric standard deviation

# **Chapter 1.**

## **Introduction**

## 1.1 Background of Research

Nanoparticles are expected for having distinguished novel optical, electronical, electrochemical and mechanical properties from bulk materials (Karch et al., 1987; Kruis et al., 1998; Nalwa, 1999; Siegel, 1993; Yang et al., 2010; Yang et al., 2003) Thus nanoparticles have received great attention in various field of modern technology such as electronics, biosensors, optical devices and catalysts (Feldheim and Foss, 2001; Huang et al., 2008; Scheer, 2010).

In order to make practical utilization of nanoparticles, a clean and time-efficient synthesis method is required. Up until now, liquid sol-gel method is widely studied and used for generating nanomaterials. But the requirement to handle the costly and hazardous metal-organic precursors, the multistage character of the processes, the complexity of the apparatus and high energy consumption which lower productivity are disadvantages of liquid-based method for nanomaterial synthesis (Ding et al., 2001; Zolotko et al., 2004). On the other hand, a number of aerosol-based gas phase synthesis methods such as electrical discharge (Schwyn et al., 1988), plasma methods (Rao et al., 1998), laser ablation (Cai et al., 1998) and synthesized in flame (Pratsinis, 1998; Zachariah et al., 1995) are also generally utilized for producing nanoparticles. The gas phase methods for particle synthesis have advantages in terms of obtaining high purity nanomaterials and well disintegrated nanopowders of narrow size

distribution (Zolotko et al., 2004). In addition, aerosol processes generates much less byproducts than liquid-based synthesis methods and collection of particles is much easier from gas than from liquid solution (Pratsinis, 2010).

Among these aerosol-based gas phase synthesis methods, synthesis within flame is widely studied for various functional oxide nanoparticles such as  $\text{TiO}_2$ ,  $\text{ZnO}$ ,  $\text{Al}_2\text{O}_3$ ,  $\text{SnO}_2$  etc (Buesser and Pratsinis, 2012; Grossmann et al., 2015; Lee and Choi, 2002; Mädler et al., 2002; Strobel and Pratsinis, 2007; Thimsen and Biswas, 2007; Tricoli and Pratsinis, 2010). This flame synthesis method has many advantages, continuous and easy to scale-up, small space to place. However, most of flame synthesis including flame spray pyrolysis, employs only liquid solutions as precursors, and they can be possible residual pollutant which would degrade the property of products. Thus, utilizing pure solid metals as precursors of oxide nanoparticles is needed to produce oxide nanoparticles of high purity.

The flame metal combustion method was suggested to use solid metal precursor and showed possibility to produce various types of nanoparticles (Yang et al., 2010). This method also have possibility for controlling the morphology of particles which have different optical properties. With this motivations, the morphology of generated particles can be controlled using the flame metal combustion method. The precise study about controlling the productivity of  $\text{MgO}$  nanoparticles which have different morphology and cathodoluminescence property was carried on to enhance the selectivity of production of the nanoparticles having desired morphology.

Many of aerosol-based gas phase methods for nanoparticle synthesis including flame metal combustion can synthesize nanoparticles of which sizes are the range of 20~100 nm (Zolotko et al., 2004). In order to generating sub-10 nm metal nanoparticles with aerosol method, spark discharge generation is a simple and reliable method (Schwyn et al., 1988). This method can produce metal nanoparticles using diverse materials, and directly applied for the performance enhancement of nanodevices (Messing et al., 2009; Sung et al., 2014). Moreover, it can be a facile method for generating charged aerosols, which can be used as building blocks for controlled fabrication by electrical forces (Kim et al., 2006; Krinke et al., 2001; Lee et al., 2011; You et al., 2010). The rod-to-rod type spark discharge generator (RR-SDG), consists of two rod-shaped metal electrodes confront each other was generally used configuration for this method (Messing et al., 2009; Meuller et al., 2012; Tabrizi et al., 2009). And the pin-to-plate type spark discharge generator (PP-SDG) was introduced which can prevent unintended agglomeration of nanoparticles occurred from the rod-to-rod spark discharge generator (Han et al., 2012). However, the particle size distribution changes over time due to the geometric conditions of pin and plate electrodes are not maintained during long-time operation.

To produce sub-10 nm nanoparticles consistently over time, a new type of spark discharge generator was suggested, called a wire-in-hole type spark discharge generator, which effectively suppressed changes in the

electrode morphology and the gap distance between electrodes for 12 hours. Enhanced stability of this generator will be advantageous for nanofabrication which uses nanoparticles as building blocks.

## 1.2. Objectives for Research

In this research, we pursue developing efficient aerosol-based gas phase synthesis methods for producing nanoparticles having unique properties with size-controllability, possibility to scale-up and maintaining consistency of generated particles. To accomplish this objectives, we extend the capability of flame metal combustion method which can produce nanoparticles with the controllability of particle size and morphology. Next, it is required to address the issue of the consistent generation of sub-10 nm particles without the change of size distribution over long time operation for the utilization of nanoparticles as building blocks for fabricating the nanopattern having desired shapes.

Producing nanoparticles with flame metal combustion method showed possibility for versatility and controllability of morphology and size within the range of 20~100 nm. In this research, the selective generation of oxide nanoparticles was achieved by changing the gas conditions of flame and the size distribution and the proportion of generated MgO nanoparticles and the optical and catalytic properties were investigated.

In order to generate sub-10 nm metal nanoparticles consistently without unintended agglomeration, it is required to integrate the merits of RR-SDGs and PP-SDGs. We designed a newly developed the wire-in-hole type spark discharge generator, and we proved this generator produced sub-10 nm particles consistently over 12 hours by measuring the particle size distributions.

## **Chapter 2.**

# **Flame Metal Combustion Method for Magnesium Oxide Nanoparticle Synthesis of Unique Morphology**

## 2.1. Introduction

MgO is one of the most intensively studied materials because of purely ionic nature and simple cubic rock-salt structure. MgO nanoparticles can be used for the construction of functional nanostructures (Cao et al., 2012; Dhal et al., 2015; Li et al., 2014) and for investigations of surface reactivity on oxides. (Pacchioni et al., 1994; Pacchioni and Maria Ferrari, 1999; Refson et al., 1995) Because equilibrium MgO [100] surfaces are considered chemically inert, the defects (both point defects and coordinately unsaturated ions in extended defects, such as ion vacancies and terrace steps) determine the properties of the MgO surfaces. Five-, four- and three-coordinated sites (i.e., 5C, 4C and 3C), which are characteristics of terraces, terrace steps and kinks, are known to be responsible for the electronic states of MgO nanoparticles (Shluger et al., 1999). One electron vacancies ( $F^+$  centers) and two electron vacancies ( $F^0$  centers) are also strongly related to the morphologies of MgO surfaces (Sterrer et al., 2006).

For synthesizing MgO particles, aerosol-based flame synthesis method is effective method for produce nanoparticles with high yield and controllability. The method is widely used for generating various oxide nanoparticles (Strobel and Pratsinis, 2007; Thimsen and Biswas, 2007; Yang et al., 2010). Moreover, this method can be easily scaled-up for mass production and controlling the size and properties by the flame condition.

## **2.2. Background of Research**

### **2.2.1. Synthesis Method for MgO Nanoparticles**

MgO nanoparticles can be synthesized by decomposing various magnesium salts or magnesium hydroxide ( $\text{Mg}(\text{OH})_2$ , brucite). However, MgO nanoparticles produced by this method have relatively large size with low surface area as well as broad size distributions. (Nagappa and Chandrappa, 2007). Thus, MgO nanoparticles are usually synthesized through sol-gel methods including hydrolysis and condensation (Portillo et al., 1996; Wang et al., 1997). But the sol-gel methods require expensive and hazardous metal-organic compounds as precursors, which is inconvenient and not economical (Ding et al., 2001). In contrast, flame synthesis methods, which use liquids or solutions as precursors have been widely used for producing functional nanoparticles (Buesser and Pratsinis, 2012; Grossmann et al., 2015; Lee and Choi, 2002; Mädler et al., 2002; Strobel and Pratsinis, 2007; Thimsen and Biswas, 2007; Tricoli and Pratsinis, 2010). A conventional metal combustion method using solid metal precursors is also one of combustion methods to synthesize nanoparticles (Patil et al., 2002). But this method is discontinuous and requires external energy sources. Also, the method tends to have unburned or remained precursors in the final products (Yang et al., 2010). Thus, it is required to establish the effective method for generating oxide nanoparticles with high productivity and controllability of particle size and morphology.

### **2.2.2. Flame Metal Combustion Method for Producing Oxide Nanoparticles**

To overcome the problems of this conventional metal combustion, a new flame metal combustion (FMC) method (Yang et al., 2010) was developed to produce pure metal-oxide nanoparticles. This flame metal combustion method has many advantages such as continuous process and high production rate, compact size, short production time, simple and safe ways to carry precursors into flames. Moreover, this method produces much less air pollution because it uses only oxy-hydrogen diffusion flame as the external energy source and metal or inorganic solid powders as precursors (Yang et al., 2010). Various metal oxide nanoparticles can be synthesized by this flame metal combustion method and the properties of nanoparticles could be altered easily by changing several parameters.

One of advantages of FMC method is controlling the morphology of nanoparticles by changing the flame condition. Previously, some have shown changing morphology of MgO nanoparticles using different methods, such as wet etching for several days (Hacquart and Jupille, 2009) and deposition by RF discharge (Muraoka et al., 2009). However, these methods have limitation to generate particles with various morphologies. In contrast, the FMC method produced unique terraced- and spherical-shaped MgO nanoparticles (for brevity we name both “terraced” MgO nanoparticle) in addition to general perfect cubic MgO nanoparticles by changing the flame condition.

Moreover, we revealed the two-band luminescence of terraced and

spherical MgO nanoparticles synthesized by the FMC method and this novel optical characteristic was attributed to the unique divacancy defect states of the MgO particles (Pikhitsa et al., 2015). The FMC method played there an important role of those extreme conditions at which the divacancies were generated in abundance. As we show below, the same extreme conditions in FMC method manifested themselves in non-cubic morphology of MgO nanoparticles. Having in mind possible prospects of using the two-band luminescence in optoelectronics (especially interesting is the 260 nm emission band) and in defect-based lasing which can be tuned by changing particle size and morphology, the growth of the MgO nanoparticles should be carefully investigated.

In this study, size distributions of MgO nanoparticles with different shapes were controlled by varying the flame condition of the FMC to understand the growth process of terraced and spherical MgO nanoparticles in the flame. Controlling morphology and size is very important because the unique optical property of metal oxide nanoparticles is caused not only by their high surface area but also by the high concentration of low-coordinated sites and structural defects on their surface (Mishakov et al., 2002). Through this study, the optimal condition to produce terraced particle was found, and other ways to change morphology have been tried. Additionally, doping MgO nanoparticles with transition metals was conducted to probe the nanoparticle morphology with transition metal ions by following the change in MgO luminescence spectra according to the shape of the MgO nanoparticles.

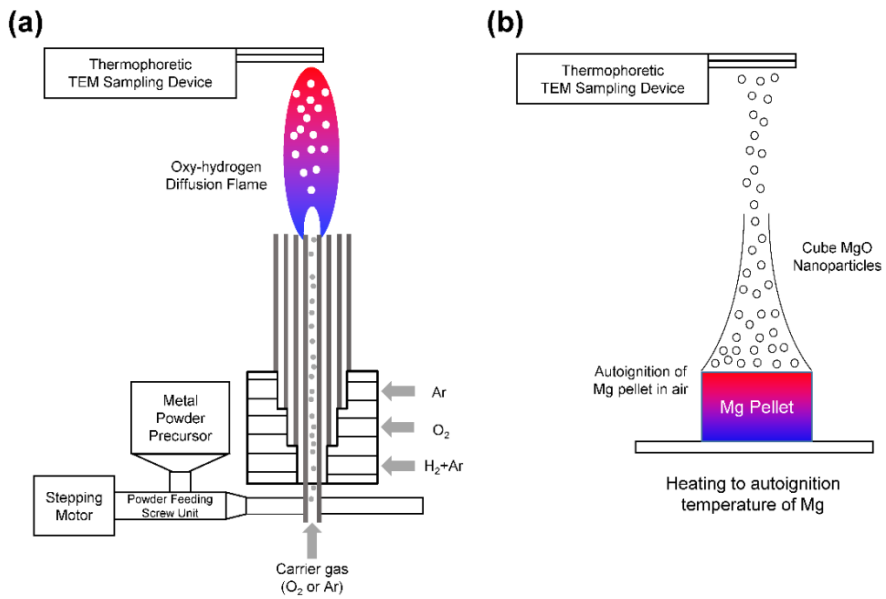
### 2.3. Experimental Details

Figure 2.1 shows schematic for the FMC (left panel) and one conventional combustion method (right panel) for producing MgO nanoparticles, respectively. For the FMC method, solid metal precursors were injected via screw feeding system to a co-axial burner. The co-axial burner for creating the oxy-hydrogen laminar diffusion flame consisted of four stainless-steel tubes. The screw feeding system of solid precursors and the production rate of nanoparticles are described in detail elsewhere (Yang et al., 2010). Micrometer-sized Mg metal powders (Alfa-aesar, 99.6% purity) were used as solid metal precursors to synthesize MgO nanoparticles through the FMC method. The injection mass rate of solid precursors was controlled by the revolution speed of the stepping motor connected to the screw feeding system. At the end of the mechanical feeding system, solid precursor powders were carried by oxygen (O<sub>2</sub>) or argon (Ar) (99.999% purity) into the oxy-hydrogen flame through the center nozzle of the coaxial burner. Hydrogen (H<sub>2</sub>) and O<sub>2</sub> (99.999% purity), as fuel and oxidizer, respectively, were fed through the following concentric annuli. Hydrogen was diluted with Ar to maintain the residence time in flame identically for all experiments. Ar shield gas was injected into the outermost concentric ring of the co-axial burner. The flow rate of oxidizer, carrier gas and shield gas were fixed as 2, 1.5 and 3 lpm for all experiments, respectively. The images of generated flame for producing particles are shown in Figure 2.2. As shown in Fig 2.2, the

flame size which determines the growth region of particles could be controlled by the flowrate of the gases injected to the flame reactor. The flame conditions of all experiments are summarized in Table 1. The flame temperature was measured using a B-type thermocouple with respect to the height of the flame. Generated MgO nanoparticles were sampled on the TEM grid using a localized thermophoretic sampling devices (Cho and Choi, 2000; Lee et al., 2008), and analyzed using normal (TEM, Carl Zeiss, Libra 120) and high-resolution transmission electron microscopes (HR-TEM, JEOL ARM 200F) to investigate the morphology and size distribution of MgO nanoparticles. Nanoparticles were also collected using a Si wafer to investigate the crystallinity. The structural characteristics of MgO nanoparticles were determined by X-ray diffraction (XRD, Mac Science, M18XHF-SRA). For investigating optical luminescence, cathodoluminescence measurement was carried out (CL, Gatan, MonoCL3) at room temperature.

In order to synthesize Li-doped MgO catalyst nanoparticles, Mg metal powders (99.8%, Alfa-aesar) were mixed with 5 wt% of lithium carbonate powders (Li, 99.98 %, Alfa-aesar). The mixture precursor was injected to the oxy-hydrogen diffusion burner via the screw powder feeder. The flame condition for reaction was the long flame condition ( $H_2$  7 +Ar 1 lpm,  $O_2$  2 lpm,  $O_2$  1.5 lpm as carrier gas, Ar 4 lpm as shield gas). The control sample was prepared by a wet-impregnation method with the Li and a commercial MgO (99.995%, Sigma-Aldrich). The produced Li/MgO powder was sintered at

800°C for 4 hours in ambient air. The catalytic activity was measured in a quartz reactor at atmospheric pressure with heating up the reaction gases to 700°C (Lee et al., 2015). The total flow rate of reaction gases was 50 sccm, and the ratio of the gases were  $\text{CH}_4:\text{O}_2:\text{Ar} = 4:1:5$ . The gas products after the catalytic reaction were analyzed by a gas chromatography (Agilent GC 6890N).



**Figure 2.1. (a) Schematic of flame metal combustion method (b) conventional metal combustion method**

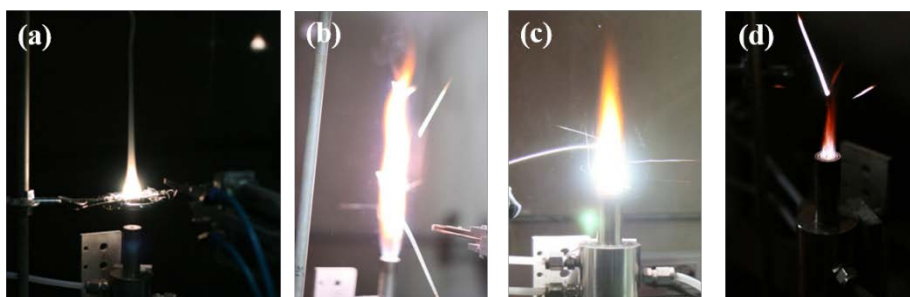


**Figure 2.2. Image of flame for synthesizing MgO nanoparticles. (a) Conventional Metal Combustion Method; self-ignition in ambient air. (b) Long flame;  $H_2 + Ar$  7+1 lpm,  $O_2$  2 lpm,  $O_2$  gas 1.5 lpm as carrier gas (c) Middle-sized flame;  $H_2 + Ar$  4 lpm,  $O_2$  2 lpm,  $O_2$  gas 1.5 lpm as carrier gas (d) Short flame with dilution gas;  $H_2 + Ar$  2+6 lpm,  $O_2$  2 lpm,  $O_2$  gas 1.5 lpm as carrier gas.**

Flame condition	Long flame	Short flame with dilution gas	Long flame with Ar carrier gas
H <sub>2</sub> / Dilution gas(Ar) (lpm)	7/1	2/6	7/1
O <sub>2</sub> (lpm)	2	2	2
Carrier gas (O <sub>2</sub> or Ar) (lpm)	1.5 (O <sub>2</sub> )	1.5 (O <sub>2</sub> )	1.5 (Ar)
Shield gas (Ar) (lpm)	3	3	3

**Table 2.1. Flame conditions for selective generation of terraced and spherical MgO nanoparticles (lpm: liter per minute)**

## **2.4. Results and Discussion**

### **2.4.1. Synthesis of Unique Terraced and Spherical MgO Nanoparticles**

Figures 2.3(a) and 2.3(b) shows the difference of morphology of the particles synthesized using two different methods. The MgO nanoparticles produced via the FMC method show unusual terraced and spherical shapes, otherwise, nanoparticles synthesized with the conventional combustion method were common cubic-shaped nanoparticles. From the X-ray diffraction analysis in Fig. 2.3(c), the crystal structures of both types of nanoparticles were identified as pure MgO. The notable difference between two differently shaped MgO nanoparticles is seen from the cathodoluminescence (CL) spectra given in Fig. 2.3(d), where terrace or spherical nanoparticles show the ultraviolet luminescence band at 260 nm, which did not appear in cubic MgO nanoparticles.

The origin of this luminescence was a divacancy center in MgO which was formed during mode II (depicted in Figure 2.11) combustion process, and this luminescence phenomenon was investigated in detail in Section 2.4.4.

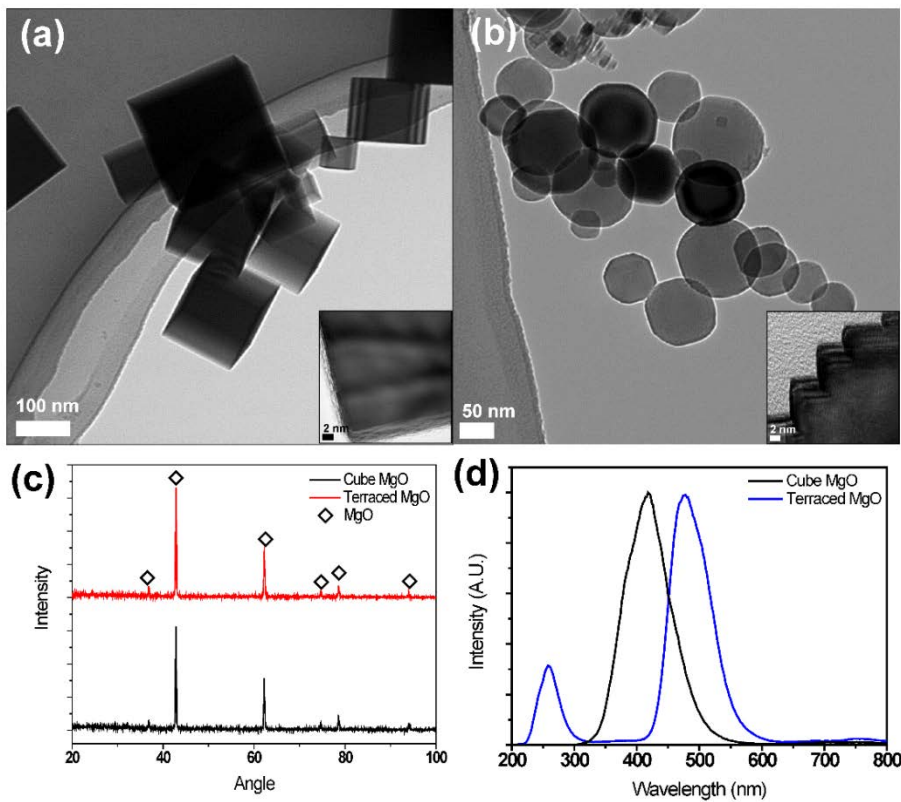


**Figure 2.3. (a) TEM image of cube MgO nanoparticles (b) TEM image of Terraced MgO nanoparticles (c) X-ray diffraction of MgO nanoparticles. (d) Cathodoluminescence spectra of cube and terraced MgO**

## 2.4.2. Particle Size Distribution of MgO Nanoparticles Generated in Two Different Conditions

Figure 2.4 shows the TEM images of the MgO nanoparticles generated at the long flame condition (see Table 1) with respect to the axial flame height above burner where the nanoparticles were captured. The gas composition of the long flame condition was H<sub>2</sub> 7 lpm diluted with Ar 1 lpm (H<sub>2</sub>/Ar: 7/1) and the flow rate of other gases are described in Table 1. The particle size distribution (PSD) and the portion of the terraced nanoparticles were measured with the TEM images. From Figure 2.5(a), 84% of particles were terraced nanoparticles at 10 mm from the bottom of the flame, and it showed the lowest portion of terraced nanoparticles (36%) at 250 mm. The nanoparticle size depicted in Figure 2.5(b) showed that the growth of terraced nanoparticles occurred at lower height of the flame, implicating a very fast initial growth. On the other hand, cubic nanoparticles mostly grew in the higher flame region, which could come from the relatively slower growth process of the cubic MgO nanoparticles than the terraced particles. When the particle grows with diffusion-limited surface growth mechanism, particle diameter  $d_g$  follows the equation (Beaucage et al., 2004):

$$d_g = [DV_m(C_b - C_d)t]^{1/2} + d^* \quad (1)$$

From the equation,  $d_g$  is proportional to the square root of residence time in flame. Using the velocity of gas in flame  $v_g = 1$  m/s, the term for time  $t$  can be changed to  $t = x/v_g$ , which  $x$  is the distance from the flame burner height.

Then the equation (1) can be rewritten as (Chae, Pikhitsa, et al., 2015):

$$d_g = (D^*)^{1/2} t^{1/2} = (D^*/\nu)^{1/2} x^{1/2} \quad (2)$$

From the curve of terrace/ball nanoparticles in figure 2.5, the value of apparent diffusion coefficient  $D^* = DV_m(C_b - C_d)$  was  $82.4 \text{ nm}^2/\text{ms}$ , and the value of diffusion coefficient  $D$  can be estimated to  $0.926 \text{ cm}^2/\text{sec}$  at  $1900 \text{ K}$  (Beaucage et al., 2004).

To understand the experimental data presented in Figs. 2.4-2.10 one has to be governed by the principal difference between the two existing modes of growth of cubic and spherical (terraced) nanoparticles, say, mode I and mode II, respectively. This difference lies in explosive-like (surface defect-induced fast) growth of spherical seeds (depicted in Figure 2.7) and then, of spherical (terraced) nanoparticles in the high-temperature zone (mode II); in Figure 2.5 (a) this zone is restricted within 0-50 mm heights (dashed in Figure 2.5(a), 2.5(b), see figure caption). We will discuss the mechanism of the fast growth in detail below, while discussing Figure 2.10; here we only mention that cubic nanoparticles are produced under the neat MgO molecule condensation (mode I) at lower temperatures and thus the growth is much slower than in mode II. The competition between those two modes is completely responsible for the dependences shown in Figs. 2.4-2.10.

As an example of how our concept of two mode growth works, let us consider the data in Figure 2.7. The fast mode II growth of spherical nanoparticles nearly stops after the high-temperature dashed zone (below 50

mm, Figure 2.5 (a), (b)) and only the slow growth of already formed terraced nanoparticles happens (see Figure 2.10) above 50 mm (Figure 2.5 (b)). On contrary, the higher and cooler part (above 50-100 mm height) of the flame promotes mode I and massive inception and further growth of cubic nanoparticles which is understandable from the proportion of Figure 2.5(a). The depression seen in Figure 2.5(b) for average size of cubic nanoparticles can be explained by a marginal low-temperature growth (mode I) possible even below 50 mm but only at the flame border in the horizontal direction of the high temperature zone where the flame temperature is lowered enough for mode I. Higher in flame, the cubic nanoparticles that grew before in this marginal zone below 50 mm will be diluted among numerous newly grown cubic nanoparticles of less size, so that the average size of the cubic nanoparticles drops down and is seen as a depression in Figure 2.5(b). Above the height of 50-100 mm the mode I growth leads to gradually increasing size of cubic nanoparticles.

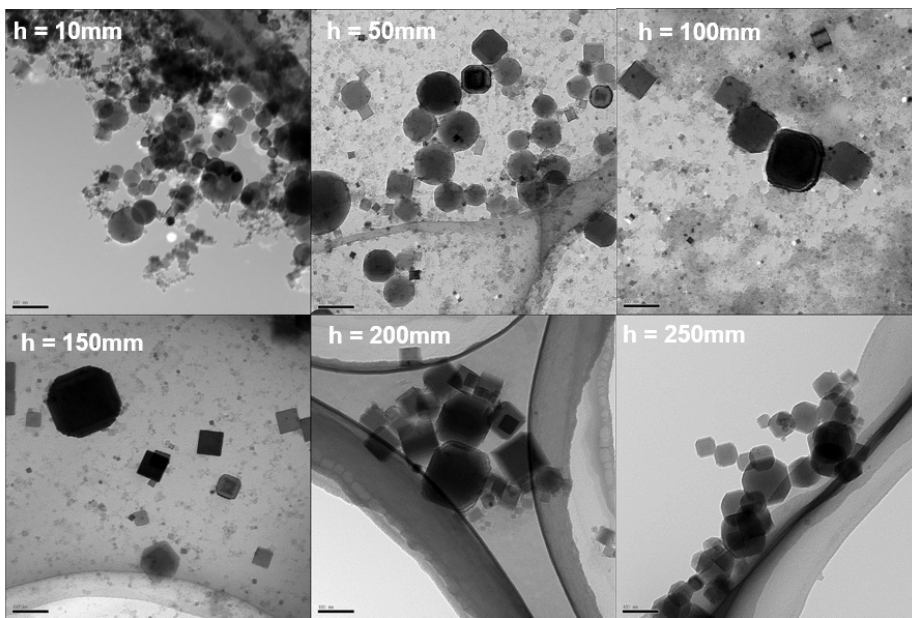


**Figure 2.4. TEM images of nanoparticles synthesized from long flame condition ( $\text{H}_2 + \text{Ar}$  7+1 lpm,  $\text{O}_2$  2 lpm, carrier gas  $\text{O}_2$  1.5 lpm). Particles are collected at 10, 50, 100, 150, 200, 250 mm from the burner.**

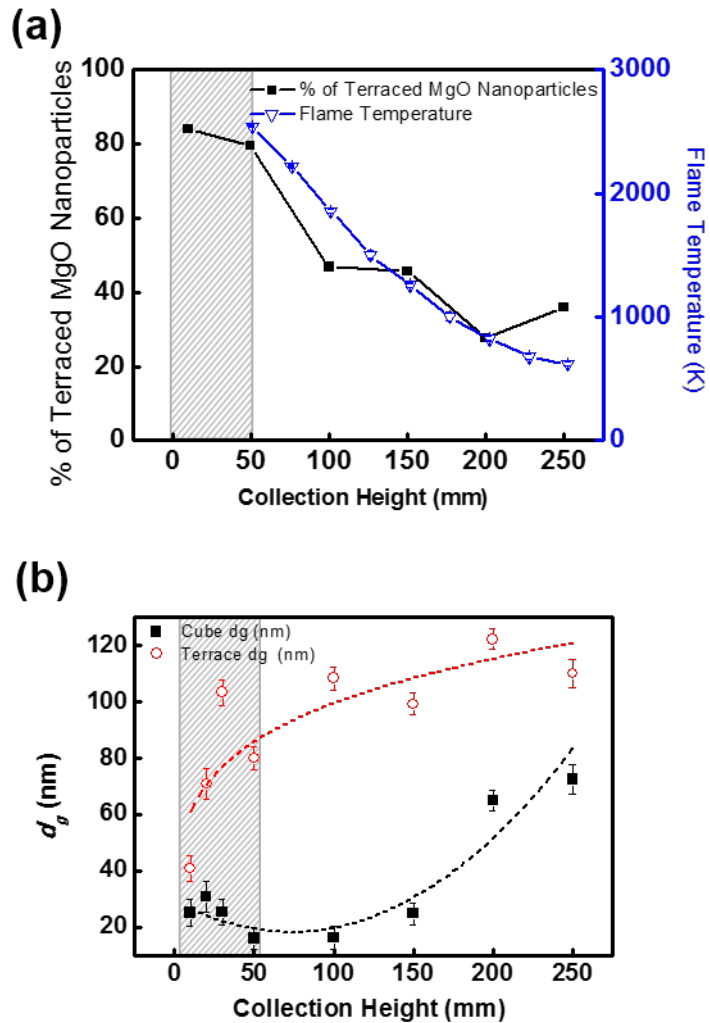
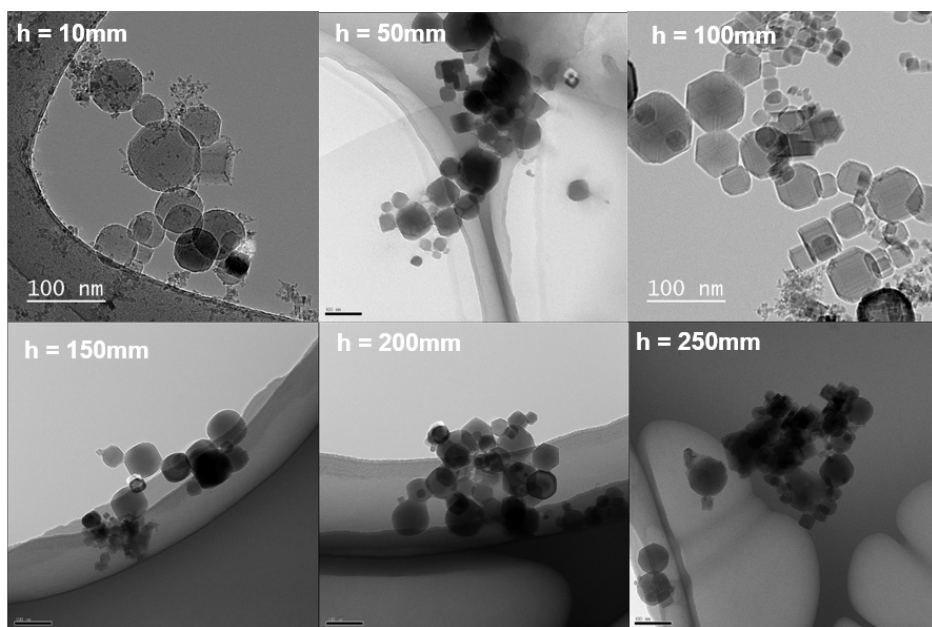


Figure 2.5. (a) Temperature distribution with the height in flame  $H_2/Ar = 7/1$  lpm along with the ratio of the number of terraced nanoparticles over cubic ones. (b) Diameters of terraced and cubic nanoparticles vs the height. The dashed zones in both plates mark the fast growth region of spherical nanoparticles. Dotted lines are guides for eye.

An additional experiment with the short flame, which results are given in Figure 2.6 and 2.7 was conducted to find optimal condition for producing higher portion of terraced MgO nanoparticles. The gas flow rate of H<sub>2</sub>/Ar was 2/6 lpm and other conditions had the same gas flow rate as for the long flame condition. In this condition, most of the generated particles were terrace/spherical-shaped. From Figure 2.7 (a), 94% of the generated particles were terrace and spherical-shaped from the sample collected at 10 mm from the bottom of the flame, while the sample collected at 250 mm showed 83% of terraced MgO nanoparticles. Nanoparticles generated from short flame condition contained much higher portion of non-cubic particles than long flame condition. The geometric mean diameter of nanoparticles grew fast like for long flame condition but the growth zone in flame which had sufficiently high temperature was short, thus the final nanoparticle diameter was smaller than that generated in long flame condition.

This result supported the viability of our two-mode concept. The abundance of terraced nanoparticles, seen in Figure 2.7(a) stemmed from the mode II growth in the dashed zone. However, the temperature was somewhat lower (1500 K vs 2500 K in Figure 2.5(a)), the growth rate on mode II, being a thermally activated process, was lower as well. Also the final size of terraced nanoparticles in Figure 2.7(b) is only 60 nm vs 120 nm in Figure 2.5(b). Additionally, larger O<sub>2</sub> concentration in 2/6 flame provides more effective surface defect growth on spherical nanoparticles via mode II (see also Figure 2.9(a) below). Note, by the constant irradiation of the burning

zone of an Mg pellet in oxygen with a CW CO<sub>2</sub> laser we found that exclusively spherical and terraced nanoparticles can be created.(Stankic et al., 2011) On the other hand, the growth of cubic nanoparticles on mode I proceeded similar to Figure 2.5(b). Yet, the number of those nanoparticles was much less because of much lower flame temperature above 50 mm height (Figure 2.7(b)), which reduces the number of incipient cubic nanoparticles. Therefrom the prevailing number of terraced nanoparticles over the cubic ones originates (Figure 2.7(a)).



**Figure 2.6. TEM images of nanoparticles synthesized from short flame condition ( $H_2 + Ar$  2+6 lpm,  $O_2$  2 lpm, carrier gas  $O_2$  1.5 lpm). Particles are collected at 10, 50, 100, 150, 200, 250 mm from the burner.**

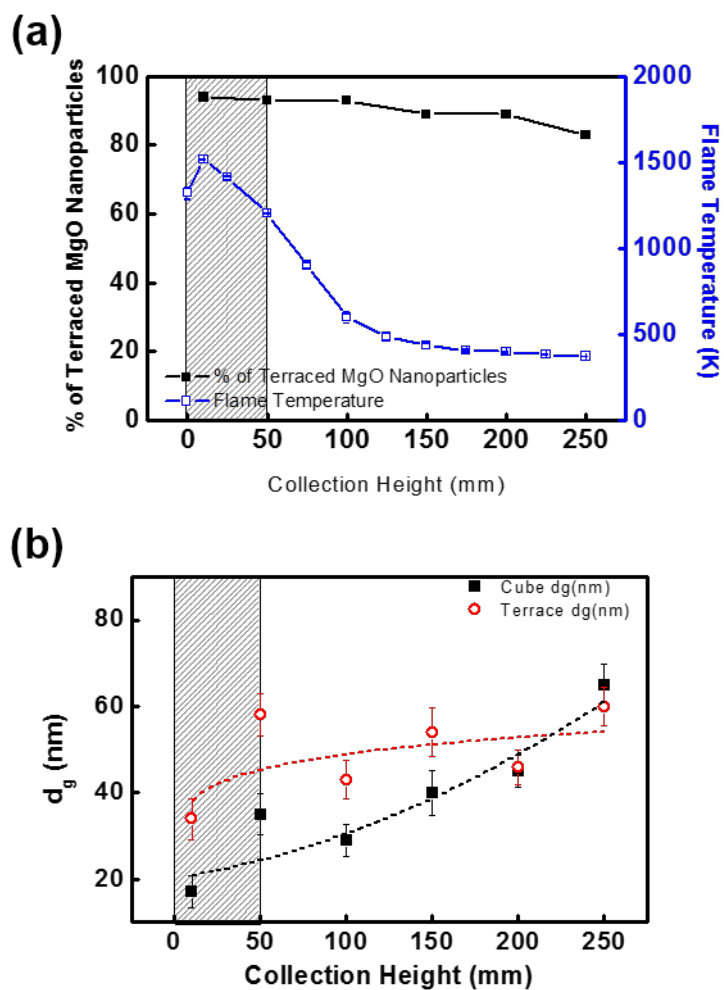


Figure 2.7. (a) Temperature distribution with the height in “short” flame ( $H_2/Ar = 2/6$  lpm ) along with the ratio of the number of terraced nanoparticles over cubic ones. (b) Diameters of terraced and cubic nanoparticles vs the height in flame. The dashed zones in both plates mark the fast growth region of spherical nanoparticles.

Changing the flow rate of fuel (hydrogen) and Ar dilution gas was carried out to inspect how the percentage of terrace-shaped MgO nanoparticles would be altered according to the gas composition and the flame size. From Figure 2.9, the percentage of terraced nanoparticles collected at 250 mm height increased as hydrogen in fuel gas ( $H_2+Ar$ ) decreased, and the average diameter of nanoparticles was smaller than the one at a higher proportion of hydrogen in fuel.

The flame conditions at  $H_2/Ar = 7/1$  and  $2/6$  in Table 2.1, considered above, are two extremes of the hydrogen flow rate changing from 7 to 2. The sizes and ratio of generated MgO nanoparticles are shown in Figure 2.9. The size of the terrace-shaped nanoparticles increased with the flow rate, while the size of the cubic nanoparticles was almost constant. It is in accord with the influence of the flame temperature on the growth rate on mode I. The ratio (Figure 2.9(a)) of terraced to cubic nanoparticles also followed the above described temperature-governed scenario.

Finally, we replaced carrier gas,  $O_2$  with Ar in flame  $7/1$  as described in Table 2.1 to see the effect of carrier gas. In other words, the  $O_2$  dependence of the terraced MgO nanoparticles during mode II at the long flame condition. Figure 2.10(a) shows cubic nanoparticles were mostly produced with the Ar carrier gas, although little amount of terraced nanoparticles was generated during mode II at 50 mm height (Figure 2.10(b)). However, as we discussed below, for larger nanoparticles at higher heights of the long flame condition and in the presence of hydroxyl groups the terraced nanoparticles can grow on

mode I as well, although in minor quantity (Figure 2.10(b)).

The large terraced nanoparticles (unlike the terraced nanoparticles grown on mode II seen at 50 mm) may not contain a specific defect center responsible for the two-band CL (260 nm and 490 nm) (Pikhitsa et al., 2015), which is evident in Figure 2.10(c) for the nanoparticles produced with O<sub>2</sub> carrier gas. The one-band CL (420 nm) and two-band CL are the strong indicators of two different growth modes.

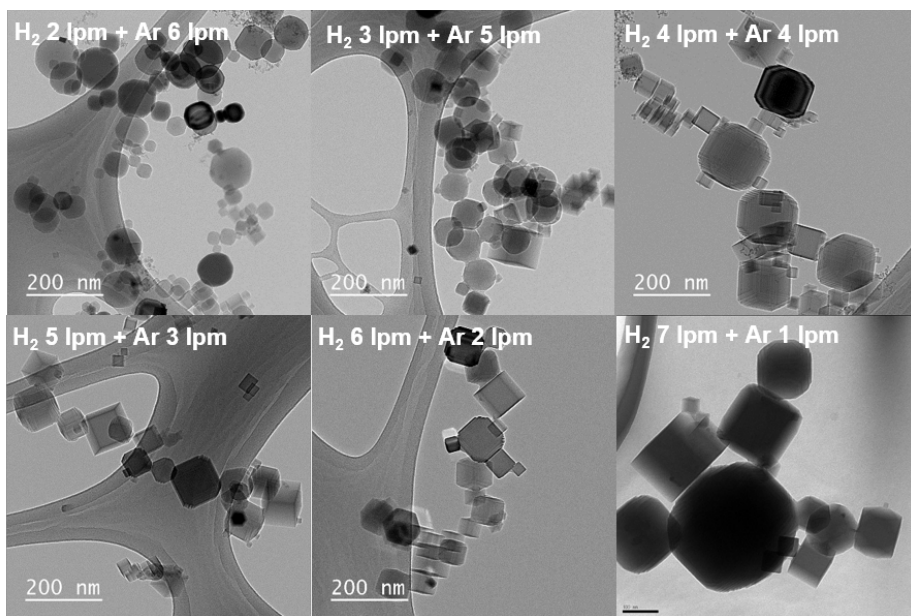


**Figure 2.8. TEM images of nanoparticles generated varying the flowrate of fuel and dilution gas. Particles are collected at 250 mm from the burner.**

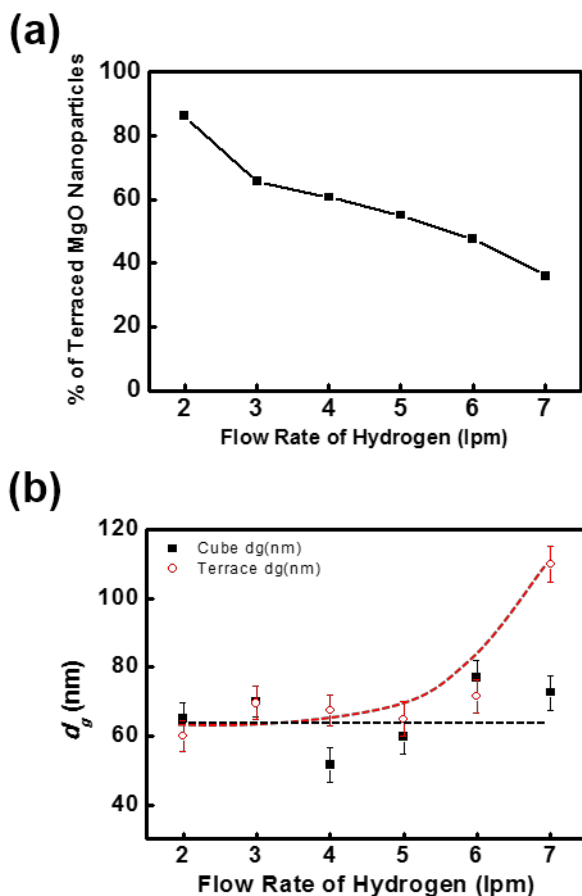


**Figure 2.9.** (a) The ratio of terraced over cubic nanoparticles vs hydrogen flow rate. (b) Sizes of nanoparticles at 250 mm vs the flow rate of hydrogen for terraced and cubic nanoparticles. The dotted lines are guides for eye.

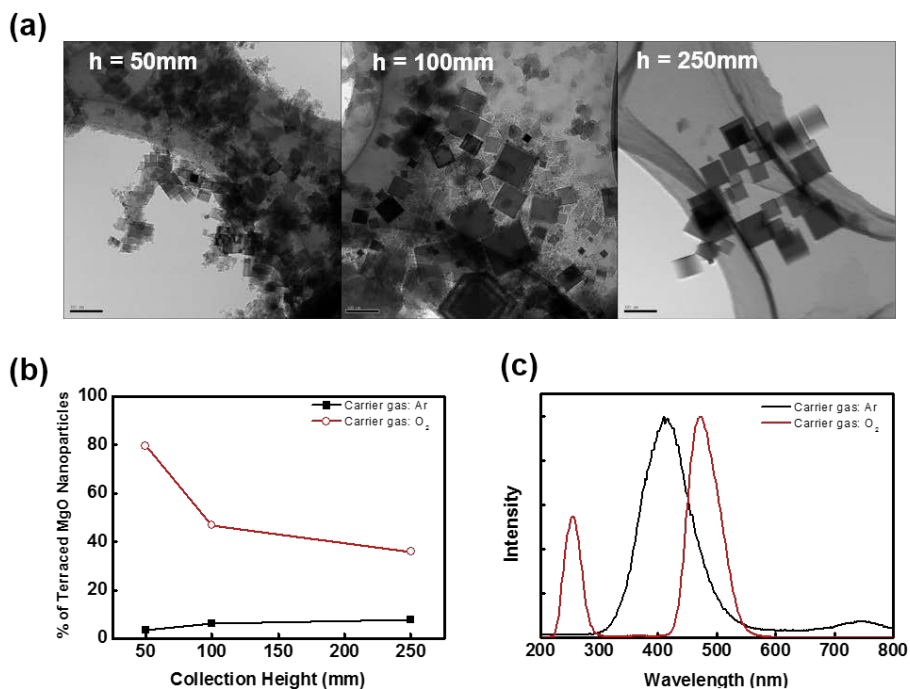


**Figure 2.10. (a) TEM images of nanoparticles collected at different heights for argon carrier gas. (b) Proportion of terraced nanoparticles vs the height in flame for oxygen and argon carrier gas. (c) The CL spectra for nanoparticles produced with oxygen or argon carrier gases show very different light emission bands.**

### 2.4.3. Growth Mechanism of Terraced/spherical and cubic MgO nanoparticles

From the HR-TEM images of Figure 2.11(a), one reveals a neat scaling law for terraced nanoparticles: the average size of the terrace steps on each nanoparticle is proportional to the size of the nanoparticle. This behavior excludes water vapor or hydrogen etching as being responsible for the large steps because etching always leads to tiny 1 nm steps.

To explain the linear dependence we notice that the large non-cubic nanoparticles are strictly divided into perfectly spherical and terraced ones. We claim that at the very initial stage of growth in flame both type nanoparticles are indistinguishably spherical and divide into two types only at the later stage of the growth. The possible mechanism of the generation and growth of the spherical MgO particles will be precisely described in this chapter.

Since long ago it has been known that there are two possible reactions that lead to solid MgO nanoparticles from Mg burning (Newman and Payne, 1987) : (I)  $\text{MgO}_{(g)} \rightarrow \text{MgO}_{(s)}$ , with enthalpy  $-566.3 \text{ kJ/ mol}$  at  $1900 \text{ K}$ ; (II)  $(\text{MgO})_n + \text{Mg}_{(g)} + 1/2 \text{ O}_2 \rightarrow (\text{MgO})_{n+1}$ , with larger enthalpy  $-729.3 \text{ kJ/ mol}$  at  $1900 \text{ K}$  . It is believed that only the first process, thus only the condensation from supersaturated MgO gas into MgO solid, takes place. (Altman et al., 2004; Newman and Payne, 1987; Stankic et al., 2011) Growth governed only by condensation of MgO molecules (mode I) leads to incipient cubes

and then to the larger cubes. However, computer simulations (Geneste et al., 2007) predict that O<sub>2</sub> molecules can be active and participate in nanoparticle surface growth (mode II) after O<sub>2</sub> molecules split over defects on the surface of growing MgO nanoparticles thus stimulating the most surface-defective (because the sphere is the most incompatible with the cubic lattice) incipient spherical shapes. The competition between the two growth mechanisms might take place with the intensification of the burning process that we performed with the oxyhydrogen flame or infrared laser.

It is known from literature that large terraced particles >200 nm can also grow in humid air by hydroxyl group passivation and thus stabilization of defective surfaces at later growth stage of primary cubes (Hacquart and Jupille, 2009; Moodie and Warble, 1971). On contrary, we observe much smaller than 200 nm terraced nanoparticles and spheres down to 10 nm (Figure 2.11). Such nanoparticles are also found for infrared laser intensified self-burning in air or oxygen where OH groups are not involved at all. This fact points out to mode II as the only reason for spherical and thus highly defective surface of nanoparticles in the environment of intensified self-burning. Then one may conclude that when spherical nanoparticles, initially grown on mode II, are transported by convection to the environment, favorable for MgO molecule condensation on mode I, and then continue their growth there, the incipient and then primary spheres start “healing” the surface defects and evolving into cubic nanoparticles through *terrace* step phase.

It is easy to see that there is no other intermediate *evolutionary* shape between the initial sphere and the final cube except the *terraced* nanoparticle that preserves the cubic MgO lattice for the single-crystalline nanoparticle. However, in the case when growth mode II persists through the whole nanoparticle growth then large perfect spheres can be grown from incipient and primary ones as we observe (Figure 2.11).

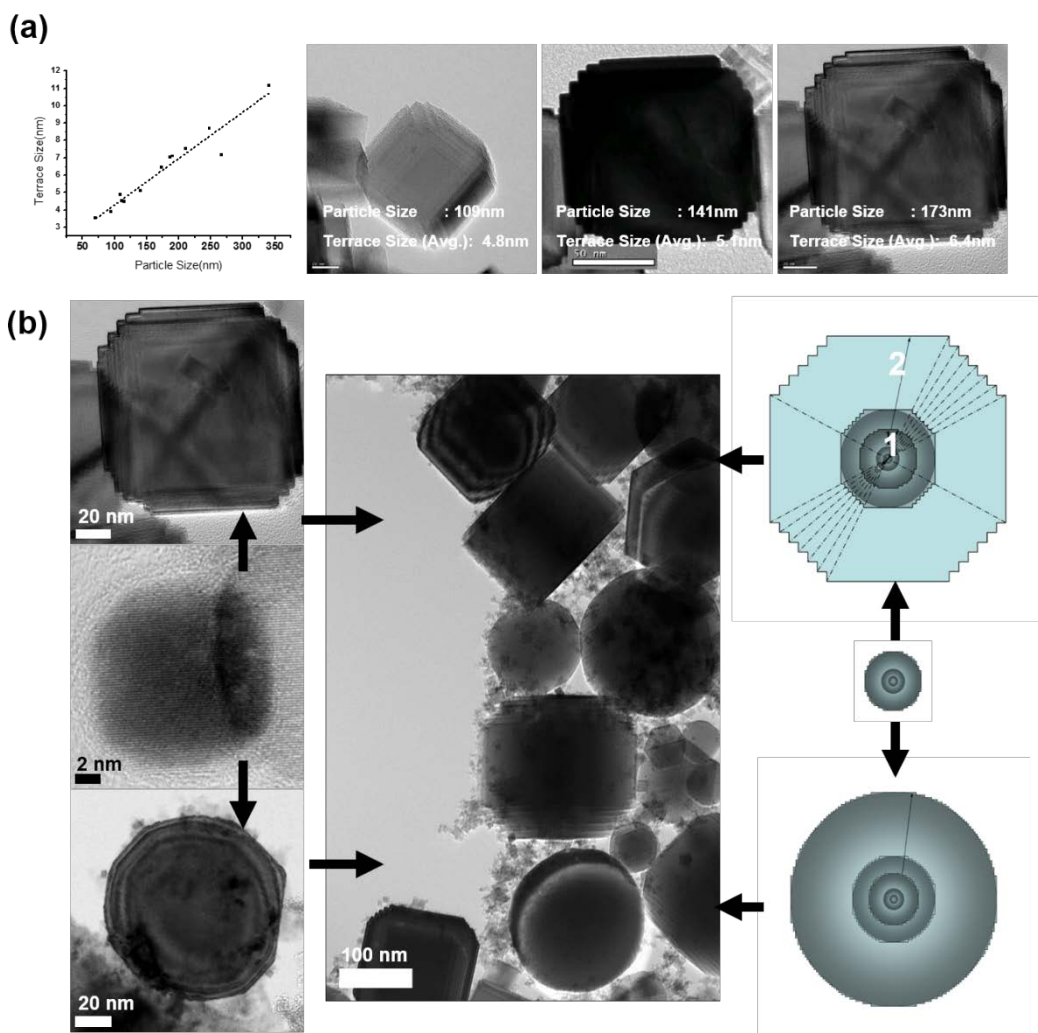


**Figure 2.11. (a) TEM images of terraced nanoparticles reveal the proportionality law between the sizes of terraced nanoparticles vs the height of terrace steps. (b) The illustration of the growth mechanism that leads either to perfect spherical nanoparticles (mode II growth) or to terraced nanoparticles (when mode I growth follows mode II growth).**

It is known from literature that large terraced particles >200 nm can also grow in humid air by hydroxyl group passivation and thus stabilization of defective surfaces at later growth stage of primary cubes (Hacquart and Jupille, 2009; Moodie and Warble, 1971). On contrary, we observe much smaller than 200 nm terraced nanoparticles and spheres down to 10 nm (Figure 2.11). Such nanoparticles are also found for infrared laser intensified self-burning in air or oxygen where OH groups are not involved at all. This fact points out to mode II as the only reason for spherical and thus highly defective surface of nanoparticles in the environment of intensified self-burning. Then one may conclude that when spherical nanoparticles, initially grown on mode II, are transported by convection to the environment, favorable for MgO molecule condensation on mode I, and then continue their growth there, the incipient and then primary spheres start “healing” the surface defects and evolving into cubic nanoparticles through *terrace* step phase. It is easy to see that there is no other intermediate *evolutionary* shape between the initial sphere and the final cube except the *terraced* nanoparticle that preserves the cubic MgO lattice for the single-crystalline nanoparticle. However, in the case when growth mode II persists through the whole nanoparticle growth then large perfect spheres can be grown from incipient and primary ones as we observe (Figure 2.11).

We now consider the evolution of the terrace step size. After a violent defect-induced surface growth in pure oxygen that leads to spherical precursor particles, the nanoparticle enters the flame region where

absorption-desorption processes (Mullins, 1957) dominate. Because a spherical precursor nanoparticle less than 5 nm is a nanoparticle with a perfect cubic MgO lattice according to HR-TEM, it may have as few as, say, 10 elementary steps of the MgO lattice constant of 0.21 nm on each “side”. These elementary steps (or grooves) act as incipient terrace steps and may start developing into the terrace steps seen in Figure 2.11. The number of steps may be conserved or reduced while the diffusion growth occurs.

Figure 2.11(b) gives the detail illustration of the mechanism for generation of terraced MgO nanoparticles either by the Mg self-burning within the oxy-hydrogen flame (HR-TEM images are given for this case) or with the infrared laser assisted Mg self-burning in air. The middle part of left (HR-TEM) and right (sketch) panels show a germ spherical nanoparticle created by fast surface defect-induced growth mechanism (mode II). The steps are of the size of the lattice distance. Top left and right panels (indicated with arrows) show the spherical nanoparticle evolution into a terraced nanoparticle in flame when adsorption-desorption of MgO molecules dominates. Then, as more and more MgO molecules are adsorbed without creating additional steps, the step size increases proportionally to the particle size and the number of steps nearly conserves as indicated by dashed lines in the top right panel. Of course, the process of reduction of the number of steps also takes place, as far as the nanoparticle evolves into a cubic shape, but nevertheless the step size still grows on average with the nanoparticle size. The evolution of the nanoparticle starts from the germ

nanoparticle marked 1 and continues to the large one marked 2. Bottom left and right panels show the spherical nanoparticle evolution into a much larger perfectly *spherical* nanoparticle when the germ nanoparticle continues its faster growth in O<sub>2</sub> environment where the surface defect induced growth (mode II) dominates. The middle panel is the TEM image of the resulting MgO smoke where both large spheres and terraced nanoparticles (up to large cubes) are distinguished.

#### 2.4.4. Cathodoluminescence of undoped and transition metal doped MgO nanoparticles

Without doping, the CL spectra, given in Figure 2.12 contain the 420 nm band (marked F at the left-hand column), the low coordination defect band (marked LC in both columns) and the P two bands (with the 260 nm and 490 nm components both marked P at the left-hand column) which are obviously seen both cathodoluminescence and low-temperature photoluminescence spectra (Pikhitsa et al., 2015).

Doping the terraced nanoparticles with  $\text{Cr}^{3+}$  ions generates an additional and well defined broad band at 730 nm seen in Figure 2.12. This band is complex and contains R and N zero-phonon lines that can be distinguished in CL spectrum given in Figure 2.12, together with the broad phonon replicas. Similar spectra were obtained for doped MgO thin films (Stavale et al., 2012). No specific features for  $\text{Cr}^{3+}$  doping peculiar to terraced nanoparticles are found. As we explain below, such peculiar features could come from the reduced crystal field felt by ions near LC defects. However, being a  $3d^3$  ion, a trivalent chromium should experience a  ${}^4\text{E}({}^2\text{G}) - {}^4\text{A}_2({}^4\text{F})$  optical transition that practically does not depend on the crystal field strength.

On contrary, doping terraced nanoparticles with  $\text{Mn}^{2+}$  may produce several  $\text{Mn}^{2+}$  bands, two of which are seen in Figure 2.12 (the one, often of somewhat lower intensity, at 610 nm and the one at 750 nm, both marked

Mn<sup>2+</sup>). The 750 nm band always appears in Mn<sup>2+</sup> doped MgO nanoparticles and comes from Mn<sup>2+</sup> ion in perfect environment of the octahedral sites in cubic crystal field of MgO lattice. The band is bulk in nature (though it is excited easily only in nanoparticles because the bulk optical transitions are weak) and has CL unresolved complex structure with a low-temperature zero phonon line at 735 nm (and the phonon replica band peaking at 750 nm at room temperature) that was discovered from photoluminescence in nanocubes of MgO (Altman et al., 2003). The band at 610 nm was not seen in previous work (Altman et al., 2003) because only the MgO nanocubes studied, being large and nearly perfect, had too few LC defects. On the other hand, terraced nanoparticles or tiny cubes have high concentration of LC defects as is seen from the presence of the LC bands in Figure 2.12. This presence is the necessary condition for the 610 nm Mn<sup>2+</sup> band. One can see that only if there is an LC band than the 610 nm may be seen. In other words, *when the 610 nm band exists, then LC band is always present*. Sometimes (as in the lowest panel in the right column) the 610 nm band is even more intense than the 750 nm band. At the left-hand column the 610 is always less than 750 nm, which can be explained by the abundance of perfectly spherical nanoparticles that lack terraces as *isolated* LC defects that have a distinguished electronic state. Spherical nanoparticles have virtually all the surface sites being defective; therefore the LC band is smeared and cannot be observed. For nanoparticles that show two-band UV-Vis CL (marked as P-bands in Figure 2.12) this is usually the case.

The state, responsible for the 610 nm  $\text{Mn}^{2+}$  band, comes from the lowering of the crystal field that splits the electron states of  $\text{Mn}^{2+}$  ion near LC defects. Basically, both bands come from the same  ${}^4\text{T}_1({}^4\text{G}) - {}^6\text{A}_1({}^6\text{S})$  optical transition,(Altman et al., 2003) however the reduced crystal field at LC defect sites shifts the emission of  $\text{Mn}^{2+}$  ion near an LC defect to shorter wavelengths. Thus, terraced MgO nanoparticles may be interesting for tuning the optical properties of doped MgO material by changing the crystal field intensity with terraces.

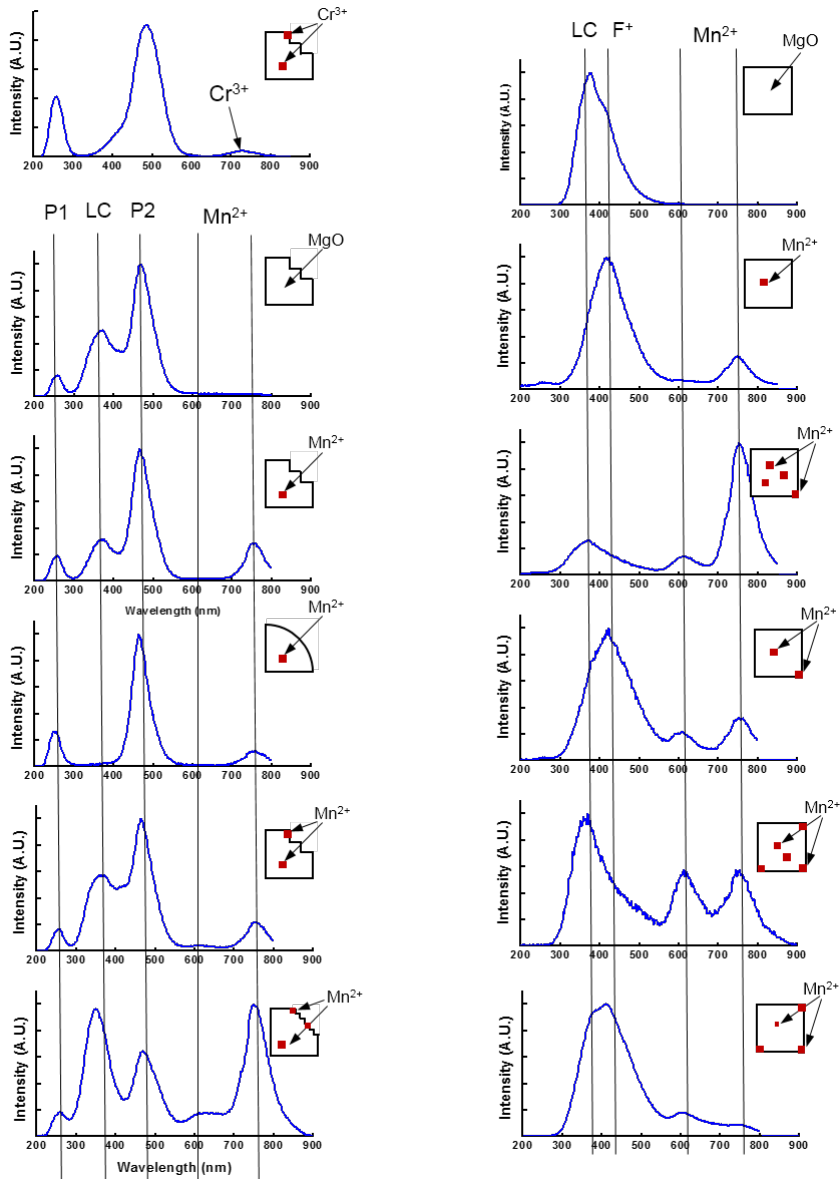


**Figure 2.12.** All possible cases of CL bands from cubic and terraced nanoparticles, including the dopant bands. Doping with  $\text{Cr}^{3+}$  ion produces characteristic 730 nm band with R and N zero phonon lines distinguished above 700 nm even at room temperature. Doping with  $\text{Mn}^{2+}$  may produce 610 nm and 750 nm bands.



#### **2.4.5. Oxidative Conversion of Methane Reaction of Flame-made MgO catalyst nanoparticles**

Methane, one of the main components of the natural gas has been highlighted as a carbon source for the chemical industry (Arndt et al., 2011; Lunsford, 1995). The MgO nanoparticles are considered as one of the most sufficient and stable supporters for the oxidative catalytic conversion of methane (OCM) reaction. With lithium as catalyst, Lithium-doped MgO (Li/MgO) composites have been considered as effective catalysts with a high conversion rate of methane and a good selectivity to the targeted higher hydrocarbons. Therefore, it is one of the most promising catalysts for the OCM reactions (Aritani et al., 2000; Arndt et al., 2011; Raouf et al., 2013).

So far, the wet-impregnation method has been widely studied and used for producing the Li/MgO catalyst particles. However, the wet-impregnation method requires long time to produce the catalyst particles because the method involves several time-consuming steps, such as stirring, mixing and drying solvents overnight (Aritani et al., 2000; Raouf et al., 2013).

Using the FMC method, the reaction for producing Li/MgO particles was completed only in a few seconds during the residence time of the particles in the  $H_2/O_2$  flame. Hence, the gas-phase FMC method reduced drastically the production time for the Li/MgO catalyst particles.

The conversion rate of methane gas of flame-made Li/MgO was 12.7 %

and total C<sub>2</sub> hydrocarbon(including C<sub>2</sub>H<sub>2</sub>, C<sub>2</sub>H<sub>4</sub>, C<sub>2</sub>H<sub>6</sub>) yield of 7.58 % at CH<sub>4</sub>:O<sub>2</sub> = 9:1 condition (Figure 2.13). This was rather low conversion efficiency, however, the reaction rate was increased by changing gas condition to CH<sub>4</sub>:O<sub>2</sub> = 4:1 without raising the rate of conversion to CO<sub>2</sub> and CO gas. As shown in Figure 2.14, the conversion rate of the methane into the flame-made Li/MgO was 22.5 %, and the C<sub>2</sub> selectivity was 55.6%. Hence, the total C<sub>2</sub> hydrocarbon yield was 12.5 % (Fig. 9 (c)). This yield was much higher than that (4.28%) of the control sample impregnation.

Although the yields reported by others were similar or higher in some degree (Aritani et al., 2000; Arndt et al., 2011; Raouf et al., 2013), synthesizing catalysts via the gas-phase FMC method has advantages of the short time to obtain catalyst particles without pollutants such as residues and byproducts. In addition, the FMC method can be easily scaled up by controlling the injection of precursors and installing multiply arranged flame burners, thus increasing the production rate of the catalyst particles.

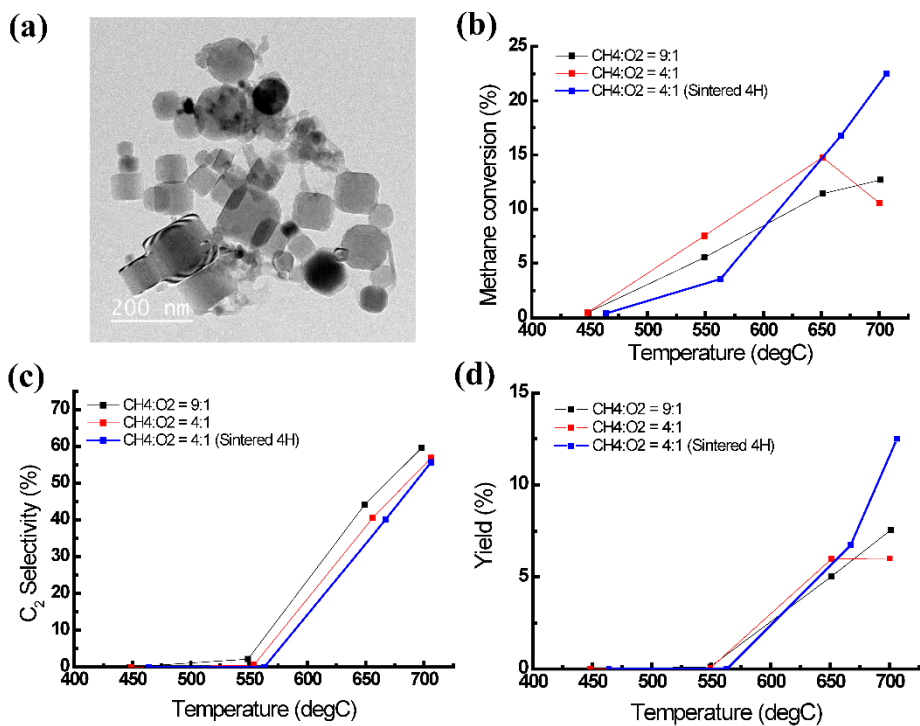


**Figure 2.13. (a) TEM image of flame-made Li/MgO catalyst particles (b) Methane conversion (c) C<sub>2</sub> selectivity (d) Total C<sub>2</sub> hydrocarbon yield of flame-made Li/MgO particles.**

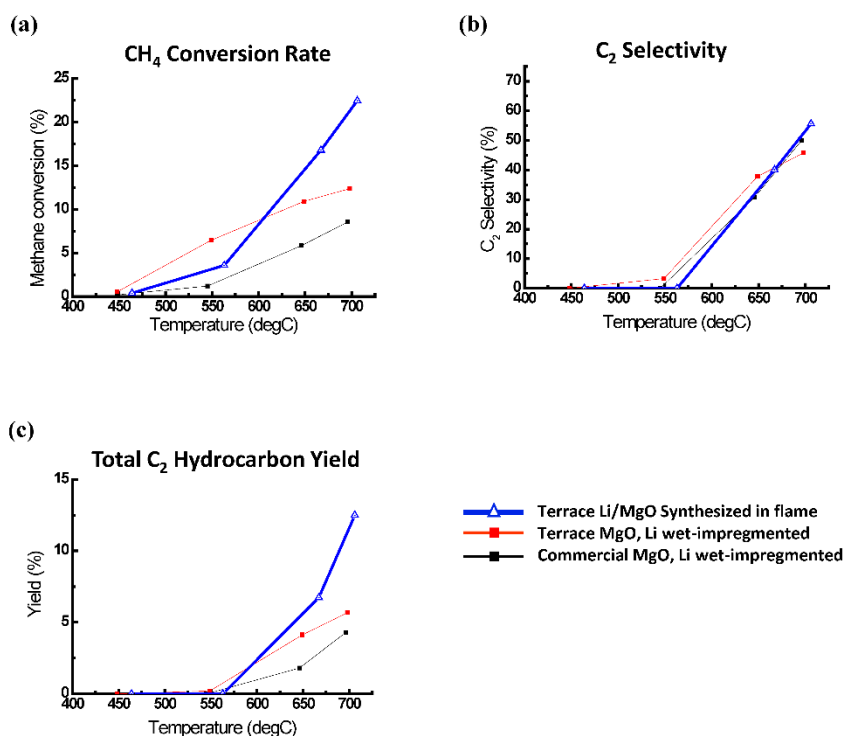


**Figure 2.14. Comparison of catalytic methane conversion of flame-made Li/MgO catalyst particles, terrace/ball MgO particles with wet-impregnated lithium and commercial MgO with wet-impregnated lithium. (a) Methane conversion (b) C<sub>2</sub> selectivity (c) Total C<sub>2</sub> hydrocarbon yield of flame-made/ Li/MgO particles.**

## 2.5. Conclusions

Terraced and spherical MgO nanoparticles, which have unique optical property of two-band luminescence, were synthesized using the FMC method. The FMC method is convenient for scaling up the production rate of the MgO nanoparticles over 10 g/hr. We investigated the proportion of the terraced and cubic MgO nanoparticles with respect to the size of the flame. Larger proportion and larger quantity of terraced nanoparticles were generated from the short flame condition, which was more abundant of oxygen. The size distribution of the produced MgO nanoparticles was also measured to understand the growth condition of the nanoparticles. From those results, optimal conditions for producing terraced and spherical MgO nanoparticles were found. Furthermore, one was able to control the proportion of the morphologically different MgO nanoparticles using different carrier gases. More terraced MgO nanoparticles were produced with oxygen carrier gas, otherwise the cubic MgO nanoparticles were predominantly generated with argon carrier gas.

From the size distribution and percentage (non-cubic over cubic) of generated MgO nanoparticles, we concluded that there are two different growth mechanisms of non-cubic (terraced and spherical) and cubic MgO nanoparticles. Generation of terraced/spherical MgO nanoparticles could be explained by fast surface defect-induced growth, which was quite different from the growth mechanism of common cubic MgO nanoparticles.

Finally, we investigated the luminescence and the catalytic property of MgO nanoparticles. The cathodoluminescence spectra of MgO nanoparticles could be changed by doping transition metals such as manganese and chromium to probe the concentration of low-coordination defects. Possible tuning of optical properties of MgO nanoparticles by controlling the morphology may be useful for optoelectronics of and lasing using MgO. In order to demonstrate the catalytic property of Li-doped terrace MgO nanoparticles synthesized via one-step flame metal combustion, oxidative coupling reaction of methane molecule was carried out and the catalytic terrace MgO nanoparticles showed higher conversion efficiency than commercial powder. Hence, the flame metal combustion method is highly productive and controllable method for synthesizing oxide nanoparticles that show unique morphology and properties with high selectivity.



## **Chapter 3.**

# **Long-time Consistent Generation of Sub-10 nm Nanoparticles using Wire-in-hole Type Spark Discharge Generator**

### 3.1. Introduction

Spark discharge generation (Schwyn et al., 1988) is a simple, clean and reliable method for generating nanometer-sized particles among diverse gas-phase synthesis techniques. Particles synthesized via a spark discharge generator can be directly used for the enhancement of many electronic and catalytic properties, for example, to increase the efficiency of an organic display device (Sung et al., 2014), to improve the performance of catalysts (Messing et al., 2009), and to generate gold seed particles for nanowire growth (Messing et al., 2009). Furthermore, spark discharge generation can produce nanoparticles using diverse materials having varied properties, such as bimetallic and mixed metallic nanoparticles (Byeon et al., 2008), and nanocomposites (Kala et al., 2013). In addition, this technique has been utilized to generate various types of charged aerosols, which enables the positioning of particles at precise locations on a dielectric surface (Krinke et al., 2001) and the fabrication of nanostructures via controlled electric field (Ha et al., 2014; Jung et al., 2014; Kim et al., 2006; Lee et al., 2011; You et al., 2010). Up to now, the rod-to-rod type spark discharge generator (RR-SDG) has been studied and used widely, however, this configuration inevitably generates unintended agglomerated nanoparticles which make difficult to be used for sophisticated nanofabrication.

In this work, we present a novel wire-in-hole type spark discharge generator (WH-SDG) that is able to generate unagglomerated nanoparticles with a constant size distribution over a long time (Chae, Lee, et al., 2015).

The WH-SDG, which consists of a metal wire and a grounded plate with a hole in which the metal wire is located in the center, effectively suppressed changes in the electrode morphology and the gap distance, which cause the minimal variation of the spark discharge voltage and spark frequency in time.

## **3.2. Background of Research**

### **3.2.1. Spark Discharge Nanoparticle Generator for Stable Nanoparticle Production**

Up until now, rod-to-rod type spark discharge generators (RR-SDG) have been widely studied, and the effects of the process parameters have been well understood (Horvath and Gangl, 2003; Roth et al., 2004; Tabrizi et al., 2009). However, particles generated by RR-SDG are prone to agglomeration at high number concentrations due to post-discharge diffusion charging in bipolar ion clouds (Bau et al., 2010). In an effort to prevent agglomeration of the particles, various methods have been developed such as controlling the flow rate of the carrier gas (Schwyn et al., 1988; Tabrizi et al., 2009) or injecting unipolar charged air ions (Park et al., 2014).

Recently, a pin-to-plate type spark discharge generator (PP-SDG), having asymmetric electrodes consisting of a sharp pin and a plate with a hole, was introduced which generates less agglomerated sub-10 nm nanoparticles with high concentration than the RR-SDG at the same condition (Han et al., 2012). This is attributed to the much faster transport of as-generated particles in the PP-SDG. Furthermore, the PP-SDG can be easily scaled up by employing multiple pin electrodes and corresponding exit holes in the flat-plate ground electrode (Ha et al., 2014). Despite such merits, the PP-SDG generated the particle size and the number concentration which evolve over time due to changes in the electrode geometry, such as gradual increases in the radius of curvature of the pin and in the distance between the pin and the plate as the

pin electrode gets eroded with time. These factors cause changes in spark discharge properties. In this study, to maintain the size distribution of produced nanoparticles over a long time while producing small and unagglomerated nanoparticles with high concentration, we designed a new type of spark discharge generator comprising a metal wire as a positive electrode and a grounded plate with a hole. The wire was placed in the center of an exit hole in the plate. Using this newly designed wire-in-hole type spark discharge generator (WH-SDG), we measured geometric mean diameter (GMD) and particle number concentration for twelve hours at various carrier gas flowrates. In addition, the versatility and controllability of the new design was demonstrated with different kinds of metal such as Cu and Pd.

### 3.3. Experimental Details

The experimental setup consists of a spark discharge generator, an electrostatic precipitator and a scanning mobility particle sizer (SMPS) system with an aerosol neutralizer, which is a commonly used particle measurement setup, as depicted in Figure 3.1(a) (Byeon et al., 2008; Han et al., 2012; Tabrizi et al., 2009). The spark discharge generator was made up of a cylindrical chamber, two electrodes, electrode holders and an inlet and an outlet for carrier gas flow. The inner diameter of the chamber is 40 mm and the length is 30 mm. The electrode holders were precisely machined and assembled at the center of the chamber. Alignment of the geometric condition of electrodes was controlled by putting the ground electrode on the 2-axis micro stage. Silver, copper and palladium (99.99% purity) were used as materials for electrodes. Nitrogen (99.999% purity) was used as the carrier gas, and the flow rate was set at 2 lpm. The size distribution of the generated particles was measured with a differential mobility analyzer (DMA, TSI 3085), a condensation nuclei counter (CNC, TSI 3776) and an Am-241 aerosol neutralizer (Grimm #5.521). The generated particles were transported to the DMA and the CNC, passing through an aerosol neutralizer. The flowrates of sheath and aerosol gas of DMA were set at 15 lpm and 1.5 lpm, respectively. The positively charged nanoparticles were collected on a carbon film-coated copper grid using electrostatic precipitator for 3 minutes, and imaged using high resolution-transmission electron microscope (HR-TEM, JEOL ARM

200F).

The circuit that provides electric power to the spark discharge generator is shown in Figure 3.1(b). Similar circuits have been widely used by other researchers to regulate the spark discharge characteristics (Han et al., 2012; Horvath and Gangl, 2003; Pfeiffer et al., 2014; Schwyn et al., 1988; Tabrizi et al., 2009). It consists of a high voltage power supply, an external capacitor ( $C_{\text{ext}}$ ) and a resistor ( $R_c$ ). Charging time of the external capacitor ( $C_{\text{ext}}$ ) can be chosen by selecting the resistance value of the external resistor ( $R_c$ ) which is depicted in figure 3.1(b). To generate nanoparticles which have desirable particle size distribution, the value of the external capacitor and the external resistor was determined. The high-voltage DC power supply (FuG HCP35-6500) with a maximum voltage of 6.5 kV was connected to one end of the resistor. High voltage power supply output ( $V_{\text{input}}$ ) was set at 6 kV to charge the external capacitor. The external capacitor which is much larger than the intrinsic capacitance between the two electrodes in SDG was connected in parallel to the electrode. Discharge voltage and spark frequency were measured with an oscilloscope (Agilent DSO-X 3014A) and a high voltage probe (Tektronix P6015A).

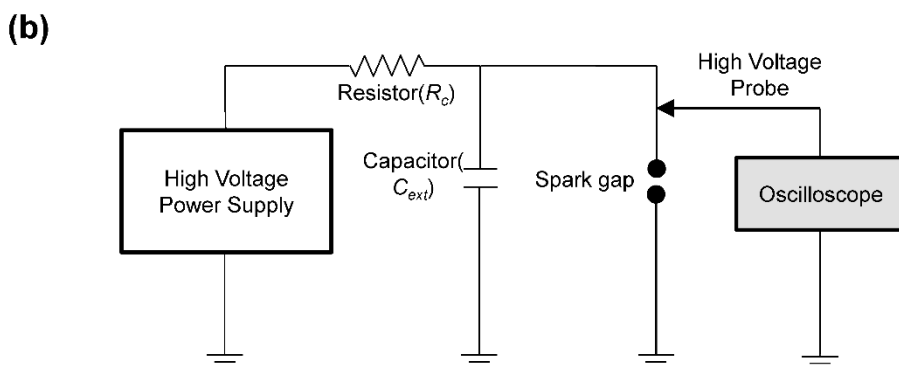
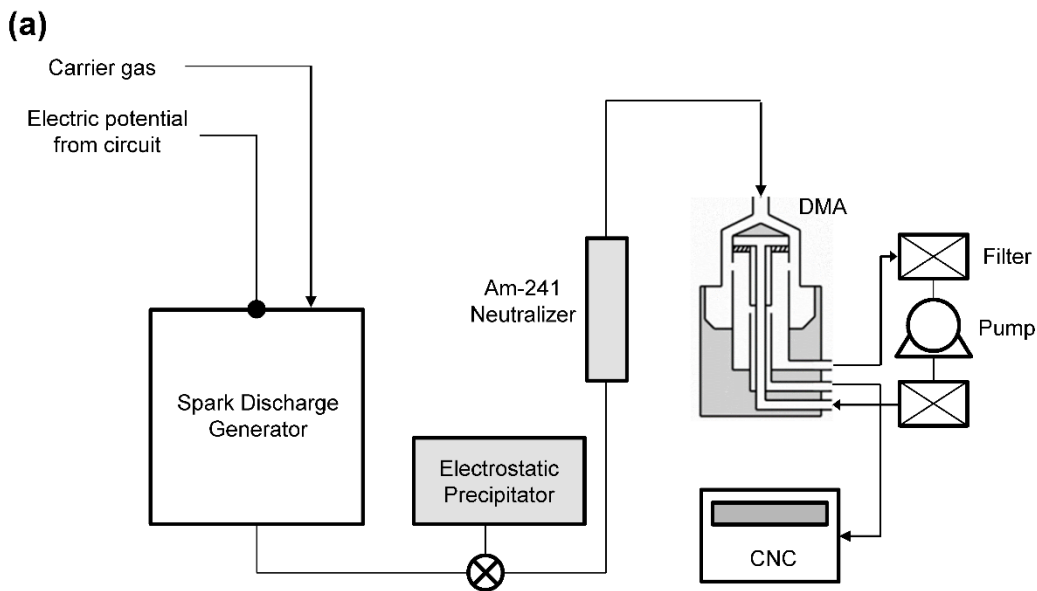


**Figure 3.1. Spark discharge system and experimental setup (a) experimental schematic of the particle generation and measurement system. (b) Schematic of the electric circuit in a spark discharge generator.**

We investigated the characteristics of four different electrode configurations as depicted in Figure 3.2: rod-to-rod, pin-to-plate, wire-in-hole and wire-to-plate configuration. For the rod-to-rod configuration, the diameter of cylindrical rod electrodes was 7 mm and the gap between the two electrodes was 0.75 mm. In the case of the pin-to-plate configuration, a pin electrode that had 7 mm diameter was machined to have a sharp tip with a radius of curvature of approximately 0.12 mm. The diameter of wire electrodes used in the wire-in-hole and wire-to-plate configuration was 0.5 mm and the wire electrodes were placed precisely in the center of the hole. The grounded electrode plate for the pin-to-plate, wire-in-hole and wire-to-plate configuration had the exit hole with a diameter of 2 mm in the center of the grounded plate electrode. The initial gap between the wire and the grounded plate was 0.75 mm for both the pin-to-plate type and the rod-to-rod type SDG.

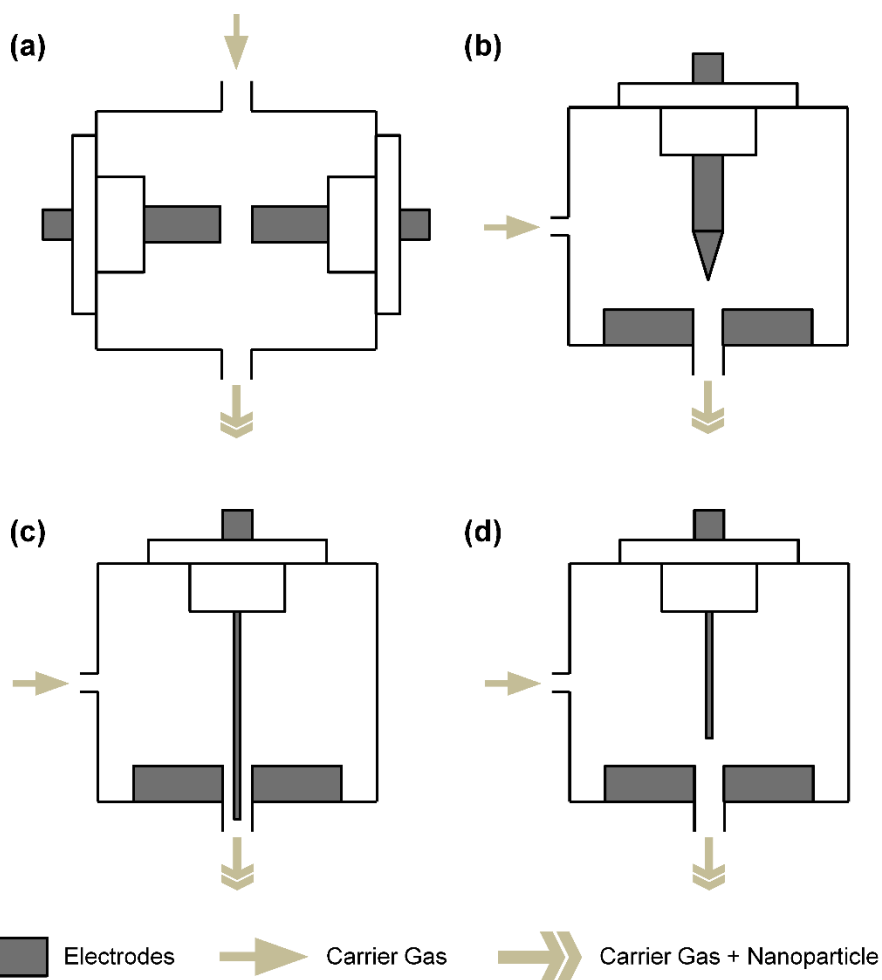


**Figure 3.2. Four different types of spark discharge generator. (a) Rod-to-rod type electrode configuration. (b) Pin-to-plate type electrode configuration. (c) Wire-in-hole type electrode configuration. (d) Wire-to-plate electrode configuration.**

## 3.4. Results and Discussion

### 3.4.1. Long-time Stability of Pin-to-plate and Rod-to-rod Type Spark Discharge Generator

The particle generation and size measurement were carried out continuously for 12 hours for the RR-SDG and the PP-SDG. Figure 3.3 shows the morphologies and size distribution of Ag nanoparticles generated by the rod-to-rod and pin-to-plate type generator. Each sub-figure shows a TEM image sampled before (Fig 3.3(a), 3.3(c)) and after tests which were conducted for 12 hours (Fig 3.3(b), 3.3(d)). SMPS measurements were also carried out every 3 hours to obtain the size distribution data (Figure 3.4).

The RR-SDG generated Ag particles with a wider size distribution than PP-SDG producing less agglomerated particles than RR-SDG. The geometric standard deviation ( $\sigma_g$ ) and the geometric mean diameter ( $d_g$ ) of the RR-SDG were 1.46 and 7.21 nm, respectively. On the contrary, the Ag nanoparticles generated by the pin-to-plate configuration showed a narrower size distribution with lower geometric standard deviation ( $\sigma_g = 1.36$ ) than that of the RR-SDG.

In the case of the PP-SDG, the size distribution of the particles became narrower over 12 hours. The diameter ( $d_g$ ) which was initially 7.32 nm declined gradually to 4.91 nm after 12 hours. The total number concentration of generated particles also decreased from  $1.12 \times 10^8 \text{ \#/cm}^3$  to  $5.70 \times 10^7 \text{ \#/cm}^3$ , as shown in Figure 3.4(b). For the rod-to-rod type generator, the size distribution did not change over time (with a minute difference of 0.21 nm in

diameter produced for 12 hours) as shown in Figure 3.4(a).

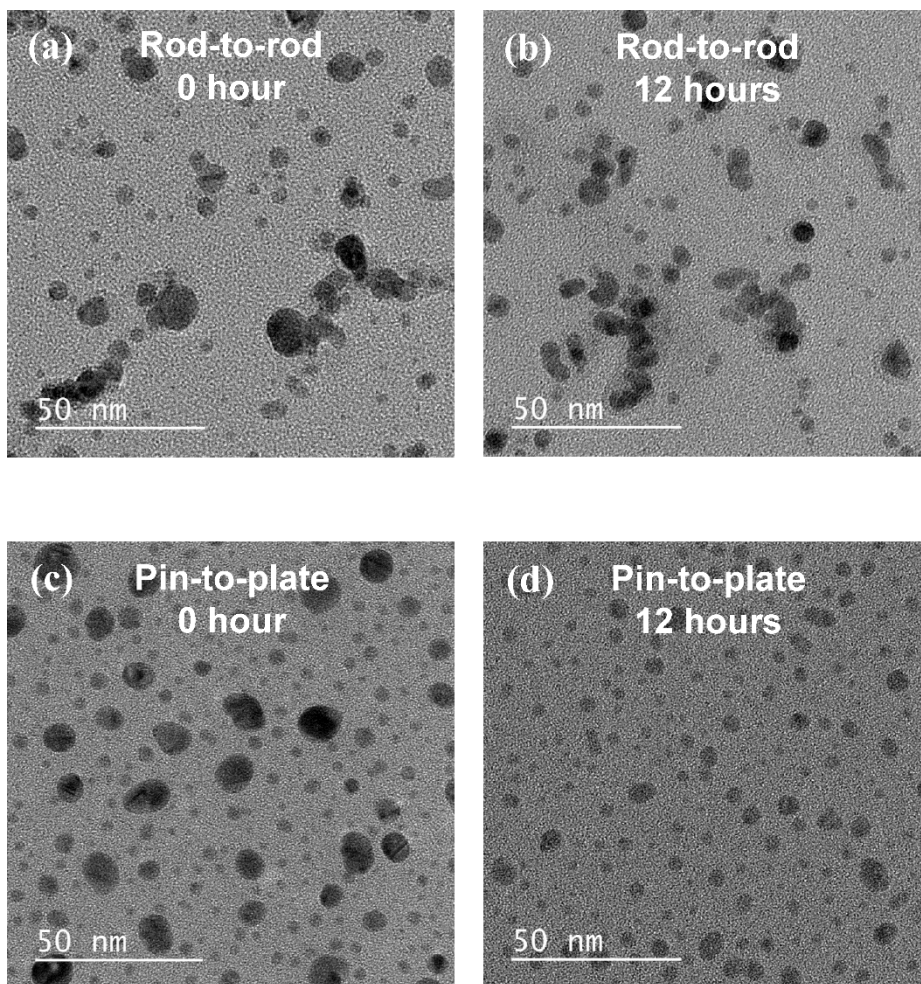


**Figure 3.3. TEM images of Ag nanoparticles generated via two different types of spark discharge generator. (a) Nanoparticles generated by rod-to-rod type SDG at the beginning of the experiment. (b) After 12 hours from the beginning. (c) Nanoparticles generated by pin-to-plate type SDG at the beginning of the experiment. (d) After 12 hours from the beginning.**

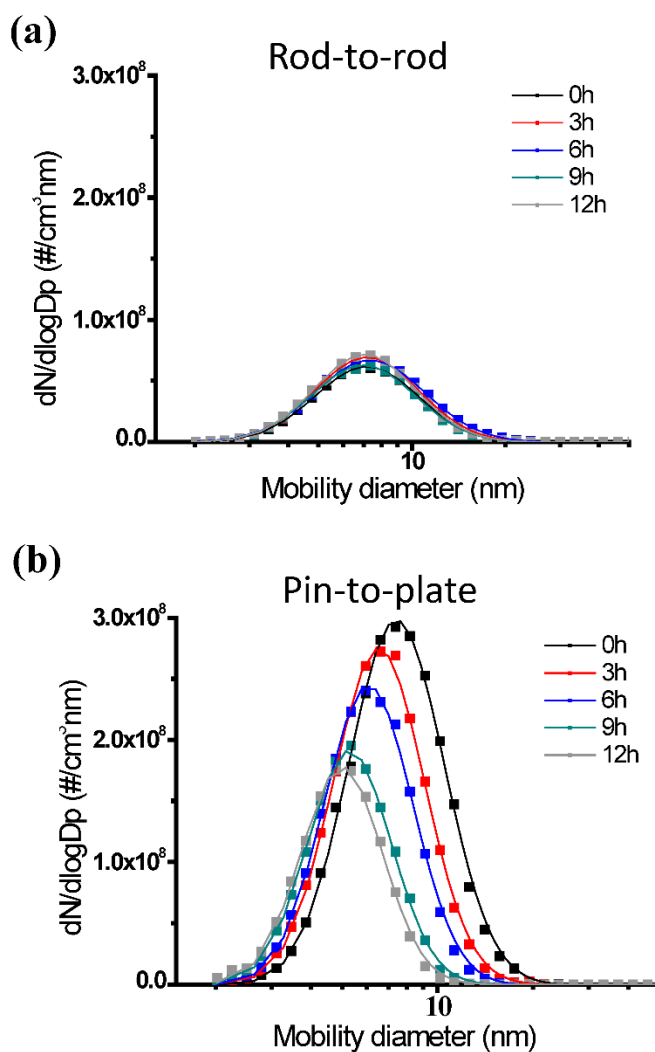


**Figure 3.4. Size distribution of Ag nanoparticles generated via two different types of spark discharge generator measured every 3 hours. (a) rod-to-rod type SDG (b) pin-to-plate type SDG.**

To investigate why the size distribution of PP-SDG generated particles gradually change over time, the tip shape of the pin electrode and spark characteristics were measured. During the spark discharge process, the tip of the pin electrode was eroded, consequently increasing both the radius of curvature of the pin electrode and the distance between the pin and the plate electrode.

Figure 3.5(a) ~ (e) show the changes in the shape of the pin electrode. The sharp pin electrode with 0.12 mm radius of curvature (Figure 3.4(a)) was eroded, thus the gap distance increased and the shape of the tip became blunt. The increase in the radius of curvature of the pin electrode and in the gap distance between the two electrodes affects the discharge characteristics such as discharge voltage and spark frequency. Due to these factors, increased electric field is required to produce sparks between the pin and the plate electrode, so consequently the discharge voltage gets increased. The electric potential of the electrode for RC circuit is defined as  $V_{electrode}(t) = V_{input}(1 - \exp(-t/RC))$ , where  $V_{input}$  is the output voltage of the power supply. As the resistance and the capacitance of the circuit are the same, increased discharge voltage requires more time for spark formation, which leads to a reduction in the spark discharge frequency.

Figure 3.5(f) shows that the measured discharge voltage ( $V_{discharge}$ ) increased from 3 kV at 0 hour to 4.2 kV after 12 hours and the spark frequency decreased from 101 Hz to 55.4 Hz during the time. Single spark

discharge energy which is expressed as  $E_{spark} = (1/2)C_{ext}V_{discharge}^2$ , where  $V_{discharge}$  is the voltage required to cause spark discharge, increased due to larger  $V_{discharge}$ . The spark discharge power is expressed as the product of the spark discharge energy and its frequency. The spark discharge power remained almost constant during the experiment. This means that the spark energy is dispersed in larger volumes as the gap between the two electrodes increases, and less energy is used for the evaporation of the electrodes. The decreased concentration of vaporized metal atoms causes the reduction in particle number concentration. In conclusion, tip erosion and gap distance increase can explain why the PP-SDG produces smaller particles as time passes whereas the RR-SDG produced particles with a constant size distribution regardless of the elapsed time.

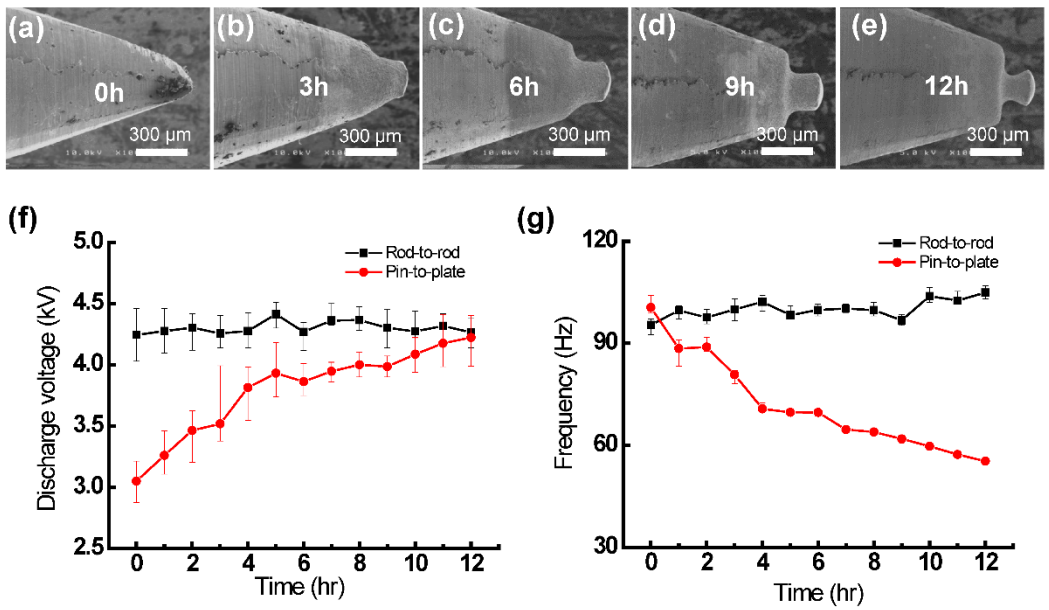


**Figure 3.5. (a) ~ (e) Morphological changes in the tip of the pin electrode in a pin-to-plate type SDG. Changes in (f) spark discharge voltage and (g) frequency versus time for both SDGs.**

### **3.4.2. 12-hour Continuous Generation of Ag Nanoparticles using Wire-in-Hole Type Spark Discharge Generator**

To maintain the fast local carrier gas velocity of the PP-SDG and to suppress the shape change of the positive electrode at the same time, we designed a new type of spark discharge chamber, called the wire-in-hole type spark discharge generator (WH-SDG) which exploits a metal wire located in the center of an exit hole in the plate. The size distribution and the morphology of particles generated by WH-SDG are depicted in Figure 3.6.

The size distribution did not change significantly for 12 hours, with  $d_g$  of 5.5 nm and  $\sigma_g$  of 1.35 maintaining the high number concentration of  $7.34 \times 10^7 \text{ \#/cm}^3$  as measured by an SMPS (Figure 3.6(c)). The TEM images of the particles after 0 hour and 12 hours elapsed confirm that the particle size distribution did not change. The particle size distributions from the TEM image were well consistent with that from SMPS measurements. The geometrical configuration of the WH-SDG can effectively restrain the change in the gap distance, and the changes in the electrode geometry were relatively insignificant. Thus, it was demonstrated that the WH-SDG can generate the unagglomerated nanoparticles with high number concentration consistently for several hours.

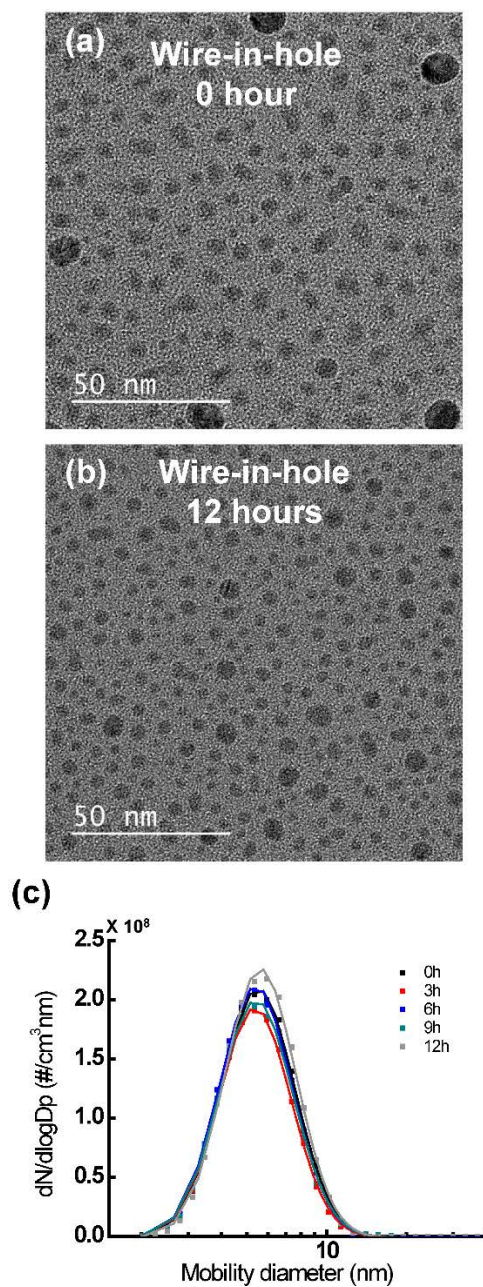


**Figure 3.6. Ag nanoparticles produced via wire-in-hole type SDG. (a) A TEM image of nanoparticles at the beginning. (b) A TEM image of nanoparticles after 12 hours from the beginning. (c) Size distributions of produced nanoparticles measured every 3 hours.**

Figure 3.7 (a) ~ (e) are the images of the wire electrode over time. The wire electrode was worn in the radial direction in the region less than 100  $\mu\text{m}$  from the tip. The spark discharge occurred at various points around the gap of the wire and the grounded plate, which resulted in evenly distributed sparks around the whole surface of the wire electrode. Since the surface area of the electrode subject to erosion is larger than that of the PP-SDG, the WH-SDG can maintain consistent spark discharge characteristics for a longer time. The discharge voltage and the spark frequency of the WH-SDG were measured with an oscilloscope. The discharge voltage ( $V_{\text{discharge}}$ ) stayed at approximately 3.28 kV and the spark frequency was stayed at approximately 90.8 Hz for 12 hours with small fluctuations ( $\pm 0.13$  kV and  $\pm 3.7$  Hz respectively), as shown in Fig 3.7(f) and 3.7(g).

The particle size distributions obtained from various types of the spark discharge generators for 12 hours are plotted in Figure 3.8. In addition to the PP-SDG and the WH-SDG, the wire-to-plate spark discharge generator (WP-SDG, see Figure 3.2(d)) was tested in the experiment to exclude the effects of tip shape changes, and determine the influence of the gap distance changes more clearly. From Figure 3.8(a), the geometric mean diameter of the WH-SDG was maintained at 5.5 nm for 12 hours, but in the case of the PP-SDG and the WP-SDG, the  $d_g$  were decreased from 7.32 to 4.90 nm, and from 7.72 to 4.60 nm, respectively. There was a similar trend for the number concentration. The WH-SDG showed the high number concentration of  $7.34 \times 10^7 \text{ \#/cm}^3$  steadily, while the number concentration of the PP-SDG and the

WP-SDG decreased (Figure 3.8(b)). The total number concentration of the PP-SDG was initially  $1.12 \times 10^8 \text{ \#/cm}^3$  and decreased to  $5.70 \times 10^7 \text{ \#/cm}^3$ . In the case of the WP-SDG, the total number concentration also decreased from  $1.30 \times 10^8 \text{ \#/cm}^3$  to  $3.59 \times 10^7 \text{ \#/cm}^3$ . This shows that the PP-SDG showed decreasing size distribution due to the change in both the tip shape and the gap distance. The increasing gap distance can reduce the particle size and quantity, which can be inferred from the case of the WP-SDG.

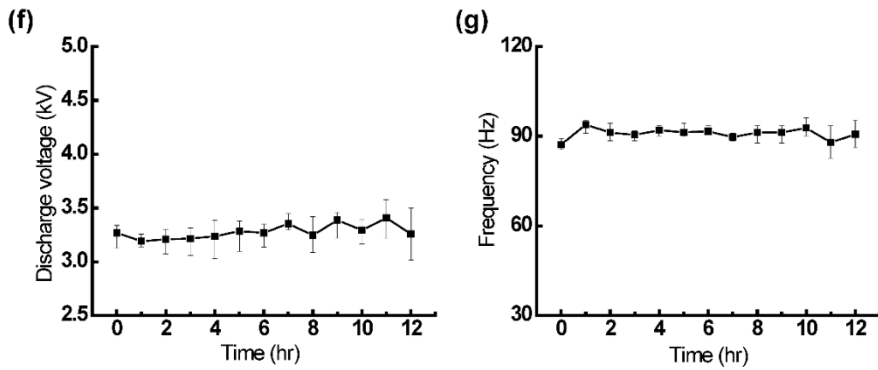
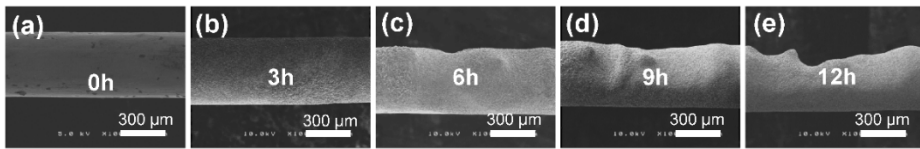


**Figure 3.7. (a) ~ (e) Morphological changes in the wire electrode in wire-in-hole type SDG. Changes in (f) spark discharge voltage and (g) frequency versus time for WH-SDG.**

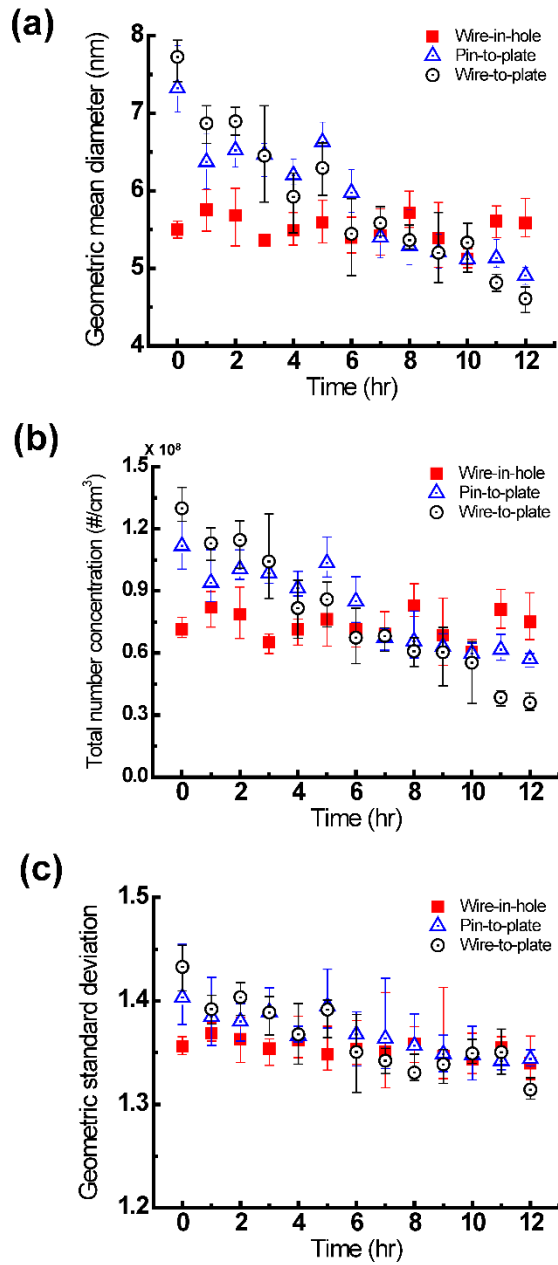


**Figure 3.8. Characteristics of particles generated via WH-SDG, PP-SDG and WP-SDG versus time. (a) Geometric mean diameter. (b) Total number concentration. (c) Geometric standard deviation.**

### 3.4.3. Control of Particle Size Distribution and Synthesis of Various Metal Nanoparticles

In order to utilize the generated nanoparticles as building blocks for nanostructures, it is important to control the size of the generated particles. Thus, we conducted an additional experiment for controlling particle sizes with respect to gas flow rate. Since the increased gas flow rate enhances cooling and dilution rate (Lehtinen and Zachariah, 2002; Tabrizi et al., 2009), the size of the generated nanoparticles is sensitive to the flow rate of the carrier gas. Hence, we measured the size distribution with using different carrier gas flow rates of 1 lpm, 2 lpm and 4 lpm. The discharge voltage and spark frequency of all experiments were maintained during the particle generation.

As shown in Figure 3.9, the particle diameter became smaller as the gas flow rate increased. The average mobility diameter is 6.50 nm, 5.51 nm and 5.15 nm for 1 lpm, 2 lpm and 4 lpm, respectively. For the flow rate of 1 lpm, the particle diameter was obviously larger than that of the case for 2 lpm due to the difference in residence time. But the difference in diameter between 2 lpm and 4 lpm cases was somewhat smaller than that between 1 lpm and 2 lpm cases. The geometric standard deviation of size distribution for 1 lpm condition was 1.38 and was slightly higher than the size distribution of 2 lpm condition ( $\sigma_g = 1.35$ ) as shown in Figure 3.9(c). The difference of  $\sigma_g$  between 2 lpm and 4 lpm cases was much smaller than that between 1 lpm and 2 lpm cases. These results imply that lower flow rate can make larger particles and

may cause agglomeration but the effect is insignificant. (Tabrizi et al., 2009) If the flow rate increases, the diameters of the generated particles become smaller because higher transport velocity in particle growth regions can lower the probability of aggregation (Han et al., 2012).

To show the versatility of the system, other materials such as copper and palladium were used in the WH-SDG as electrodes and the performance evaluation was carried out (Figure 3.10). The experimental conditions were set for generating nanoparticles of 5 nm in diameter. In the case of silver and copper, the electric circuit was comprised of a 5 M $\Omega$  charging resistor and a 2nF external capacitor. For palladium nanoparticles, the resistance and the capacitance of the circuit were 20 M $\Omega$  and 1 nF, respectively. The gas flow rate for Pd particle generation was set at 3 lpm to avoid agglomeration. As shown in Figure 3.10, the size distributions were maintained with little fluctuation. The average geometric standard deviations were 1.35, 1.32 and 1.31 for silver, copper and palladium, respectively.

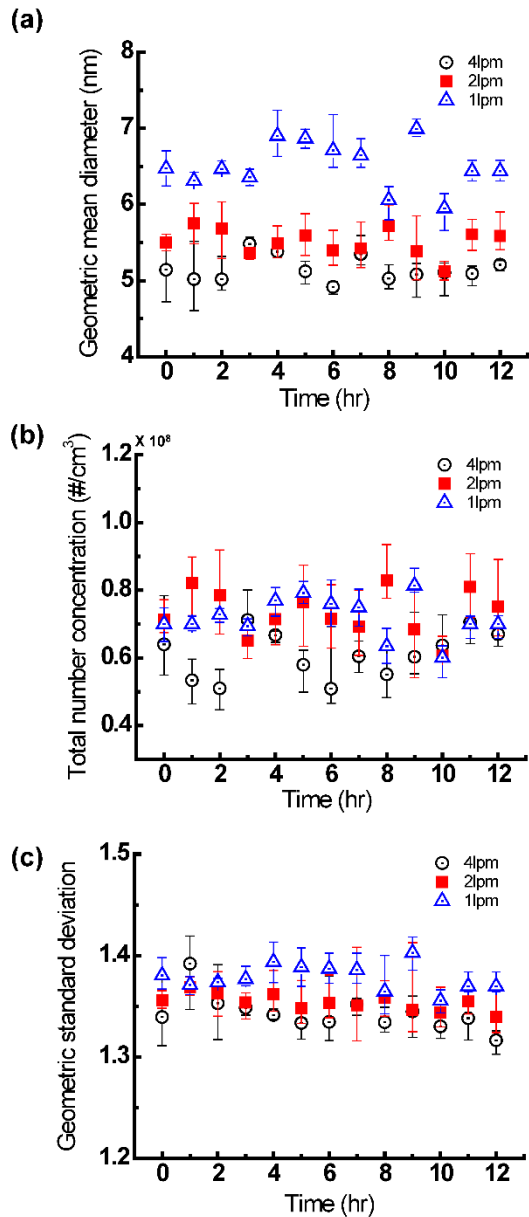


**Figure 3.9. Size distributions of generated nanoparticles with different gas flow rate. (a) Geometric mean diameter. (b) Total number concentration (c) Geometric standard deviation**

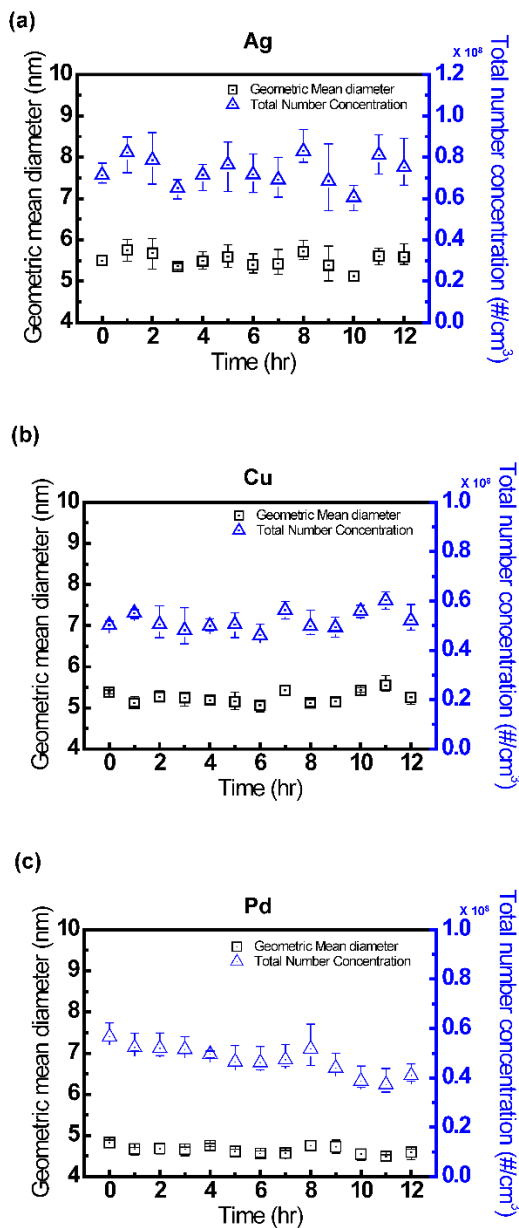


**Figure 3.10. Geometric mean diameters and total number concentrations of various metal nanoparticles generated by WH-SDG over 12 hours. (a) Silver (b) Copper (c) Palladium**

### 3.5. Conclusion

In this study, we developed and evaluated a new type of SDG, in which a metal wire was used as an electrode and the wire electrode was designed to be located in the center of the hole on the grounded plate electrode. Using this wire-in-hole type SDG, it was possible not only to generate unagglomerated nanoparticles with high concentration, but also to show more consistent size distributions for longer operations than the previous pin-to-plate type SDG. The change in the particle size distribution of the PP-SDG over time was found to be due to the changes in the geometry of the pin electrode caused by repetitive spark discharges. The transformed electrode geometry led to the change in spark discharge characteristics such as spark discharge voltage and frequency which could directly influence the generation of nanoparticles. On the other hand, the WH-SDG could effectively suppress the change of gap distance and the shape of the electrode and, hence, maintain its spark discharge properties for a longer time.

Further, to control the diameter of the generated nanoparticles, we carried out experiments varying the flow rates of the carrier gas. As expected, the increasing flow rates from 1 lpm to 4 lpm could produce smaller diameters of nanoparticles. In addition, WH-SDG was able to produce and maintain unagglomerated metal nanoparticles such as Ag, Cu and Pd for a long time.

Thus, the WH-SDG has a novel advantage over other electrode configurations as it can produce small and unagglomerated nanoparticles consistently for several hours. This capability will be especially advantageous

for utilization of produced nanoparticles as building blocks to fabricate nanostructures with complex morphologies.



## **Chapter 4.**

### **Concluding Remarks**

In order to expand the aerosol-based gas phase nanoparticle synthesis method, we established the selective production of magnesium oxide nanoparticles having different morphologies and investigated the optical properties. Moreover, the wire-in-hole type spark discharge generator was introduced to generate sub-10 nm particles consistently.

Using the flame metal combustion method, we discovered the parameters for selectively producing the terraced MgO nanoparticles, which have distinguished morphology and properties compared to general cubic MgO nanoparticles. The flame conditions for producing large proportion of terraced MgO nanoparticles were found and the short flame condition with oxygen carrier gas which was more abundant of oxygen was adequate for producing terrace-shaped MgO particles. With argon carrier gas, otherwise, the cubic MgO nanoparticles were mainly generated. Thus, it is found that the selectivity of produced MgO nanoparticles was determined with changing the flame conditions. For investigating the growth condition of nanoparticles, the particle size distribution of the produced MgO nanoparticles was also measured from electron microscope images. From those results, it could be concluded that optimized conditions for producing terraced and spherical MgO nanoparticles were established.

In Chapter 3, we demonstrated a wire-in-hole type spark discharge generator, which consists of a metal wire electrode and a grounded plate electrode with a hole, could produce sub-10 nm nanoparticles preventing from the change of the particle size distribution over time that exists on the rod-to-

rod and the pin-to-plate type spark discharge method. The newly developed WH-SDG could not only produce nanoparticles unagglomerated primary nanoparticles, but also to show more consistent size distribution for long hours than the previous pin-to-plate type SDG. From the study of long-time operation of the SDG, the change in the geometry of the pin electrode caused by repetitive spark discharge resulted the change in the particle size distribution of the PP-SDG with the lapse of time. The gap size between electrodes and the morphology of electrode geometry could change in spark discharge characteristics such as spark discharge voltage and frequency which could directly influence the generation of nanoparticles. On the other hand, the WH-SDG could effectively suppress the geometrical changes such as gap distance and the shape of the tip of the electrode. Thus the WH-SDG could maintain its spark discharge properties which were highly affected by the geometrical conditions of electrodes for 12 hour generation experiment.

## References

- Altman, I. S., Pikhitsa, P. V., and Choi, M. (2004). Key Effects in Nanoparticle Formation by Combustion Techniques. C. Granqvist, L. Kish, & W. Marlow (Eds.). In *Gas Phase Nanoparticle Synthesis* (pp. 43-67). Springer Netherlands.
- Altman, I. S., Pikhitsa, P. V., Choi, M., Song, H.-J., Nasibulin, A. G., and Kauppinen, E. I. (2003). Zero-phonon lines in the photoluminescence spectra of MgO:Mn<sup>2+</sup> nanocrystals. *Physical Review B*, 68 (12), 125324.
- Aritani, H., Yamada, H., Nishio, T., Shiono, T., Imamura, S., Kudo, M., Hasegawa, S., Tanaka, T., and Yoshida, S. (2000). Characterization of Li-doped MgO catalysts for oxidative coupling of methane by means of MgK-edge XANES. *Journal of Physical Chemistry B*, 104 (44), 10133-10143.
- Arndt, S., Laugel, G., Levchenko, S., Horn, R., Baerns, M., Scheffler, M., Schlogl, R., and Schomacker, R. (2011). A Critical Assessment of Li/MgO-Based Catalysts for the Oxidative Coupling of Methane. *Catalysis Reviews-Science and Engineering*, 53 (4), 424-514.
- Bau, S., Witschger, O., Gensdarmes, F., Thomas, D., and Borra, J. P. (2010). Electrical properties of airborne nanoparticles produced by a commercial spark-discharge generator. *Journal of Nanoparticle Research*, 12 (6), 1989-1995.
- Beaucage, G., Kammler, H. K., Mueller, R., Strobel, R., Agashe, N., Pratsinis, S. E., and Narayanan, T. (2004). Probing the dynamics of nanoparticle growth in a flame using synchrotron radiation. *Nature Materials*, 3 (6),

370-374.

- Buesser, B., and Pratsinis, S. E. (2012). Design of Nanomaterial Synthesis by Aerosol Processes. *Annual Review of Chemical and Biomolecular Engineering, Vol 3, 3*, 103-127.
- Byeon, J. H., Park, J. H., and Hwang, J. H. (2008). Spark generation of monometallic and bimetallic aerosol nanoparticles. *Journal of Aerosol Science, 39* (10), 888-896.
- Cai, H., Chaudhary, N., Lee, J., Becker, M. F., Brock, J. R., and Keto, J. W. (1998). Generation of metal nanoparticles by laser ablation of microspheres. *Journal of Aerosol Science, 29* (5-6), 627-636.
- Cao, C. Y., Qu, J., Wei, F., Liu, H., and Song, W. G. (2012). Superb Adsorption Capacity and Mechanism of Flowerlike Magnesium Oxide Nanostructures for Lead and Cadmium Ions. *ACS Applied Materials & Interfaces, 4* (8), 4283-4287.
- Chae, S., Lee, D., Kim, M. C., Kim, D. S., and Choi, M. (2015). Wire-in-Hole-Type Spark Discharge Generator for Long-Time Consistent Generation of Unagglomerated Nanoparticles. *Aerosol Science and Technology, 49* (7), 463-471.
- Chae, S., Pikhitsa, P. V., Shin, S., Kim, C. H., Jung, S., and Choi, M. (2015). Formation of non-cubic nanoparticles from cubic MgO in intensified self-burning of magnesium (Publication no. arXiv:1511.08554).
- Cho, J., and Choi, M. (2000). Determination of number density, size and morphology of aggregates in coflow diffusion flames using light scattering and local sampling. *Journal of Aerosol Science, 31* (9), 1077-1095.

- Dhal, J. P., Sethi, M., Mishra, B. G., and Hota, G. (2015). MgO nanomaterials with different morphologies and their sorption capacity for removal of toxic dyes. *Materials Letters*, *141*, 267-271.
- Ding, Y., Zhang, G. T., Wu, H., Hai, B., Wang, L. B., and Qian, Y. T. (2001). Nanoscale magnesium hydroxide and magnesium oxide powders: Control over size, shape, and structure via hydrothermal synthesis. *Chemistry of Materials*, *13* (2), 435-440.
- Feldheim, D. L., and Foss, C. A. (2001). *Metal nanoparticles: synthesis, characterization, and applications*: CRC Press.
- Geneste, G., Morillo, J., Finocchi, F., and Hayoun, M. (2007). Primary nucleation processes in binary oxide growth: The case of MgO. *Surface Science*, *601* (23), 5616-5627.
- Grossmann, H. K., Grieb, T., Meierhofer, F., Hodapp, M. J., Noriler, D., Gröhn, A., Meier, H. F., Fritsching, U., Wegner, K., and Mädler, L. (2015). Nanoscale mixing during double-flame spray synthesis of heterostructured nanoparticles. *Journal of Nanoparticle Research*, *17* (4), 1-16.
- Ha, K., Choi, H., Jung, K., Han, K., Lee, J. K., Ahn, K., and Choi, M. (2014). Large-area assembly of three-dimensional nanoparticle structures via ion assisted aerosol lithography with a multi-pin spark discharge generator. *Nanotechnology*, *25* (22).
- Hacquart, R., and Jupille, J. (2009). Morphology of MgO smoke crystallites upon etching in wet environment. *Journal of Crystal Growth*, *311* (21), 4598-4604.
- Han, K., Kim, W., Yu, J., Lee, J., Lee, H., Woo, C. G., and Choi, M. (2012). A study of pin-to-plate type spark discharge generator for producing

- unagglomerated nanoaerosols. *Journal of Aerosol Science*, 52, 80-88.
- Horvath, H., and Gangl, M. (2003). A low-voltage spark generator for production of carbon particles. *Journal of Aerosol Science*, 34 (11), 1581-1588.
- Huang, T., Nallathamby, P. D., and Xu, X.-H. N. (2008). Photostable Single-Molecule Nanoparticle Optical Biosensors for Real-Time Sensing of Single Cytokine Molecules and Their Binding Reactions. *Journal of the American Chemical Society*, 130 (50), 17095-17105.
- Jung, K., Hahn, J., In, S., Bae, Y., Lee, H., Pikhitsa, P. V., Ahn, K., Ha, K., Lee, J. K., Park, N., and Choi, M. (2014). Hotspot-Engineered 3D Multipetal Flower Assemblies for Surface-Enhanced Raman Spectroscopy. *Advanced Materials*, 26 (34), 5924-+.
- Kala, S., Theissmann, R., and Kruis, F. E. (2013). Generation of AuGe nanocomposites by co-sparking technique and their photoluminescence properties. *Journal of Nanoparticle Research*, 15 (9).
- Karch, J., Birringer, R., and Gleiter, H. (1987). Ceramics Ductile at Low-Temperature. *Nature*, 330 (6148), 556-558.
- Kim, H., Kim, J., Yang, H. J., Suh, J., Kim, T., Han, B. W., Kim, S., Kim, D. S., Pikhitsa, P. V., and Choi, M. (2006). Parallel patterning of nanoparticles via electrodynamic focusing of charged aerosols. *Nature Nanotechnology*, 1 (2), 117-121.
- Krinke, T. J., Fissan, H., Deppert, K., Magnusson, M. H., and Samuelson, L. (2001). Positioning of nanometer-sized particles on flat surfaces by direct deposition from the gas phase. *Applied Physics Letters*, 78 (23), 3708-3710.

- Kruis, F. E., Fissan, H., and Peled, A. (1998). Synthesis of nanoparticles in the gas phase for electronic, optical and magnetic applications - A review. *Journal of Aerosol Science*, 29 (5-6), 511-535.
- Lee, D., and Choi, M. (2002). Coalescence enhanced synthesis of nanoparticles to control size, morphology and crystalline phase at high concentrations. *Journal of Aerosol Science*, 33 (1), 1-16.
- Lee, H., Lee, D.-H., Song, Y.-H., Choi, W. C., Park, Y.-K., and Kim, D. H. (2015). Synergistic effect of non-thermal plasma-catalysis hybrid system on methane complete oxidation over Pd-based catalysts. *Chemical Engineering Journal*, 259, 761-770.
- Lee, H., You, S., Pikhitsa, P. V., Kim, J., Kwon, S., Woo, C. G., and Choi, M. (2011). Three-Dimensional Assembly of Nanoparticles from Charged Aerosols. *Nano Letters*, 11 (1), 119-124.
- Lee, J., Altman, I., and Choi, M. (2008). Design of thermophoretic probe for precise particle sampling. *Journal of Aerosol Science*, 39 (5), 418-431.
- Lehtinen, K. E. J., and Zachariah, M. R. (2002). Energy accumulation in nanoparticle collision and coalescence processes. *Journal of Aerosol Science*, 33 (2), 357-368.
- Li, M. J., Guo, W. L., Li, H. J., Dai, W., and Yang, B. H. (2014). Electrochemical bio sensor based on one-dimensional MgO nanostructures for the simultaneous determination of ascorbic acid, dopamine, and uric acid. *Sensors and Actuators B-Chemical*, 204, 629-636.
- Lunsford, J. H. (1995). The Catalytic Oxidative Coupling of Methane. *Angewandte Chemie-International Edition in English*, 34 (9), 970-980.

- Mädler, L., Kammler, H. K., Mueller, R., and Pratsinis, S. E. (2002). Controlled synthesis of nanostructured particles by flame spray pyrolysis. *Journal of Aerosol Science*, 33 (2), 369-389.
- Messing, M. E., Dick, K. A., Wallenberg, L. R., and Deppert, K. (2009). Generation of size-selected gold nanoparticles by spark discharge - for growth of epitaxial nanowires. *Gold Bulletin*, 42 (1), 20-26.
- Meuller, B. O., Messing, M. E., Engberg, D. L. J., Jansson, A. M., Johansson, L. I. M., Norlen, S. M., Tureson, N., and Deppert, K. (2012). Review of Spark Discharge Generators for Production of Nanoparticle Aerosols. *Aerosol Science and Technology*, 46 (11), 1256-1270.
- Mishakov, I. V., Bedilo, A. F., Richards, R. M., Chesnokov, V. V., Volodin, A. M., Zaikovskii, V. I., Buyanov, R. A., and Klabunde, K. J. (2002). Nanocrystalline MgO as a dehydrohalogenation catalyst. *Journal of Catalysis*, 206 (1), 40-48.
- Moodie, A. F., and Warble, C. E. (1971). Electron microscopic investigations of MgO morphology and surfaces. *Journal of Crystal Growth*, 10 (1), 26-38.
- Mullins, W. W. (1957). Theory of Thermal Grooving. *Journal of Applied Physics*, 28 (3), 333-339.
- Muraoka, T., Kashimura, T., and Iizuka, S. (2009). Spherical MgO microparticle deposition by RF impulse discharge with small coaxial electrodes. *Thin Solid Films*, 518 (3), 1012-1015.
- Nagappa, B., and Chandrappa, G. T. (2007). Mesoporous nanocrystalline magnesium oxide for environmental remediation. *Microporous and Mesoporous Materials*, 106 (1-3), 212-218.

- Nalwa, H. S. (1999). *Handbook of Nanostructured Materials and Nanotechnology, Five-Volume Set* (Vol. 3): Academic Press.
- Newman, R. N., and Payne, J. F. B. (1987). The Anomalous Brightness of Magnesium Air Flames. *Combustion and Flame*, 68 (1), 31-41.
- Pacchioni, G., Clotet, A., and Ricart, J. M. (1994). A theoretical study of the adsorption and reaction of SO<sub>2</sub> at surface and step sites of the MgO(100) surface. *Surface Science*, 315 (3), 337-350.
- Pacchioni, G., and Maria Ferrari, A. (1999). Surface reactivity of MgO oxygen vacancies. *Catalysis Today*, 50 (3-4), 533-540.
- Park, K. T., Farid, M. M., and Hwang, J. (2014). Anti-agglomeration of spark discharge-generated aerosols via unipolar air ions. *Journal of Aerosol Science*, 67, 144-156.
- Patil, K. C., Aruna, S. T., and Mimani, T. (2002). Combustion synthesis: an update. *Current Opinion in Solid State and Materials Science*, 6 (6), 507-512.
- Pfeiffer, T. V., Feng, J., and Schmidt-Ott, A. (2014). New developments in spark production of nanoparticles. *Advanced Powder Technology*, 25 (1), 56-70.
- Pikhitsa, P. V., Kim, C., Chae, S., Shin, S., Jung, S., Kitaura, M., Kimura, S., Fukui, K., and Choi, M. (2015). Two-band luminescence from an intrinsic defect in spherical and terraced MgO nanoparticles. *Applied Physics Letters*, 106 (18), 183106.
- Portillo, R., Lopez, T., Gomez, R., Bokhimi, Morales, A., and Novaro, O. (1996). Magnesia synthesis via sol-gel: Structure and reactivity. *Langmuir*, 12 (1), 40-44.

- Pratsinis, S. E. (1998). Flame aerosol synthesis of ceramic powders. *Progress in Energy and Combustion Science*, 24 (3), 197-219.
- Pratsinis, S. E. (2010). Aerosol-based Technologies in Nanoscale Manufacturing: from Functional Materials to Devices through Core Chemical Engineering. *Aiche Journal*, 56 (12), 3028-3035.
- Rao, N. P., Tymiak, N., Blum, J., Neuman, A., Lee, H. J., Girshick, S. L., McMurry, P. H., and Heberlein, J. (1998). Hypersonic plasma particle deposition of nanostructured silicon and silicon carbide. *Journal of Aerosol Science*, 29 (5-6), 707-720.
- Raouf, F., Taghizadeh, M., and Yousefi, M. (2013). Activity enhancement of Li/MgO catalysts by lithium chloride as a lithium precursor for the oxidative coupling of methane. *Reaction Kinetics Mechanisms and Catalysis*, 110 (2), 373-385.
- Refson, K., Wogelius, R. A., Fraser, D. G., Payne, M. C., Lee, M. H., and Milman, V. (1995). Water chemisorption and reconstruction of the MgO surface. *Physical Review B*, 52 (15), 10823-10826.
- Roth, C., Ferron, G. A., Karg, E., Lentner, B., Schumann, G., Takenaka, S., and Heyder, J. (2004). Generation of ultrafine particles by spark discharging. *Aerosol Science and Technology*, 38 (3), 228-235.
- Scheer, E. (2010). *Molecular electronics: an introduction to theory and experiment* (Vol. 1): World Scientific.
- Schwyn, S., Garwin, E., and Schmidtott, A. (1988). Aerosol Generation by Spark Discharge. *Journal of Aerosol Science*, 19 (5), 639-642.
- Shluger, A. L., Sushko, P. V., and Kantorovich, L. N. (1999). Spectroscopy of low-coordinated surface sites: Theoretical study of MgO. *Physical*

*Review B*, 59 (3), 2417-2430.

Siegel, R. W. (1993). Nanophase Materials Assembled from Atom Clusters. *Materials Science and Engineering B-Solid State Materials for Advanced Technology*, 19 (1-2), 37-43.

Stankic, S., Cottura, M., Demaille, D., Noguera, C., and Jupille, J. (2011). Nucleation and growth concepts applied to the formation of a stoichiometric compound in a gas phase: The case of MgO smoke. *Journal of Crystal Growth*, 329 (1), 52-56.

Stavale, F., Nilius, N., and Freund, H.-J. (2012). Cathodoluminescence of near-surface centres in Cr-doped MgO(001) thin films probed by scanning tunnelling microscopy. *New Journal of Physics*, 14 (3), 033006.

Sterrerr, M., Heyde, M., Novicki, M., Nilius, N., Risse, T., Rust, H. P., Pacchioni, G., and Freund, H. J. (2006). Identification of color centers on MgO(001) thin films with scanning tunneling microscopy. *Journal of Physical Chemistry B*, 110 (1), 46-49.

Strobel, R., and Pratsinis, S. E. (2007). Flame aerosol synthesis of smart nanostructured materials. *Journal of Materials Chemistry*, 17 (45), 4743-4756.

Sung, H., Lee, J., Han, K., Lee, J. K., Sung, J., Kim, D., Choi, M., and Kim, C. (2014). Controlled positioning of metal nanoparticles in an organic light-emitting device for enhanced quantum efficiency. *Organic Electronics*, 15 (2), 491-499.

Tabrizi, N. S., Ullmann, M., Vons, V. A., Lafont, U., and Schmidt-Ott, A. (2009). Generation of nanoparticles by spark discharge. *Journal of Nanoparticle Research*, 11 (2), 315-332.

- Thimsen, E., and Biswas, P. (2007). Nanostructured photoactive films synthesized by a flame aerosol reactor. *Aiche Journal*, 53 (7), 1727-1735.
- Tricoli, A., and Pratsinis, S. E. (2010). Dispersed nanoelectrode devices. *Nat Nano*, 5 (1), 54-60.
- Wang, J. A., Novaro, O., Bokhimi, X., Lopez, T., Gomez, R., Navarrete, J., Llanos, M. E., and LopezSalinas, E. (1997). Structural defects and acidic and basic sites in sol-gel MgO. *Journal of Physical Chemistry B*, 101 (38), 7448-7451.
- Yang, S., Jang, Y. H., Kim, C. H., Hwang, C., Lee, J., Chae, S., Jung, S., and Choi, M. (2010). A flame metal combustion method for production of nanoparticles. *Powder Technology*, 197 (3), 170-176.
- Yang, S. S., Yi, J. H., Son, S., Jang, J., Altman, I. S., Pikhitsa, P. V., and Choi, M. (2003). Fragmentation of Fe<sub>2</sub>O<sub>3</sub> nanoparticles driven by a phase transition in a flame and their magnetic properties. *Applied Physics Letters*, 83 (23), 4842-4844.
- You, S., Han, K., Kim, H., Lee, H., Woo, C. G., Jeong, C., Nam, W., and Choi, M. (2010). High-Resolution, Parallel Patterning of Nanoparticles via an Ion-Induced Focusing Mask. *Small*, 6 (19), 2146-2152.
- Zachariah, M. R., Mcmillin, B., and Shull, R. D. (1995). Synthesis and in-Situ Characterization of Superparamagnetic Nanocomposites from Vapor-Phase Condensation. *Abstracts of Papers of the American Chemical Society*, 210, 18-Pmse.
- Zolotko, A. N., Poletaev, N. I., Vovchuk, J. I., and Florko, A. V. (2004). Nanoparticle Formation by Combustion Techniques. In *Gas Phase Nanoparticle Synthesis* (pp. 123-156). Springer.

# 화염금속연소법과 스파크방전법을 이용한 기능성 나노입자 합성

서울대학교 대학원 기계항공공학부

채 석 병

나노입자는 벌크 상태의 물질과는 다른 고유의 특성을 갖고 이러한 나노입자를 합성하기 위한 기법은 나노기술의 주된 연구분야 중 하나이다. 다양한 종류의 나노재료가 전자, 광학, 촉매, 에너지 및 바이오 공학 분야에 응용되고 있어 우수한 특성을 갖는 나노재료의 효율적인 합성 기법에 대한 연구가 필요가 높아지고 있다. 현재까지 다양한 종류의 나노입자 합성 기법이 보고되었으며, 기능성 나노재료의 합성을 위해 적용되고 있다. 이 중, 에어로졸 기반의 기상 합성법은 이러한 나노재료를 합성하기에 보다 청정하고 효율적인 기법 중 하나로 여겨진다. 이는 현존하는 졸-겔 방법에서 만족시키기 어려운 부분으로, 전기 방전, 레이저 어블레이션, 증발-응축, 화염 연소법 등의 많은 에어로졸 기반의 기상합성법이 소개되고, 나노입자를 합성하는데 응용되고 있다. 이를 바탕으로, 본 연구에서는 형상과 특성이 다른 산화물 나노입자를 선택적으로 합성할 수 있는 화염 금속 연소법과 10 nm 이하의 나노입자를 장시간 안정적으로 생산할 수 있는 새로운 스파크 방전 장비를 이용한 스파크 방전법을 설명한다.

화염금속연소법은 기존의 수용액 상태의 전구체가 아닌 고체 분말 상태의 금속 분말을 전구체로 사용하여 이를 초고온의 수소-산소 확산화염에 주입하여 나노입자를 합성하는 기법으로, 손쉽고 효율적으로 나노입자를 합성할 수 있는 에어로졸 기반의 기상합성법이다. 화염금속연소법으로 산화아연, 산화마그네슘, 산화주석 등의 다양한 산화물 나노입자를 제조할 수 있다. 이 기법을 활용하여 산화 마그네슘 입자를 합성하였을 때, 기존의 산화마그네슘과 다른 음극발광 특성을 갖는 테라스/구형 산화마그네슘 나노입자가 생성되는 것을 발견하였다. 합성된 산화마그네슘 입자의 화염 위치별 입자 크기 분포를 측정하여 두 종류의 나노입자의 성장 메커니즘이 일반적인 정방형 입자와 다른 표면결함에 의한 빠른 성장임을 규명하였으며, 다른 종류의 이송 기체를 사용하여 산화마그네슘 나노입자를 합성하면 정방형 입자와 테라스/구형 입자가 생성되는 비율을 제어할 수 있음을 발견하였다. 또한 산화마그네슘 입자에 전이금속을 도핑하여, 금속 입자의 위치에 따라 음극 발광 특성이 달라지는 특성을 조사하였다.

스파크 방전법은 10 nm 이하의 입자를 제조할 수 있는 적절한 방법으로 여겨지고 있으며, 특히 나노패턴 제조를 위한 구성 입자로 활용되는 하전된 나노입자를 효율적으로 제조할 수 있는 기법이다. 스파크 방전은 방전 전극의 구성에 따라 입자가 생성되는 양상이 달라지는데, 일반적으로 사용되는 봉-봉 구조의 경우 국부적으로 생성 후의 유속이 적어 의도하지 않은 응집현상이 발생하는 것이 불가피하다. 반면에, 이전에 보고된 핀-판 구조의 경우 응집되지 않은 입자의 합성이 가능하나, 시간이 경과됨에 따라 전극이 마모되어 스파크 특성이 변하고 입자 크기분포가 변하는 현상이 있다. 이러한 문제를 해결하기 위해 선 전극을 판 전극의 가운데에 위치한 입자 출구에 위치시킨 새로운 전극 구조를

사용한 스파크 방전 장비를 개발하였다. 이는 전극의 기하학적인 변화와 전극간 거리 변화를 효율적으로 억제시켜 일정한 스파크 방전 전압과 방전 주파수를 장시간 유지하는 것이 가능하였고, 따라서 12시간 동안 입자의 크기분포 변화가 없이 안정적으로 나노입자를 발생시켰다. 이를 이용하여 입자 크기의 제어 실험 및 은, 구리, 팔라듐 등의 다양한 종류의 금속 나노입자를 제조하는 실험을 수행하였다.

**주요어:** 에어로졸기반 나노입자 합성; 화염금속연소법; 테라스 산화마그네슘 입자; 스파크 방전법; 선-구멍 구조 스파크 방전 입자 발생기

**학 번:** 2008-22895



저작자표시-비영리-변경금지 2.0 대한민국

이용자는 아래의 조건을 따르는 경우에 한하여 자유롭게

- 이 저작물을 복제, 배포, 전송, 전시, 공연 및 방송할 수 있습니다.

다음과 같은 조건을 따라야 합니다:



저작자표시. 귀하는 원저작자를 표시하여야 합니다.



비영리. 귀하는 이 저작물을 영리 목적으로 이용할 수 없습니다.



변경금지. 귀하는 이 저작물을 개작, 변형 또는 가공할 수 없습니다.

- 귀하는, 이 저작물의 재이용이나 배포의 경우, 이 저작물에 적용된 이용허락조건을 명확하게 나타내어야 합니다.
- 저작권자로부터 별도의 허가를 받으면 이러한 조건들은 적용되지 않습니다.

저작권법에 따른 이용자의 권리는 위의 내용에 의하여 영향을 받지 않습니다.

이것은 [이용허락규약\(Legal Code\)](#)을 이해하기 쉽게 요약한 것입니다.

[Disclaimer](#)

공학박사학위논문

# Synthesis of Functional Nanoparticles Using Flame Metal Combustion and Spark Discharge Method

화염금속연소법과 스파크 방전법을 이용한  
기능성 나노입자 합성

2016 년 2 월

서울대학교 대학원

기계항공공학부

채 석 병



# 화염금속연소법과 스파크방전법을 이용한 기능성 나노입자 합성

Synthesis of Functional Nanoparticles Using Flame  
Metal Combustion and Spark Discharge Method

지도교수 최 만 수

이 논문을 공학박사 학위논문으로 제출함

2015년 11월

서울대학교 대학원  
기계항공공학부  
채 석 병

채석병의 공학박사 학위논문을 인준함

2015년 12월

위원장 : 이 준 식 (인)

부위원장 : 최 만 수 (인)

위원 : 전 누 리

위원 : 고 승 환

위원 : 김 형 철





# **Synthesis of Functional Nanoparticles Using Flame Metal Combustion and Spark Discharge Method**

Sukbyung Chae

Department of Mechanical and Aerospace Engineering

The Graduate School

Seoul National University

## **Abstract**

Nanoparticles with unique properties have been widely studied and synthesizing methods of nanomaterials have been one of the main research field of nanotechnology. Various functional nanomaterials are utilized in electronics, photonics, catalysts, renewable energy devices and biotechnology. Up to now, various synthesis methods for nanoparticles have been reported and used to produce such functional nanomaterials. The aerosol-based gas phase synthesizing methods are considered as clean and efficient methods for producing those functional nanomaterials, which could not fully satisfied with existing sol-gel methods. Many of aerosol-based gas phase methods have been studied and used such as electrical discharge, laser ablation, evaporation-condensation and synthesizing in flame and each method has been studied and utilized to produce nanomaterials. With these motivation, in this thesis, we describe the method for synthesizing oxide nanoparticles with different properties with high selectivity and introduce a novel spark generator for stable sub-10 nm nanoparticle generation.

The flame metal combustion method, which utilizes solid metal powder as precursors and oxy-hydrogen diffusion flame of extremely high

temperature, is one of the facile and effective aerosol-based gas phase synthesizing method of nanoparticles. This method can be used for producing various oxide nanoparticles such as ZnO, MgO, SnO<sub>2</sub>. Using this method, we discovered that terraced and spherical MgO nanoparticles which have unique optical property could be generated. We investigated the optimized flame condition for the selective production of terraced and spherical MgO nanoparticles over conventional cubic ones. The size distribution of the produced MgO nanoparticles was measured to understand the growth condition of the nanoparticles. Furthermore, one was able to control the proportion of the morphology of generated MgO nanoparticles using different carrier gases. From the size distribution and the percentage of generated MgO nanoparticles, we found the dominant mechanism of terraced and spherical nanoparticles to be the fast surface defect-induced growth, which should be different from the growth mechanism of cubic MgO nanoparticles. We investigated the change of cathodoluminescence spectra of MgO nanoparticles doped with transition metals such as manganese and chromium to probe the nanoparticle morphology.

In order to generate sub-10 nm particles, spark discharge generation method is considered as an appropriate manner. Moreover, this method is a very effective method for producing charged aerosols which can be used as building blocks for nanofabrication. The electrode configuration in a spark discharge generator (SDG) plays a critical role in the characteristics of the process. For instance, the rod-to-rod configuration is unable to prevent nanoparticles from agglomerating due to slow local carrier gas velocity. On the other hand, the recently developed pin-to-plate configuration can produce unagglomerated nanoparticles, however, the geometric mean diameter and the number concentration of nanoparticles change over time as the pin gets eroded. To address the issue, a novel wire-in-hole type spark discharge generator (WH-SDG) that is able to generate unagglomerated nanoparticles with a constant size distribution over a long time was introduced. The WH-

SDG, which consists of a metal wire and a grounded plate with a hole in which the metal wire is located in the center, effectively suppressed changes in the electrode morphology and the gap distance, which cause the minimal variation of the spark discharge voltage and frequency in time. Therefore, the WH-SDG was able to maintain a constant size distribution of the generated nanoparticles for 12 hours. Additionally, it was found that the WH-SDG could control the diameter of nanoparticles by regulating the gas flow rate into the generator and produce nanoparticles out of various metals such as copper and palladium.

**Keywords: Aerosol-based nanoparticle synthesis; Flame metal combustion; Terraced MgO nanoparticles; Spark discharge; Wire-in-hole type spark discharge generator**

**Student Number: 2008-22895**

# Contents

<b>Abstract</b> .....	<b>i</b>
<b>List of Figures</b> .....	<b>vi</b>
<b>Nomenclature</b> .....	<b>x</b>
<b>Chapter 1. Introduction</b> .....	<b>1</b>
1.1. Background of Research .....	<b>2</b>
1.2. Objectives for Research .....	<b>6</b>
<b>Chapter 2. Flame Metal Combustion Method for Magnesium Oxide Nanoparticle Synthesis of Unique Morphology</b> .....	<b>9</b>
2.1. Introduction .....	<b>10</b>
2.2. Background of Research .....	<b>11</b>
2.2.1. Synthesis of MgO Nanoparticles .....	<b>11</b>
2.2.2. Flame Metal Combustion Method for Producing Oxide Nanoparticles .....	<b>14</b>
2.3. Experimental Details .....	<b>17</b>
2.4. Result and Discussions .....	<b>22</b>
2.4.1. Synthesis of Unique Terraced and Spherical MgO nanoparticles .....	<b>22</b>
2.4.2. Particle Size Distribution of MgO nanoparticles .....	<b>24</b>
2.4.3. Growth Mechanism of Terraced/spherical and cubic MgO nanoparticles .....	<b>38</b>
2.4.4. Cathodoluminescence of undoped and transition metal doped MgO nanoparticles .....	<b>45</b>

2.4.5. Oxidative Conversion of Methane Reaction of Flame-made MgO catalyst nanoparticles .....	49
2.5. Conclusion .....	53
<b>Chapter 3. Long-time Consistent Generation of sub-10 nm Nanoparticles using Wire-in-hole Type Spark Discharge Generator ...</b>	<b>55</b>
3.1. Introduction .....	56
3.2. Background of Research .....	58
3.2.1. Spark Discharge Nanoparticle Generator for Stable Nanoparticle Production .....	59
3.3. Experimental Details .....	60
3.4. Results and Discussion .....	66
3.4.1. Long-time Stability of Pin-to-Plate and Rod-to-Rod Type Spark Discharge Generator .....	67
3.4.2. 12-hour Continuous Generation of Ag Nanoparticles using Wire-in-Hole Type Spark Discharge Generator .....	72
3.4.3. Control of Particle Size Distribution and Synthesis of Various Metal Nanoparticles .....	78
3.5. Conclusion .....	84
<b>Chapter 4. Concluding Remarks .....</b>	<b>85</b>
<b>References .....</b>	<b>89</b>
<b>국문초록 .....</b>	<b>99</b>

## List of Figures

- Figure 2.1** (a) Schematic of flame metal combustion method (b) conventional metal combustion method.
- Figure 2.2.** Image of flame for synthesizing MgO nanoparticles. (a) Conventional Metal Combustion Method (self-ignition in ambient air) (b) Long flame ( $\text{H}_2 + \text{Ar}$  7+1 lpm,  $\text{O}_2$  2 lpm,  $\text{O}_2$  gas 1.5 lpm as carrier gas) (c) Middle-sized flame ( $\text{H}_2 + \text{Ar}$  4 lpm,  $\text{O}_2$  2 lpm,  $\text{O}_2$  gas 1.5 lpm as carrier gas) (d) Short flame with dilution gas ( $\text{H}_2 + \text{Ar}$  2+6 lpm,  $\text{O}_2$  2 lpm,  $\text{O}_2$  gas 1.5 lpm as carrier gas).
- Figure 2.3.** (a) TEM image of cube MgO nanoparticles (b) TEM image of Terraced MgO nanoparticles (c) X-ray diffraction of MgO nanoparticles. (d) Cathodoluminescence spectra of cube and terraced MgO
- Figure 2.4.** TEM images of nanoparticles synthesized from long flame condition ( $\text{H}_2 + \text{Ar}$  7+1 lpm,  $\text{O}_2$  2 lpm, carrier gas  $\text{O}_2$  1.5 lpm). Particles are collected at 10, 50, 100, 150, 200, 250 mm from the burner.
- Figure 2.5.** (a) Temperature distribution with the height in flame  $\text{H}_2/\text{Ar} = 7/1$  lpm along with the ratio of the number of terraced nanoparticles over cubic ones. (b) Diameters of terraced and cubic nanoparticles vs the height. The dashed zones in both plates mark the fast growth region of spherical nanoparticles. Dotted lines are guides for eye.
- Figure 2.6.** TEM images of nanoparticles synthesized from short flame condition ( $\text{H}_2 + \text{Ar}$  2+6 lpm,  $\text{O}_2$  2 lpm, carrier gas  $\text{O}_2$  1.5 lpm). Particles are collected at 10, 50, 100, 150, 200, 250 mm from the burner.
- Figure 2.7.** (a) Temperature distribution with the height in “short” flame ( $\text{H}_2/\text{Ar} = 2/6$  lpm) along with the ratio of the number of terraced nanoparticles over cubic ones. (b) Diameters of terraced and cubic nanoparticles vs the height in flame. The dashed zones in both plates mark the fast growth region of

spherical nanoparticles.

- Figure 2.8.** TEM images of nanoparticles generated varying the flowrate of fuel and dilution gas. Particles are collected at 250 mm from the burner.
- Figure 2.9.** (a) The ratio of terraced over cubic nanoparticles vs hydrogen flow rate. (b) Sizes of nanoparticles at 250 mm vs the flow rate of hydrogen for terraced and cubic nanoparticles. The dotted lines are guides for eye.
- Figure 2.10.** (a) TEM images of nanoparticles collected at different heights for argon carrier gas. (b) Proportion of terraced nanoparticles vs the height in flame for oxygen and argon carrier gas. (c) The CL spectra for nanoparticles produced with oxygen or argon carrier gases show very different light emission bands.
- Figure 2.11.** (a) TEM images of terraced nanoparticles reveal the proportionality law between the sizes of terraced nanoparticles vs the height of terrace steps. (b) The illustration of the growth mechanism that leads either to perfect spherical nanoparticles (mode II growth) or to terraced nanoparticles (when mode I growth follows mode II growth).
- Figure 2.12.** All possible cases of CL bands from cubic and terraced nanoparticles, including the dopant bands. Doping with  $\text{Cr}^{3+}$  ion produces characteristic 730 nm band with R and N zero phonon lines distinguished above 700 nm even at room temperature. Doping with  $\text{Mn}^{2+}$  may produce 610 nm and 750 nm bands.
- Figure 2.13.** (a) TEM image of flame-made Li/MgO catalyst particles (b) Methane conversion (c)  $\text{C}_2$  selectivity (d) Total  $\text{C}_2$  hydrocarbon yield of of flame-made Li/MgO particles.
- Figure 2.14.** Comparison of catalytic methane conversion of flame-made Li/MgO catalyst particles, terrace/ball MgO particles with wet-impregnated lithium and commercial MgO with wet-impregnated lithium.

(a) Methane conversion (b) C<sub>2</sub> selectivity (c) Total C<sub>2</sub> hydrocarbon yield of flame-made/ Li/MgO particles.

- Figure 3.1.** Spark discharge system and experimental setup (a) experimental schematic of the particle generation and measurement system. (b) Schematic of the electric circuit in a spark discharge generator.
- Figure 3.2.** Four different types of spark discharge generator. (a) Rod-to-rod type electrode configuration. (b) Pin-to-plate type electrode configuration. (c) Wire-in-hole type electrode configuration. (d) Wire-to-plate electrode configuration.
- Figure 3.3.** TEM images of Ag nanoparticles generated via two different types of spark discharge generator. (a) Nanoparticles generated by rod-to-rod type SDG at the beginning of the experiment. (b) After 12 hours from the beginning. (c) Nanoparticles generated by pin-to-plate type SDG at the beginning of the experiment. (d) After 12 hours from the beginning.
- Figure 3.4.** Size distribution of Ag nanoparticles generated via two different types of spark discharge generator measured every 3 hours. (a) rod-to-rod type SDG (b) pin-to-plate type SDG.
- Figure 3.5.** (a) ~ (e) Morphological changes in the tip of the pin electrode in a pin-to-plate type SDG. Changes in (f) spark discharge voltage and (g) frequency versus time for both SDGs.
- Figure 3.6.** Ag nanoparticles produced via wire-in-hole type SDG. (a) A TEM image of nanoparticles at the beginning. (b) A TEM image of nanoparticles after 12 hours from the beginning. (c) Size distributions of produced nanoparticles measured every 3 hours.
- Figure 3.7.** (a) ~ (e) Morphological changes in the wire electrode in wire-in-hole type SDG. Changes in (f) spark discharge voltage and (g) frequency versus time for WH-SDG.
- Figure 3.8.** Characteristics of particles generated via WH-SDG,

PP-SDG and WP-SDG versus time. (a) Geometric mean diameter. (b) Total number concentration. (c) Geometric standard deviation.

**Figure 3.9.** Size distributions of generated nanoparticles with different gas flow rate. (a) Geometric mean diameter. (b) Total number concentration (c) Geometric standard deviation

**Figure 3.10** Geometric mean diameters and total number concentrations of various metal nanoparticles generated by WH-SDG over 12 hours. (a) Silver (b) Copper (c) Palladium

## List of Tables

**Table 2.1.** Flame conditions for selective generation of terraced and spherical MgO nanoparticles

## Nomenclature

$C_{ext}$	External capacitance
$d_g$	Geometric mean diameter
$E_{spark}$	Energy dissipated during spark discharge
$R$	Charging resistance
$V_{discharge}$	Discharge voltage between electrodes
$V_{electrode}$	Potential applied to electrode
$V_{input}$	Applied setting potential from HV power supply
$\sigma_g$	Geometric standard deviation

# **Chapter 1.**

## **Introduction**

## 1.1 Background of Research

Nanoparticles are expected for having distinguished novel optical, electronical, electrochemical and mechanical properties from bulk materials (Karch et al., 1987; Kruis et al., 1998; Nalwa, 1999; Siegel, 1993; Yang et al., 2010; Yang et al., 2003) Thus nanoparticles have received great attention in various field of modern technology such as electronics, biosensors, optical devices and catalysts (Feldheim and Foss, 2001; Huang et al., 2008; Scheer, 2010).

In order to make practical utilization of nanoparticles, a clean and time-efficient synthesis method is required. Up until now, liquid sol-gel method is widely studied and used for generating nanomaterials. But the requirement to handle the costly and hazardous metal-organic precursors, the multistage character of the processes, the complexity of the apparatus and high energy consumption which lower productivity are disadvantages of liquid-based method for nanomaterial synthesis (Ding et al., 2001; Zolotko et al., 2004). On the other hand, a number of aerosol-based gas phase synthesis methods such as electrical discharge (Schwyn et al., 1988), plasma methods (Rao et al., 1998), laser ablation (Cai et al., 1998) and synthesized in flame (Pratsinis, 1998; Zachariah et al., 1995) are also generally utilized for producing nanoparticles. The gas phase methods for particle synthesis have advantages in terms of obtaining high purity nanomaterials and well disintegrated nanopowders of narrow size

distribution (Zolotko et al., 2004). In addition, aerosol processes generates much less byproducts than liquid-based synthesis methods and collection of particles is much easier from gas than from liquid solution (Pratsinis, 2010).

Among these aerosol-based gas phase synthesis methods, synthesis within flame is widely studied for various functional oxide nanoparticles such as  $\text{TiO}_2$ ,  $\text{ZnO}$ ,  $\text{Al}_2\text{O}_3$ ,  $\text{SnO}_2$  etc (Buesser and Pratsinis, 2012; Grossmann et al., 2015; Lee and Choi, 2002; Mädler et al., 2002; Strobel and Pratsinis, 2007; Thimsen and Biswas, 2007; Tricoli and Pratsinis, 2010). This flame synthesis method has many advantages, continuous and easy to scale-up, small space to place. However, most of flame synthesis including flame spray pyrolysis, employs only liquid solutions as precursors, and they can be possible residual pollutant which would degrade the property of products. Thus, utilizing pure solid metals as precursors of oxide nanoparticles is needed to produce oxide nanoparticles of high purity.

The flame metal combustion method was suggested to use solid metal precursor and showed possibility to produce various types of nanoparticles (Yang et al., 2010). This method also have possibility for controlling the morphology of particles which have different optical properties. With this motivations, the morphology of generated particles can be controlled using the flame metal combustion method. The precise study about controlling the productivity of  $\text{MgO}$  nanoparticles which have different morphology and cathodoluminescence property was carried on to enhance the selectivity of production of the nanoparticles having desired morphology.

Many of aerosol-based gas phase methods for nanoparticle synthesis including flame metal combustion can synthesize nanoparticles of which sizes are the range of 20~100 nm (Zolotko et al., 2004). In order to generating sub-10 nm metal nanoparticles with aerosol method, spark discharge generation is a simple and reliable method (Schwyn et al., 1988). This method can produce metal nanoparticles using diverse materials, and directly applied for the performance enhancement of nanodevices (Messing et al., 2009; Sung et al., 2014). Moreover, it can be a facile method for generating charged aerosols, which can be used as building blocks for controlled fabrication by electrical forces (Kim et al., 2006; Krinke et al., 2001; Lee et al., 2011; You et al., 2010). The rod-to-rod type spark discharge generator (RR-SDG), consists of two rod-shaped metal electrodes confront each other was generally used configuration for this method (Messing et al., 2009; Meuller et al., 2012; Tabrizi et al., 2009). And the pin-to-plate type spark discharge generator (PP-SDG) was introduced which can prevent unintended agglomeration of nanoparticles occurred from the rod-to-rod spark discharge generator (Han et al., 2012). However, the particle size distribution changes over time due to the geometric conditions of pin and plate electrodes are not maintained during long-time operation.

To produce sub-10 nm nanoparticles consistently over time, a new type of spark discharge generator was suggested, called a wire-in-hole type spark discharge generator, which effectively suppressed changes in the

electrode morphology and the gap distance between electrodes for 12 hours. Enhanced stability of this generator will be advantageous for nanofabrication which uses nanoparticles as building blocks.

## 1.2. Objectives for Research

In this research, we pursue developing efficient aerosol-based gas phase synthesis methods for producing nanoparticles having unique properties with size-controllability, possibility to scale-up and maintaining consistency of generated particles. To accomplish this objectives, we extend the capability of flame metal combustion method which can produce nanoparticles with the controllability of particle size and morphology. Next, it is required to address the issue of the consistent generation of sub-10 nm particles without the change of size distribution over long time operation for the utilization of nanoparticles as building blocks for fabricating the nanopattern having desired shapes.

Producing nanoparticles with flame metal combustion method showed possibility for versatility and controllability of morphology and size within the range of 20~100 nm. In this research, the selective generation of oxide nanoparticles was achieved by changing the gas conditions of flame and the size distribution and the proportion of generated MgO nanoparticles and the optical and catalytic properties were investigated.

In order to generate sub-10 nm metal nanoparticles consistently without unintended agglomeration, it is required to integrate the merits of RR-SDGs and PP-SDGs. We designed a newly developed the wire-in-hole type spark discharge generator, and we proved this generator produced sub-10 nm particles consistently over 12 hours by measuring the particle size distributions.

## **Chapter 2.**

# **Flame Metal Combustion Method for Magnesium Oxide Nanoparticle Synthesis of Unique Morphology**

## 2.1. Introduction

MgO is one of the most intensively studied materials because of purely ionic nature and simple cubic rock-salt structure. MgO nanoparticles can be used for the construction of functional nanostructures (Cao et al., 2012; Dhal et al., 2015; Li et al., 2014) and for investigations of surface reactivity on oxides. (Pacchioni et al., 1994; Pacchioni and Maria Ferrari, 1999; Refson et al., 1995) Because equilibrium MgO [100] surfaces are considered chemically inert, the defects (both point defects and coordinately unsaturated ions in extended defects, such as ion vacancies and terrace steps) determine the properties of the MgO surfaces. Five-, four- and three-coordinated sites (i.e., 5C, 4C and 3C), which are characteristics of terraces, terrace steps and kinks, are known to be responsible for the electronic states of MgO nanoparticles (Shluger et al., 1999). One electron vacancies ( $F^+$  centers) and two electron vacancies ( $F^0$  centers) are also strongly related to the morphologies of MgO surfaces (Sterrer et al., 2006).

For synthesizing MgO particles, aerosol-based flame synthesis method is effective method for produce nanoparticles with high yield and controllability. The method is widely used for generating various oxide nanoparticles (Strobel and Pratsinis, 2007; Thimsen and Biswas, 2007; Yang et al., 2010). Moreover, this method can be easily scaled-up for mass production and controlling the size and properties by the flame condition.

## **2.2. Background of Research**

### **2.2.1. Synthesis Method for MgO Nanoparticles**

MgO nanoparticles can be synthesized by decomposing various magnesium salts or magnesium hydroxide ( $\text{Mg}(\text{OH})_2$ , brucite). However, MgO nanoparticles produced by this method have relatively large size with low surface area as well as broad size distributions.(Nagappa and Chandrappa, 2007). Thus, MgO nanoparticles are usually synthesized through sol-gel methods including hydrolysis and condensation (Portillo et al., 1996; Wang et al., 1997). But the sol-gel methods require expensive and hazardous metal-organic compounds as precursors, which is inconvenient and not economical (Ding et al., 2001). In contrast, flame synthesis methods, which use liquids or solutions as precursors have been widely used for producing functional nanoparticles (Buesser and Pratsinis, 2012; Grossmann et al., 2015; Lee and Choi, 2002; Mädler et al., 2002; Strobel and Pratsinis, 2007; Thimsen and Biswas, 2007; Tricoli and Pratsinis, 2010). A conventional metal combustion method using solid metal precursors is also one of combustion methods to synthesize nanoparticles (Patil et al., 2002). But this method is discontinuous and requires external energy sources. Also, the method tends to have unburned or remained precursors in the final products (Yang et al., 2010). Thus, it is required to establish the effective method for generating oxide nanoparticles with high productivity and controllability of particle size and morphology.

### **2.2.2. Flame Metal Combustion Method for Producing Oxide Nanoparticles**

To overcome the problems of this conventional metal combustion, a new flame metal combustion (FMC) method (Yang et al., 2010) was developed to produce pure metal-oxide nanoparticles. This flame metal combustion method has many advantages such as continuous process and high production rate, compact size, short production time, simple and safe ways to carry precursors into flames. Moreover, this method produces much less air pollution because it uses only oxy-hydrogen diffusion flame as the external energy source and metal or inorganic solid powders as precursors (Yang et al., 2010). Various metal oxide nanoparticles can be synthesized by this flame metal combustion method and the properties of nanoparticles could be altered easily by changing several parameters.

One of advantages of FMC method is controlling the morphology of nanoparticles by changing the flame condition. Previously, some have shown changing morphology of MgO nanoparticles using different methods, such as wet etching for several days (Hacquart and Jupille, 2009) and deposition by RF discharge (Muraoka et al., 2009). However, these methods have limitation to generate particles with various morphologies. In contrast, the FMC method produced unique terraced- and spherical-shaped MgO nanoparticles (for brevity we name both “terraced” MgO nanoparticle) in addition to general perfect cubic MgO nanoparticles by changing the flame condition.

Moreover, we revealed the two-band luminescence of terraced and

spherical MgO nanoparticles synthesized by the FMC method and this novel optical characteristic was attributed to the unique divacancy defect states of the MgO particles (Pikhitsa et al., 2015). The FMC method played there an important role of those extreme conditions at which the divacancies were generated in abundance. As we show below, the same extreme conditions in FMC method manifested themselves in non-cubic morphology of MgO nanoparticles. Having in mind possible prospects of using the two-band luminescence in optoelectronics (especially interesting is the 260 nm emission band) and in defect-based lasing which can be tuned by changing particle size and morphology, the growth of the MgO nanoparticles should be carefully investigated.

In this study, size distributions of MgO nanoparticles with different shapes were controlled by varying the flame condition of the FMC to understand the growth process of terraced and spherical MgO nanoparticles in the flame. Controlling morphology and size is very important because the unique optical property of metal oxide nanoparticles is caused not only by their high surface area but also by the high concentration of low-coordinated sites and structural defects on their surface (Mishakov et al., 2002). Through this study, the optimal condition to produce terraced particle was found, and other ways to change morphology have been tried. Additionally, doping MgO nanoparticles with transition metals was conducted to probe the nanoparticle morphology with transition metal ions by following the change in MgO luminescence spectra according to the shape of the MgO nanoparticles.

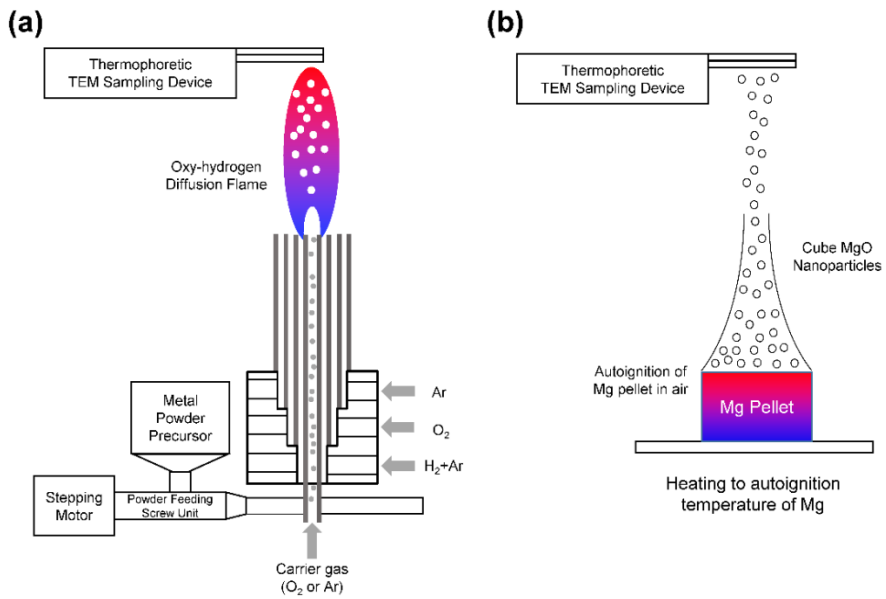
### 2.3. Experimental Details

Figure 2.1 shows schematic for the FMC (left panel) and one conventional combustion method (right panel) for producing MgO nanoparticles, respectively. For the FMC method, solid metal precursors were injected via screw feeding system to a co-axial burner. The co-axial burner for creating the oxy-hydrogen laminar diffusion flame consisted of four stainless-steel tubes. The screw feeding system of solid precursors and the production rate of nanoparticles are described in detail elsewhere (Yang et al., 2010). Micrometer-sized Mg metal powders (Alfa-aesar, 99.6% purity) were used as solid metal precursors to synthesize MgO nanoparticles through the FMC method. The injection mass rate of solid precursors was controlled by the revolution speed of the stepping motor connected to the screw feeding system. At the end of the mechanical feeding system, solid precursor powders were carried by oxygen (O<sub>2</sub>) or argon (Ar) (99.999% purity) into the oxy-hydrogen flame through the center nozzle of the coaxial burner. Hydrogen (H<sub>2</sub>) and O<sub>2</sub> (99.999% purity), as fuel and oxidizer, respectively, were fed through the following concentric annuli. Hydrogen was diluted with Ar to maintain the residence time in flame identically for all experiments. Ar shield gas was injected into the outermost concentric ring of the co-axial burner. The flow rate of oxidizer, carrier gas and shield gas were fixed as 2, 1.5 and 3 lpm for all experiments, respectively. The images of generated flame for producing particles are shown in Figure 2.2. As shown in Fig 2.2, the

flame size which determines the growth region of particles could be controlled by the flowrate of the gases injected to the flame reactor. The flame conditions of all experiments are summarized in Table 1. The flame temperature was measured using a B-type thermocouple with respect to the height of the flame. Generated MgO nanoparticles were sampled on the TEM grid using a localized thermophoretic sampling devices (Cho and Choi, 2000; Lee et al., 2008), and analyzed using normal (TEM, Carl Zeiss, Libra 120) and high-resolution transmission electron microscopes (HR-TEM, JEOL ARM 200F) to investigate the morphology and size distribution of MgO nanoparticles. Nanoparticles were also collected using a Si wafer to investigate the crystallinity. The structural characteristics of MgO nanoparticles were determined by X-ray diffraction (XRD, Mac Science, M18XHF-SRA). For investigating optical luminescence, cathodoluminescence measurement was carried out (CL, Gatan, MonoCL3) at room temperature.

In order to synthesize Li-doped MgO catalyst nanoparticles, Mg metal powders (99.8%, Alfa-aesar) were mixed with 5 wt% of lithium carbonate powders (Li, 99.98 %, Alfa-aesar). The mixture precursor was injected to the oxy-hydrogen diffusion burner via the screw powder feeder. The flame condition for reaction was the long flame condition ( $H_2$  7 +Ar 1 lpm,  $O_2$  2 lpm,  $O_2$  1.5 lpm as carrier gas, Ar 4 lpm as shield gas). The control sample was prepared by a wet-impregnation method with the Li and a commercial MgO (99.995%, Sigma-Aldrich). The produced Li/MgO powder was sintered at

800°C for 4 hours in ambient air. The catalytic activity was measured in a quartz reactor at atmospheric pressure with heating up the reaction gases to 700°C (Lee et al., 2015). The total flow rate of reaction gases was 50 sccm, and the ratio of the gases were  $\text{CH}_4:\text{O}_2:\text{Ar} = 4:1:5$ . The gas products after the catalytic reaction were analyzed by a gas chromatography (Agilent GC 6890N).



**Figure 2.1. (a) Schematic of flame metal combustion method (b) conventional metal combustion method**

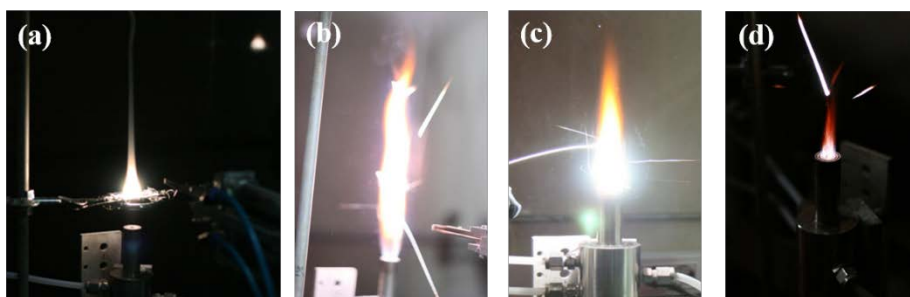


**Figure 2.2. Image of flame for synthesizing MgO nanoparticles. (a) Conventional Metal Combustion Method; self-ignition in ambient air. (b) Long flame;  $H_2 + Ar$  7+1 lpm,  $O_2$  2 lpm,  $O_2$  gas 1.5 lpm as carrier gas (c) Middle-sized flame;  $H_2 + Ar$  4 lpm,  $O_2$  2 lpm,  $O_2$  gas 1.5 lpm as carrier gas (d) Short flame with dilution gas;  $H_2 + Ar$  2+6 lpm,  $O_2$  2 lpm,  $O_2$  gas 1.5 lpm as carrier gas.**

Flame condition	Long flame	Short flame with dilution gas	Long flame with Ar carrier gas
H <sub>2</sub> / Dilution gas(Ar) (lpm)	7/1	2/6	7/1
O <sub>2</sub> (lpm)	2	2	2
Carrier gas (O <sub>2</sub> or Ar) (lpm)	1.5 (O <sub>2</sub> )	1.5 (O <sub>2</sub> )	1.5 (Ar)
Shield gas (Ar) (lpm)	3	3	3

**Table 2.1. Flame conditions for selective generation of terraced and spherical MgO nanoparticles (lpm: liter per minute)**

## **2.4. Results and Discussion**

### **2.4.1. Synthesis of Unique Terraced and Spherical MgO Nanoparticles**

Figures 2.3(a) and 2.3(b) shows the difference of morphology of the particles synthesized using two different methods. The MgO nanoparticles produced via the FMC method show unusual terraced and spherical shapes, otherwise, nanoparticles synthesized with the conventional combustion method were common cubic-shaped nanoparticles. From the X-ray diffraction analysis in Fig. 2.3(c), the crystal structures of both types of nanoparticles were identified as pure MgO. The notable difference between two differently shaped MgO nanoparticles is seen from the cathodoluminescence (CL) spectra given in Fig. 2.3(d), where terrace or spherical nanoparticles show the ultraviolet luminescence band at 260 nm, which did not appear in cubic MgO nanoparticles.

The origin of this luminescence was a divacancy center in MgO which was formed during mode II (depicted in Figure 2.11) combustion process, and this luminescence phenomenon was investigated in detail in Section 2.4.4.

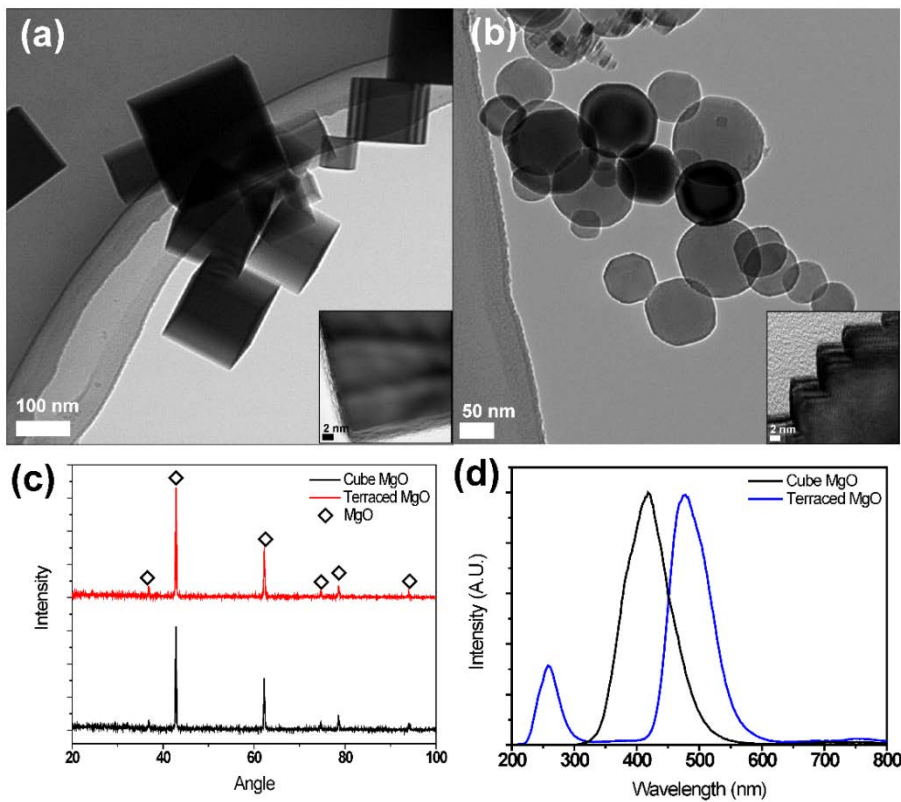


**Figure 2.3. (a) TEM image of cube MgO nanoparticles (b) TEM image of Terraced MgO nanoparticles (c) X-ray diffraction of MgO nanoparticles. (d) Cathodoluminescence spectra of cube and terraced MgO**

## 2.4.2. Particle Size Distribution of MgO Nanoparticles Generated in Two Different Conditions

Figure 2.4 shows the TEM images of the MgO nanoparticles generated at the long flame condition (see Table 1) with respect to the axial flame height above burner where the nanoparticles were captured. The gas composition of the long flame condition was H<sub>2</sub> 7 lpm diluted with Ar 1 lpm (H<sub>2</sub>/Ar: 7/1) and the flow rate of other gases are described in Table 1. The particle size distribution (PSD) and the portion of the terraced nanoparticles were measured with the TEM images. From Figure 2.5(a), 84% of particles were terraced nanoparticles at 10 mm from the bottom of the flame, and it showed the lowest portion of terraced nanoparticles (36%) at 250 mm. The nanoparticle size depicted in Figure 2.5(b) showed that the growth of terraced nanoparticles occurred at lower height of the flame, implicating a very fast initial growth. On the other hand, cubic nanoparticles mostly grew in the higher flame region, which could come from the relatively slower growth process of the cubic MgO nanoparticles than the terraced particles. When the particle grows with diffusion-limited surface growth mechanism, particle diameter  $d_g$  follows the equation (Beaucage et al., 2004):

$$d_g = [DV_m(C_b - C_d)t]^{1/2} + d^* \quad (1)$$

From the equation,  $d_g$  is proportional to the square root of residence time in flame. Using the velocity of gas in flame  $v_g = 1$  m/s, the term for time  $t$  can be changed to  $t = x/v_g$ , which  $x$  is the distance from the flame burner height.

Then the equation (1) can be rewritten as (Chae, Pikhitsa, et al., 2015):

$$d_g = (D^*)^{1/2} t^{1/2} = (D^*/\nu)^{1/2} x^{1/2} \quad (2)$$

From the curve of terrace/ball nanoparticles in figure 2.5, the value of apparent diffusion coefficient  $D^* = DV_m(C_b - C_d)$  was  $82.4 \text{ nm}^2/\text{ms}$ , and the value of diffusion coefficient  $D$  can be estimated to  $0.926 \text{ cm}^2/\text{sec}$  at  $1900 \text{ K}$  (Beaucage et al., 2004).

To understand the experimental data presented in Figs. 2.4-2.10 one has to be governed by the principal difference between the two existing modes of growth of cubic and spherical (terraced) nanoparticles, say, mode I and mode II, respectively. This difference lies in explosive-like (surface defect-induced fast) growth of spherical seeds (depicted in Figure 2.7) and then, of spherical (terraced) nanoparticles in the high-temperature zone (mode II); in Figure 2.5 (a) this zone is restricted within 0-50 mm heights (dashed in Figure 2.5(a), 2.5(b), see figure caption). We will discuss the mechanism of the fast growth in detail below, while discussing Figure 2.10; here we only mention that cubic nanoparticles are produced under the neat MgO molecule condensation (mode I) at lower temperatures and thus the growth is much slower than in mode II. The competition between those two modes is completely responsible for the dependences shown in Figs. 2.4-2.10.

As an example of how our concept of two mode growth works, let us consider the data in Figure 2.7. The fast mode II growth of spherical nanoparticles nearly stops after the high-temperature dashed zone (below 50

mm, Figure 2.5 (a), (b)) and only the slow growth of already formed terraced nanoparticles happens (see Figure 2.10) above 50 mm (Figure 2.5 (b)). On contrary, the higher and cooler part (above 50-100 mm height) of the flame promotes mode I and massive inception and further growth of cubic nanoparticles which is understandable from the proportion of Figure 2.5(a). The depression seen in Figure 2.5(b) for average size of cubic nanoparticles can be explained by a marginal low-temperature growth (mode I) possible even below 50 mm but only at the flame border in the horizontal direction of the high temperature zone where the flame temperature is lowered enough for mode I. Higher in flame, the cubic nanoparticles that grew before in this marginal zone below 50 mm will be diluted among numerous newly grown cubic nanoparticles of less size, so that the average size of the cubic nanoparticles drops down and is seen as a depression in Figure 2.5(b). Above the height of 50-100 mm the mode I growth leads to gradually increasing size of cubic nanoparticles.

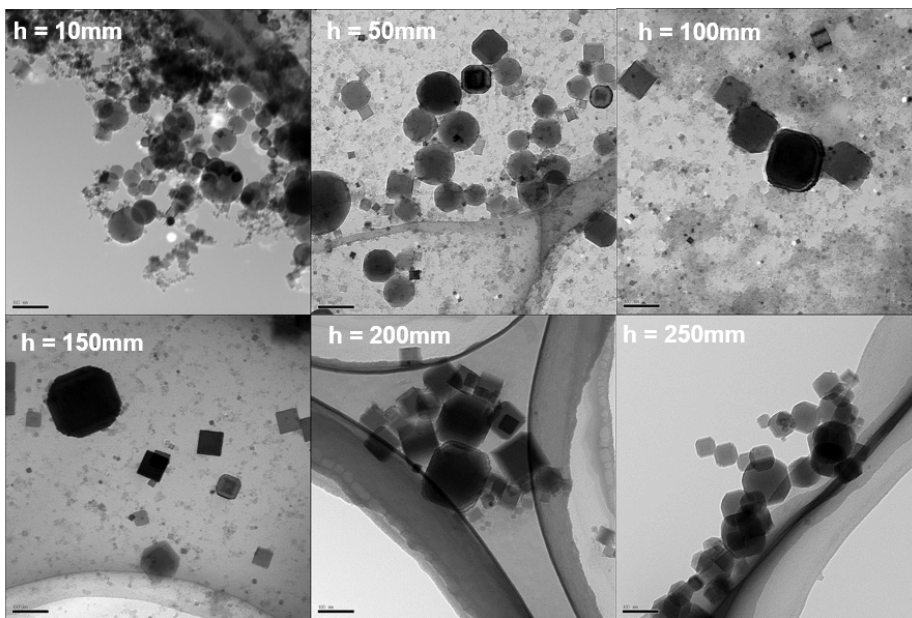


**Figure 2.4. TEM images of nanoparticles synthesized from long flame condition ( $\text{H}_2 + \text{Ar}$  7+1 lpm,  $\text{O}_2$  2 lpm, carrier gas  $\text{O}_2$  1.5 lpm). Particles are collected at 10, 50, 100, 150, 200, 250 mm from the burner.**

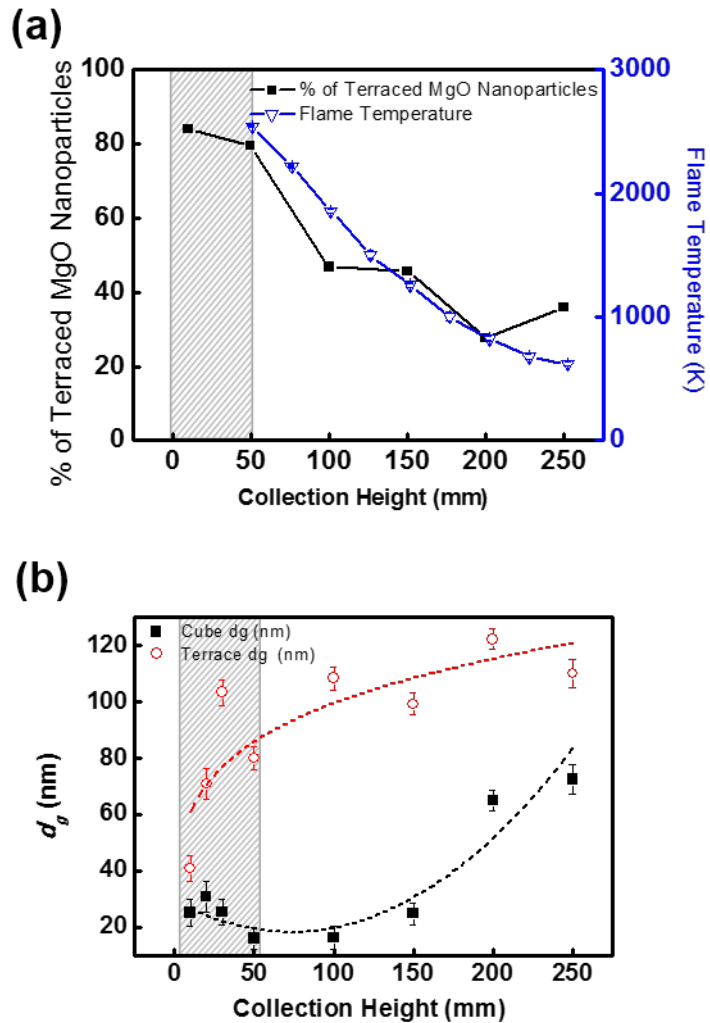
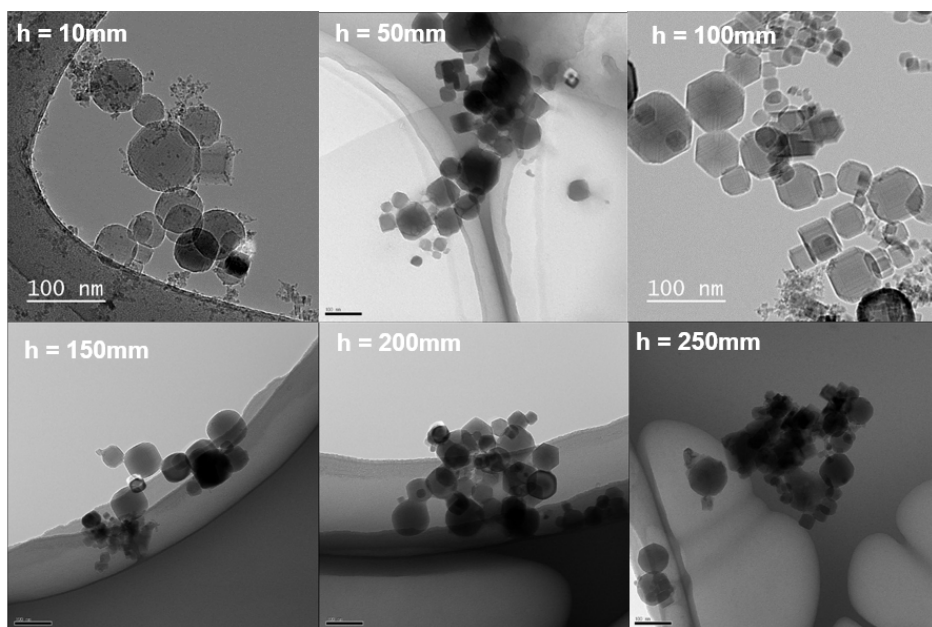


Figure 2.5. (a) Temperature distribution with the height in flame  $H_2/Ar = 7/1$  lpm along with the ratio of the number of terraced nanoparticles over cubic ones. (b) Diameters of terraced and cubic nanoparticles vs the height. The dashed zones in both plates mark the fast growth region of spherical nanoparticles. Dotted lines are guides for eye.

An additional experiment with the short flame, which results are given in Figure 2.6 and 2.7 was conducted to find optimal condition for producing higher portion of terraced MgO nanoparticles. The gas flow rate of H<sub>2</sub>/Ar was 2/6 lpm and other conditions had the same gas flow rate as for the long flame condition. In this condition, most of the generated particles were terrace/spherical-shaped. From Figure 2.7 (a), 94% of the generated particles were terrace and spherical-shaped from the sample collected at 10 mm from the bottom of the flame, while the sample collected at 250 mm showed 83% of terraced MgO nanoparticles. Nanoparticles generated from short flame condition contained much higher portion of non-cubic particles than long flame condition. The geometric mean diameter of nanoparticles grew fast like for long flame condition but the growth zone in flame which had sufficiently high temperature was short, thus the final nanoparticle diameter was smaller than that generated in long flame condition.

This result supported the viability of our two-mode concept. The abundance of terraced nanoparticles, seen in Figure 2.7(a) stemmed from the mode II growth in the dashed zone. However, the temperature was somewhat lower (1500 K vs 2500 K in Figure 2.5(a)), the growth rate on mode II, being a thermally activated process, was lower as well. Also the final size of terraced nanoparticles in Figure 2.7(b) is only 60 nm vs 120 nm in Figure 2.5(b). Additionally, larger O<sub>2</sub> concentration in 2/6 flame provides more effective surface defect growth on spherical nanoparticles via mode II (see also Figure 2.9(a) below). Note, by the constant irradiation of the burning

zone of an Mg pellet in oxygen with a CW CO<sub>2</sub> laser we found that exclusively spherical and terraced nanoparticles can be created.(Stankic et al., 2011) On the other hand, the growth of cubic nanoparticles on mode I proceeded similar to Figure 2.5(b). Yet, the number of those nanoparticles was much less because of much lower flame temperature above 50 mm height (Figure 2.7(b)), which reduces the number of incipient cubic nanoparticles. Therefrom the prevailing number of terraced nanoparticles over the cubic ones originates (Figure 2.7(a)).



**Figure 2.6. TEM images of nanoparticles synthesized from short flame condition ( $\text{H}_2 + \text{Ar}$  2+6 lpm,  $\text{O}_2$  2 lpm, carrier gas  $\text{O}_2$  1.5 lpm). Particles are collected at 10, 50, 100, 150, 200, 250 mm from the burner.**

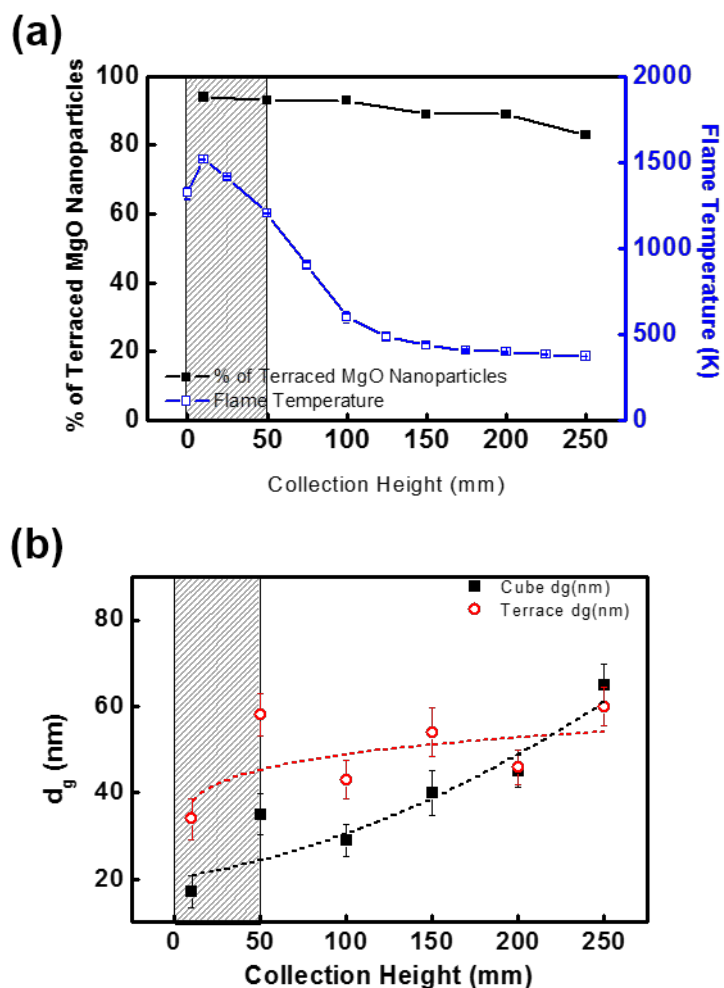


Figure 2.7. (a) Temperature distribution with the height in “short” flame ( $H_2/Ar = 2/6$  lpm ) along with the ratio of the number of terraced nanoparticles over cubic ones. (b) Diameters of terraced and cubic nanoparticles vs the height in flame. The dashed zones in both plates mark the fast growth region of spherical nanoparticles.

Changing the flow rate of fuel (hydrogen) and Ar dilution gas was carried out to inspect how the percentage of terrace-shaped MgO nanoparticles would be altered according to the gas composition and the flame size. From Figure 2.9, the percentage of terraced nanoparticles collected at 250 mm height increased as hydrogen in fuel gas ( $H_2+Ar$ ) decreased, and the average diameter of nanoparticles was smaller than the one at a higher proportion of hydrogen in fuel.

The flame conditions at  $H_2/Ar = 7/1$  and  $2/6$  in Table 2.1, considered above, are two extremes of the hydrogen flow rate changing from 7 to 2. The sizes and ratio of generated MgO nanoparticles are shown in Figure 2.9. The size of the terrace-shaped nanoparticles increased with the flow rate, while the size of the cubic nanoparticles was almost constant. It is in accord with the influence of the flame temperature on the growth rate on mode I. The ratio (Figure 2.9(a)) of terraced to cubic nanoparticles also followed the above described temperature-governed scenario.

Finally, we replaced carrier gas,  $O_2$  with Ar in flame  $7/1$  as described in Table 2.1 to see the effect of carrier gas. In other words, the  $O_2$  dependence of the terraced MgO nanoparticles during mode II at the long flame condition. Figure 2.10(a) shows cubic nanoparticles were mostly produced with the Ar carrier gas, although little amount of terraced nanoparticles was generated during mode II at 50 mm height (Figure 2.10(b)). However, as we discussed below, for larger nanoparticles at higher heights of the long flame condition and in the presence of hydroxyl groups the terraced nanoparticles can grow on

mode I as well, although in minor quantity (Figure 2.10(b)).

The large terraced nanoparticles (unlike the terraced nanoparticles grown on mode II seen at 50 mm) may not contain a specific defect center responsible for the two-band CL (260 nm and 490 nm) (Pikhitsa et al., 2015), which is evident in Figure 2.10(c) for the nanoparticles produced with O<sub>2</sub> carrier gas. The one-band CL (420 nm) and two-band CL are the strong indicators of two different growth modes.

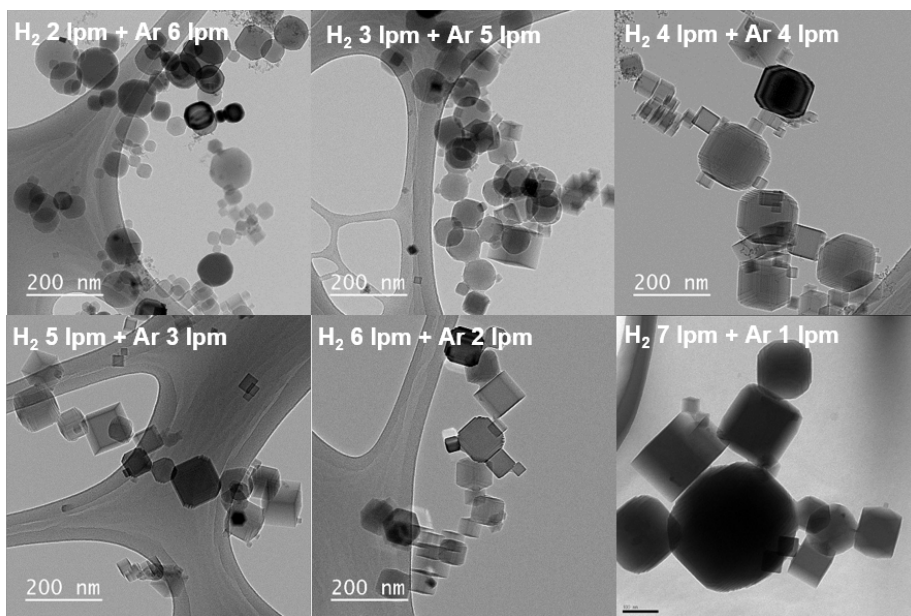


**Figure 2.8. TEM images of nanoparticles generated varying the flowrate of fuel and dilution gas. Particles are collected at 250 mm from the burner.**

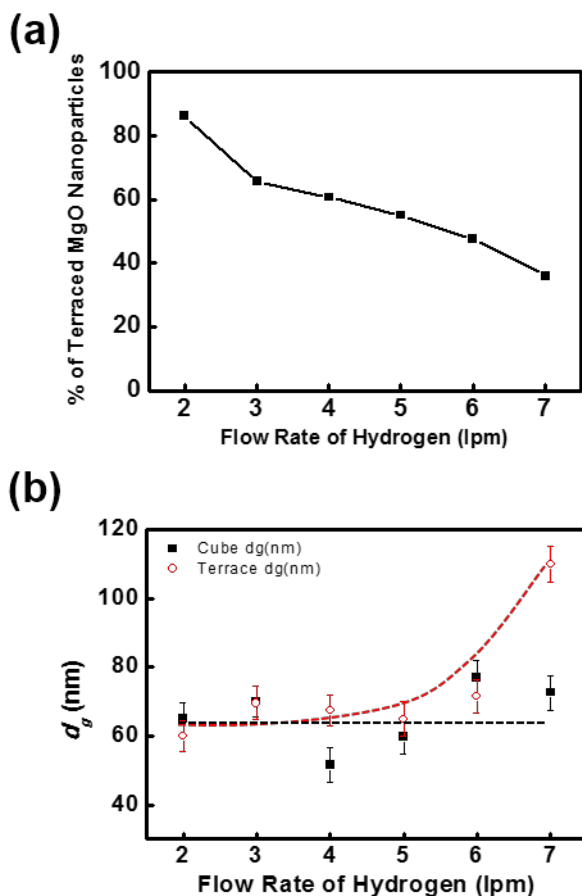


**Figure 2.9. (a) The ratio of terraced over cubic nanoparticles vs hydrogen flow rate. (b) Sizes of nanoparticles at 250 mm vs the flow rate of hydrogen for terraced and cubic nanoparticles. The dotted lines are guides for eye.**

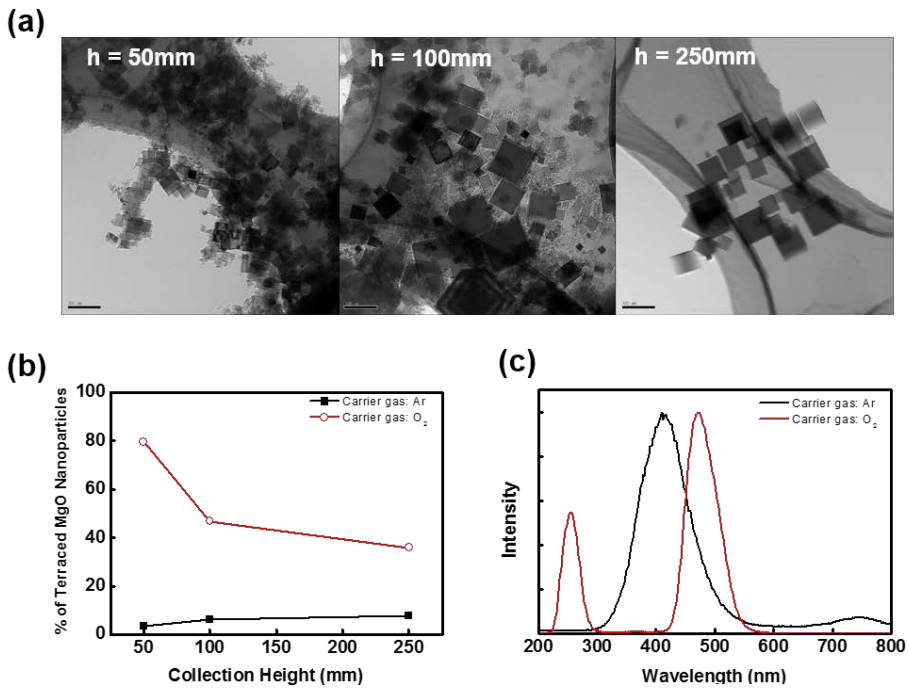


**Figure 2.10. (a) TEM images of nanoparticles collected at different heights for argon carrier gas. (b) Proportion of terraced nanoparticles vs the height in flame for oxygen and argon carrier gas. (c) The CL spectra for nanoparticles produced with oxygen or argon carrier gases show very different light emission bands.**

### 2.4.3. Growth Mechanism of Terraced/spherical and cubic MgO nanoparticles

From the HR-TEM images of Figure 2.11(a), one reveals a neat scaling law for terraced nanoparticles: the average size of the terrace steps on each nanoparticle is proportional to the size of the nanoparticle. This behavior excludes water vapor or hydrogen etching as being responsible for the large steps because etching always leads to tiny 1 nm steps.

To explain the linear dependence we notice that the large non-cubic nanoparticles are strictly divided into perfectly spherical and terraced ones. We claim that at the very initial stage of growth in flame both type nanoparticles are indistinguishably spherical and divide into two types only at the later stage of the growth. The possible mechanism of the generation and growth of the spherical MgO particles will be precisely described in this chapter.

Since long ago it has been known that there are two possible reactions that lead to solid MgO nanoparticles from Mg burning (Newman and Payne, 1987) : (I)  $\text{MgO}_{(g)} \rightarrow \text{MgO}_{(s)}$ , with enthalpy  $-566.3 \text{ kJ/ mol}$  at  $1900 \text{ K}$ ; (II)  $(\text{MgO})_n + \text{Mg}_{(g)} + 1/2 \text{ O}_2 \rightarrow (\text{MgO})_{n+1}$ , with larger enthalpy  $-729.3 \text{ kJ/ mol}$  at  $1900 \text{ K}$  . It is believed that only the first process, thus only the condensation from supersaturated MgO gas into MgO solid, takes place. (Altman et al., 2004; Newman and Payne, 1987; Stankic et al., 2011) Growth governed only by condensation of MgO molecules (mode I) leads to incipient cubes

and then to the larger cubes. However, computer simulations (Geneste et al., 2007) predict that O<sub>2</sub> molecules can be active and participate in nanoparticle surface growth (mode II) after O<sub>2</sub> molecules split over defects on the surface of growing MgO nanoparticles thus stimulating the most surface-defective (because the sphere is the most incompatible with the cubic lattice) incipient spherical shapes. The competition between the two growth mechanisms might take place with the intensification of the burning process that we performed with the oxyhydrogen flame or infrared laser.

It is known from literature that large terraced particles >200 nm can also grow in humid air by hydroxyl group passivation and thus stabilization of defective surfaces at later growth stage of primary cubes (Hacquart and Jupille, 2009; Moodie and Warble, 1971). On contrary, we observe much smaller than 200 nm terraced nanoparticles and spheres down to 10 nm (Figure 2.11). Such nanoparticles are also found for infrared laser intensified self-burning in air or oxygen where OH groups are not involved at all. This fact points out to mode II as the only reason for spherical and thus highly defective surface of nanoparticles in the environment of intensified self-burning. Then one may conclude that when spherical nanoparticles, initially grown on mode II, are transported by convection to the environment, favorable for MgO molecule condensation on mode I, and then continue their growth there, the incipient and then primary spheres start “healing” the surface defects and evolving into cubic nanoparticles through *terrace* step phase.

It is easy to see that there is no other intermediate *evolutionary* shape between the initial sphere and the final cube except the *terraced* nanoparticle that preserves the cubic MgO lattice for the single-crystalline nanoparticle. However, in the case when growth mode II persists through the whole nanoparticle growth then large perfect spheres can be grown from incipient and primary ones as we observe (Figure 2.11).

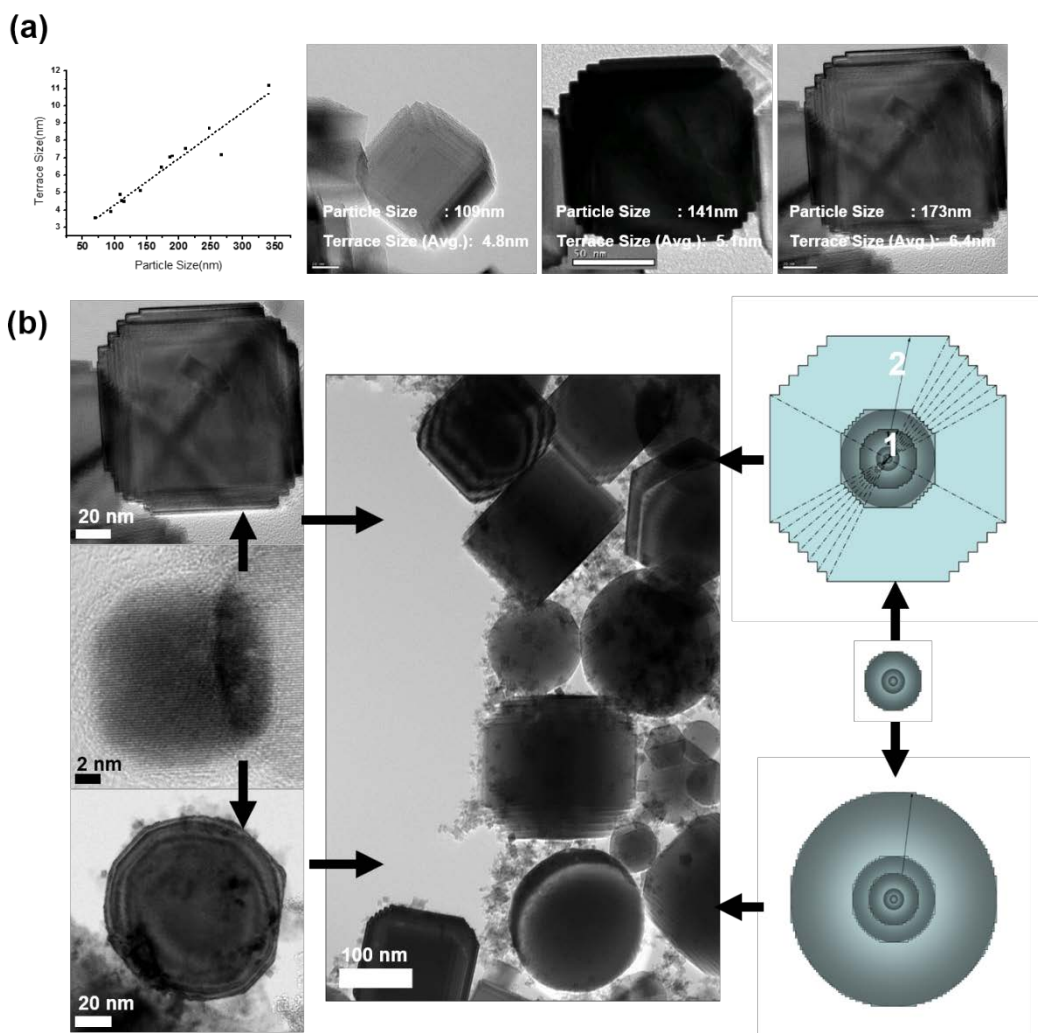


**Figure 2.11. (a) TEM images of terraced nanoparticles reveal the proportionality law between the sizes of terraced nanoparticles vs the height of terrace steps. (b) The illustration of the growth mechanism that leads either to perfect spherical nanoparticles (mode II growth) or to terraced nanoparticles (when mode I growth follows mode II growth).**

It is known from literature that large terraced particles  $>200$  nm can also grow in humid air by hydroxyl group passivation and thus stabilization of defective surfaces at later growth stage of primary cubes (Hacquart and Jupille, 2009; Moodie and Warble, 1971). On contrary, we observe much smaller than 200 nm terraced nanoparticles and spheres down to 10 nm (Figure 2.11). Such nanoparticles are also found for infrared laser intensified self-burning in air or oxygen where OH groups are not involved at all. This fact points out to mode II as the only reason for spherical and thus highly defective surface of nanoparticles in the environment of intensified self-burning. Then one may conclude that when spherical nanoparticles, initially grown on mode II, are transported by convection to the environment, favorable for MgO molecule condensation on mode I, and then continue their growth there, the incipient and then primary spheres start “healing” the surface defects and evolving into cubic nanoparticles through *terrace* step phase. It is easy to see that there is no other intermediate *evolutionary* shape between the initial sphere and the final cube except the *terraced* nanoparticle that preserves the cubic MgO lattice for the single-crystalline nanoparticle. However, in the case when growth mode II persists through the whole nanoparticle growth then large perfect spheres can be grown from incipient and primary ones as we observe (Figure 2.11).

We now consider the evolution of the terrace step size. After a violent defect-induced surface growth in pure oxygen that leads to spherical precursor particles, the nanoparticle enters the flame region where

absorption-desorption processes (Mullins, 1957) dominate. Because a spherical precursor nanoparticle less than 5 nm is a nanoparticle with a perfect cubic MgO lattice according to HR-TEM, it may have as few as, say, 10 elementary steps of the MgO lattice constant of 0.21 nm on each “side”. These elementary steps (or grooves) act as incipient terrace steps and may start developing into the terrace steps seen in Figure 2.11. The number of steps may be conserved or reduced while the diffusion growth occurs.

Figure 2.11(b) gives the detail illustration of the mechanism for generation of terraced MgO nanoparticles either by the Mg self-burning within the oxy-hydrogen flame (HR-TEM images are given for this case) or with the infrared laser assisted Mg self-burning in air. The middle part of left (HR-TEM) and right (sketch) panels show a germ spherical nanoparticle created by fast surface defect-induced growth mechanism (mode II). The steps are of the size of the lattice distance. Top left and right panels (indicated with arrows) show the spherical nanoparticle evolution into a terraced nanoparticle in flame when adsorption-desorption of MgO molecules dominates. Then, as more and more MgO molecules are adsorbed without creating additional steps, the step size increases proportionally to the particle size and the number of steps nearly conserves as indicated by dashed lines in the top right panel. Of course, the process of reduction of the number of steps also takes place, as far as the nanoparticle evolves into a cubic shape, but nevertheless the step size still grows on average with the nanoparticle size. The evolution of the nanoparticle starts from the germ

nanoparticle marked 1 and continues to the large one marked 2. Bottom left and right panels show the spherical nanoparticle evolution into a much larger perfectly *spherical* nanoparticle when the germ nanoparticle continues its faster growth in O<sub>2</sub> environment where the surface defect induced growth (mode II) dominates. The middle panel is the TEM image of the resulting MgO smoke where both large spheres and terraced nanoparticles (up to large cubes) are distinguished.

#### 2.4.4. Cathodoluminescence of undoped and transition metal doped MgO nanoparticles

Without doping, the CL spectra, given in Figure 2.12 contain the 420 nm band (marked F at the left-hand column), the low coordination defect band (marked LC in both columns) and the P two bands (with the 260 nm and 490 nm components both marked P at the left-hand column) which are obviously seen both cathodoluminescence and low-temperature photoluminescence spectra (Pikhitsa et al., 2015).

Doping the terraced nanoparticles with  $\text{Cr}^{3+}$  ions generates an additional and well defined broad band at 730 nm seen in Figure 2.12. This band is complex and contains R and N zero-phonon lines that can be distinguished in CL spectrum given in Figure 2.12, together with the broad phonon replicas. Similar spectra were obtained for doped MgO thin films (Stavale et al., 2012). No specific features for  $\text{Cr}^{3+}$  doping peculiar to terraced nanoparticles are found. As we explain below, such peculiar features could come from the reduced crystal field felt by ions near LC defects. However, being a  $3d^3$  ion, a trivalent chromium should experience a  ${}^4\text{E}({}^2\text{G}) - {}^4\text{A}_2({}^4\text{F})$  optical transition that practically does not depend on the crystal field strength.

On contrary, doping terraced nanoparticles with  $\text{Mn}^{2+}$  may produce several  $\text{Mn}^{2+}$  bands, two of which are seen in Figure 2.12 (the one, often of somewhat lower intensity, at 610 nm and the one at 750 nm, both marked

Mn<sup>2+</sup>). The 750 nm band always appears in Mn<sup>2+</sup> doped MgO nanoparticles and comes from Mn<sup>2+</sup> ion in perfect environment of the octahedral sites in cubic crystal field of MgO lattice. The band is bulk in nature (though it is excited easily only in nanoparticles because the bulk optical transitions are weak) and has CL unresolved complex structure with a low-temperature zero phonon line at 735 nm (and the phonon replica band peaking at 750 nm at room temperature) that was discovered from photoluminescence in nanocubes of MgO (Altman et al., 2003). The band at 610 nm was not seen in previous work (Altman et al., 2003) because only the MgO nanocubes studied, being large and nearly perfect, had too few LC defects. On the other hand, terraced nanoparticles or tiny cubes have high concentration of LC defects as is seen from the presence of the LC bands in Figure 2.12. This presence is the necessary condition for the 610 nm Mn<sup>2+</sup> band. One can see that only if there is an LC band than the 610 nm may be seen. In other words, *when the 610 nm band exists, then LC band is always present*. Sometimes (as in the lowest panel in the right column) the 610 nm band is even more intense than the 750 nm band. At the left-hand column the 610 is always less than 750 nm, which can be explained by the abundance of perfectly spherical nanoparticles that lack terraces as *isolated* LC defects that have a distinguished electronic state. Spherical nanoparticles have virtually all the surface sites being defective; therefore the LC band is smeared and cannot be observed. For nanoparticles that show two-band UV-Vis CL (marked as P-bands in Figure 2.12) this is usually the case.

The state, responsible for the 610 nm  $\text{Mn}^{2+}$  band, comes from the lowering of the crystal field that splits the electron states of  $\text{Mn}^{2+}$  ion near LC defects. Basically, both bands come from the same  ${}^4\text{T}_1({}^4\text{G}) - {}^6\text{A}_1({}^6\text{S})$  optical transition, (Altman et al., 2003) however the reduced crystal field at LC defect sites shifts the emission of  $\text{Mn}^{2+}$  ion near an LC defect to shorter wavelengths. Thus, terraced MgO nanoparticles may be interesting for tuning the optical properties of doped MgO material by changing the crystal field intensity with terraces.

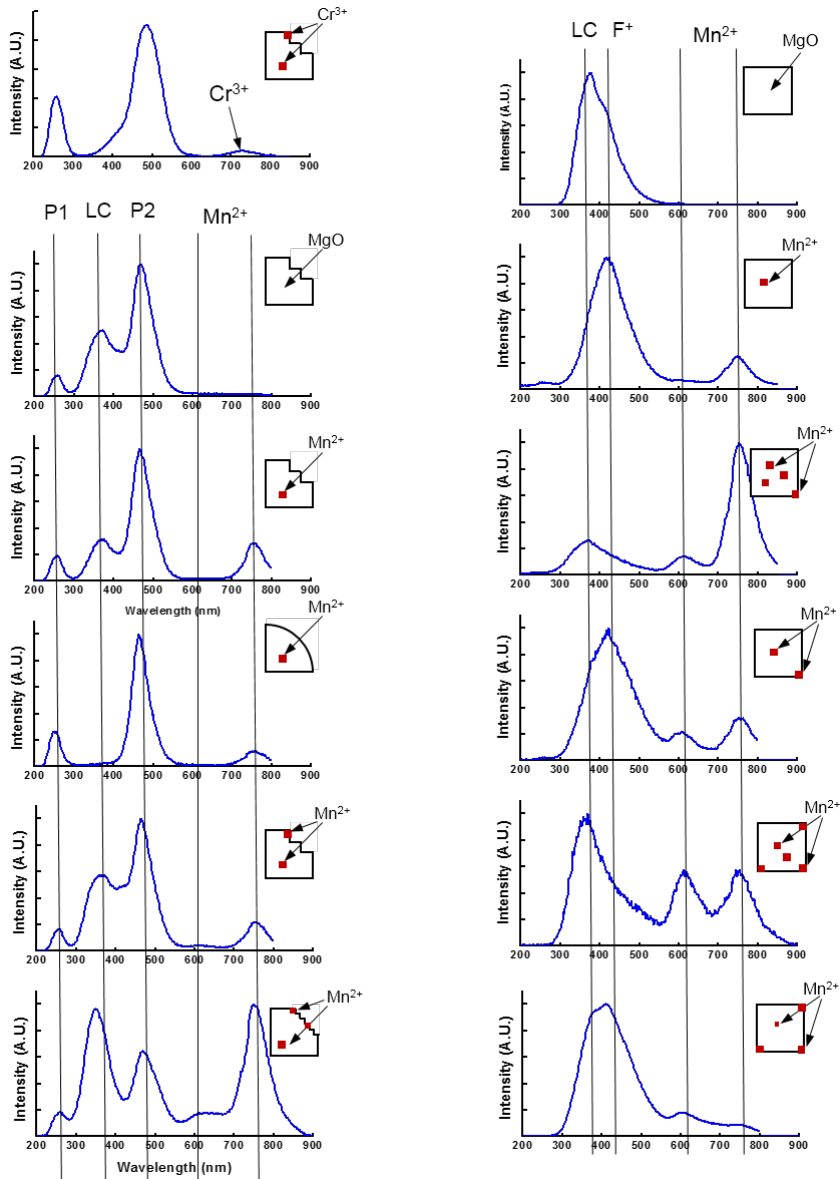


**Figure 2.12.** All possible cases of CL bands from cubic and terraced nanoparticles, including the dopant bands. Doping with  $\text{Cr}^{3+}$  ion produces characteristic 730 nm band with R and N zero phonon lines distinguished above 700 nm even at room temperature. Doping with  $\text{Mn}^{2+}$  may produce 610 nm and 750 nm bands.



#### **2.4.5. Oxidative Conversion of Methane Reaction of Flame-made MgO catalyst nanoparticles**

Methane, one of the main components of the natural gas has been highlighted as a carbon source for the chemical industry (Arndt et al., 2011; Lunsford, 1995). The MgO nanoparticles are considered as one of the most sufficient and stable supporters for the oxidative catalytic conversion of methane (OCM) reaction. With lithium as catalyst, Lithium-doped MgO (Li/MgO) composites have been considered as effective catalysts with a high conversion rate of methane and a good selectivity to the targeted higher hydrocarbons. Therefore, it is one of the most promising catalysts for the OCM reactions (Aritani et al., 2000; Arndt et al., 2011; Raouf et al., 2013).

So far, the wet-impregnation method has been widely studied and used for producing the Li/MgO catalyst particles. However, the wet-impregnation method requires long time to produce the catalyst particles because the method involves several time-consuming steps, such as stirring, mixing and drying solvents overnight (Aritani et al., 2000; Raouf et al., 2013).

Using the FMC method, the reaction for producing Li/MgO particles was completed only in a few seconds during the residence time of the particles in the  $H_2/O_2$  flame. Hence, the gas-phase FMC method reduced drastically the production time for the Li/MgO catalyst particles.

The conversion rate of methane gas of flame-made Li/MgO was 12.7 %

and total C<sub>2</sub> hydrocarbon(including C<sub>2</sub>H<sub>2</sub>, C<sub>2</sub>H<sub>4</sub>, C<sub>2</sub>H<sub>6</sub>) yield of 7.58 % at CH<sub>4</sub>:O<sub>2</sub> = 9:1 condition (Figure 2.13). This was rather low conversion efficiency, however, the reaction rate was increased by changing gas condition to CH<sub>4</sub>:O<sub>2</sub> = 4:1 without raising the rate of conversion to CO<sub>2</sub> and CO gas. As shown in Figure 2.14, the conversion rate of the methane into the flame-made Li/MgO was 22.5 %, and the C<sub>2</sub> selectivity was 55.6%. Hence, the total C<sub>2</sub> hydrocarbon yield was 12.5 % (Fig. 9 (c)). This yield was much higher than that (4.28%) of the control sample impregnation.

Although the yields reported by others were similar or higher in some degree (Aritani et al., 2000; Arndt et al., 2011; Raouf et al., 2013), synthesizing catalysts via the gas-phase FMC method has advantages of the short time to obtain catalyst particles without pollutants such as residues and byproducts. In addition, the FMC method can be easily scaled up by controlling the injection of precursors and installing multiply arranged flame burners, thus increasing the production rate of the catalyst particles.

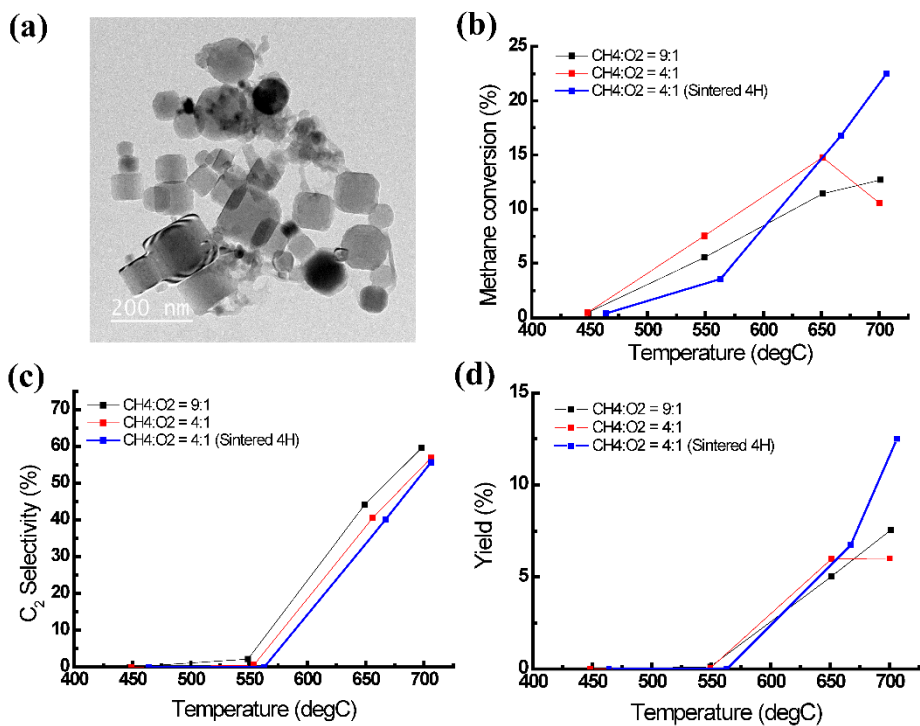


**Figure 2.13. (a) TEM image of flame-made Li/MgO catalyst particles (b) Methane conversion (c) C<sub>2</sub> selectivity (d) Total C<sub>2</sub> hydrocarbon yield of flame-made Li/MgO particles.**

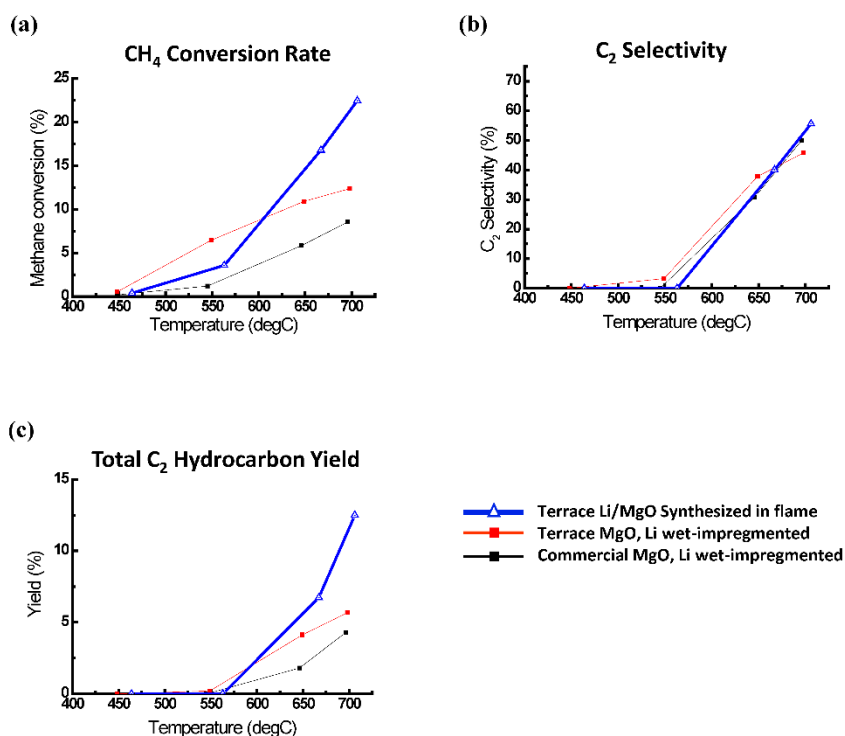


**Figure 2.14. Comparison of catalytic methane conversion of flame-made Li/MgO catalyst particles, terrace/ball MgO particles with wet-impregnated lithium and commercial MgO with wet-impregnated lithium. (a) Methane conversion (b) C<sub>2</sub> selectivity (c) Total C<sub>2</sub> hydrocarbon yield of flame-made/ Li/MgO particles.**

## 2.5. Conclusions

Terraced and spherical MgO nanoparticles, which have unique optical property of two-band luminescence, were synthesized using the FMC method. The FMC method is convenient for scaling up the production rate of the MgO nanoparticles over 10 g/hr. We investigated the proportion of the terraced and cubic MgO nanoparticles with respect to the size of the flame. Larger proportion and larger quantity of terraced nanoparticles were generated from the short flame condition, which was more abundant of oxygen. The size distribution of the produced MgO nanoparticles was also measured to understand the growth condition of the nanoparticles. From those results, optimal conditions for producing terraced and spherical MgO nanoparticles were found. Furthermore, one was able to control the proportion of the morphologically different MgO nanoparticles using different carrier gases. More terraced MgO nanoparticles were produced with oxygen carrier gas, otherwise the cubic MgO nanoparticles were predominantly generated with argon carrier gas.

From the size distribution and percentage (non-cubic over cubic) of generated MgO nanoparticles, we concluded that there are two different growth mechanisms of non-cubic (terraced and spherical) and cubic MgO nanoparticles. Generation of terraced/spherical MgO nanoparticles could be explained by fast surface defect-induced growth, which was quite different from the growth mechanism of common cubic MgO nanoparticles.

Finally, we investigated the luminescence and the catalytic property of MgO nanoparticles. The cathodoluminescence spectra of MgO nanoparticles could be changed by doping transition metals such as manganese and chromium to probe the concentration of low-coordination defects. Possible tuning of optical properties of MgO nanoparticles by controlling the morphology may be useful for optoelectronics of and lasing using MgO. In order to demonstrate the catalytic property of Li-doped terrace MgO nanoparticles synthesized via one-step flame metal combustion, oxidative coupling reaction of methane molecule was carried out and the catalytic terrace MgO nanoparticles showed higher conversion efficiency than commercial powder. Hence, the flame metal combustion method is highly productive and controllable method for synthesizing oxide nanoparticles that show unique morphology and properties with high selectivity.



## **Chapter 3.**

# **Long-time Consistent Generation of Sub-10 nm Nanoparticles using Wire-in-hole Type Spark Discharge Generator**

### 3.1. Introduction

Spark discharge generation (Schwyn et al., 1988) is a simple, clean and reliable method for generating nanometer-sized particles among diverse gas-phase synthesis techniques. Particles synthesized via a spark discharge generator can be directly used for the enhancement of many electronic and catalytic properties, for example, to increase the efficiency of an organic display device (Sung et al., 2014), to improve the performance of catalysts (Messing et al., 2009), and to generate gold seed particles for nanowire growth (Messing et al., 2009). Furthermore, spark discharge generation can produce nanoparticles using diverse materials having varied properties, such as bimetallic and mixed metallic nanoparticles (Byeon et al., 2008), and nanocomposites (Kala et al., 2013). In addition, this technique has been utilized to generate various types of charged aerosols, which enables the positioning of particles at precise locations on a dielectric surface (Krinke et al., 2001) and the fabrication of nanostructures via controlled electric field (Ha et al., 2014; Jung et al., 2014; Kim et al., 2006; Lee et al., 2011; You et al., 2010). Up to now, the rod-to-rod type spark discharge generator (RR-SDG) has been studied and used widely, however, this configuration inevitably generates unintended agglomerated nanoparticles which make difficult to be used for sophisticated nanofabrication.

In this work, we present a novel wire-in-hole type spark discharge generator (WH-SDG) that is able to generate unagglomerated nanoparticles with a constant size distribution over a long time (Chae, Lee, et al., 2015).

The WH-SDG, which consists of a metal wire and a grounded plate with a hole in which the metal wire is located in the center, effectively suppressed changes in the electrode morphology and the gap distance, which cause the minimal variation of the spark discharge voltage and spark frequency in time.

## **3.2. Background of Research**

### **3.2.1. Spark Discharge Nanoparticle Generator for Stable Nanoparticle Production**

Up until now, rod-to-rod type spark discharge generators (RR-SDG) have been widely studied, and the effects of the process parameters have been well understood (Horvath and Gangl, 2003; Roth et al., 2004; Tabrizi et al., 2009). However, particles generated by RR-SDG are prone to agglomeration at high number concentrations due to post-discharge diffusion charging in bipolar ion clouds (Bau et al., 2010). In an effort to prevent agglomeration of the particles, various methods have been developed such as controlling the flow rate of the carrier gas (Schwyn et al., 1988; Tabrizi et al., 2009) or injecting unipolar charged air ions (Park et al., 2014).

Recently, a pin-to-plate type spark discharge generator (PP-SDG), having asymmetric electrodes consisting of a sharp pin and a plate with a hole, was introduced which generates less agglomerated sub-10 nm nanoparticles with high concentration than the RR-SDG at the same condition (Han et al., 2012). This is attributed to the much faster transport of as-generated particles in the PP-SDG. Furthermore, the PP-SDG can be easily scaled up by employing multiple pin electrodes and corresponding exit holes in the flat-plate ground electrode (Ha et al., 2014). Despite such merits, the PP-SDG generated the particle size and the number concentration which evolve over time due to changes in the electrode geometry, such as gradual increases in the radius of curvature of the pin and in the distance between the pin and the plate as the

pin electrode gets eroded with time. These factors cause changes in spark discharge properties. In this study, to maintain the size distribution of produced nanoparticles over a long time while producing small and unagglomerated nanoparticles with high concentration, we designed a new type of spark discharge generator comprising a metal wire as a positive electrode and a grounded plate with a hole. The wire was placed in the center of an exit hole in the plate. Using this newly designed wire-in-hole type spark discharge generator (WH-SDG), we measured geometric mean diameter (GMD) and particle number concentration for twelve hours at various carrier gas flowrates. In addition, the versatility and controllability of the new design was demonstrated with different kinds of metal such as Cu and Pd.

### 3.3. Experimental Details

The experimental setup consists of a spark discharge generator, an electrostatic precipitator and a scanning mobility particle sizer (SMPS) system with an aerosol neutralizer, which is a commonly used particle measurement setup, as depicted in Figure 3.1(a) (Byeon et al., 2008; Han et al., 2012; Tabrizi et al., 2009). The spark discharge generator was made up of a cylindrical chamber, two electrodes, electrode holders and an inlet and an outlet for carrier gas flow. The inner diameter of the chamber is 40 mm and the length is 30 mm. The electrode holders were precisely machined and assembled at the center of the chamber. Alignment of the geometric condition of electrodes was controlled by putting the ground electrode on the 2-axis micro stage. Silver, copper and palladium (99.99% purity) were used as materials for electrodes. Nitrogen (99.999% purity) was used as the carrier gas, and the flow rate was set at 2 lpm. The size distribution of the generated particles was measured with a differential mobility analyzer (DMA, TSI 3085), a condensation nuclei counter (CNC, TSI 3776) and an Am-241 aerosol neutralizer (Grimm #5.521). The generated particles were transported to the DMA and the CNC, passing through an aerosol neutralizer. The flowrates of sheath and aerosol gas of DMA were set at 15 lpm and 1.5 lpm, respectively. The positively charged nanoparticles were collected on a carbon film-coated copper grid using electrostatic precipitator for 3 minutes, and imaged using high resolution-transmission electron microscope (HR-TEM, JEOL ARM

200F).

The circuit that provides electric power to the spark discharge generator is shown in Figure 3.1(b). Similar circuits have been widely used by other researchers to regulate the spark discharge characteristics (Han et al., 2012; Horvath and Gangl, 2003; Pfeiffer et al., 2014; Schwyn et al., 1988; Tabrizi et al., 2009). It consists of a high voltage power supply, an external capacitor ( $C_{\text{ext}}$ ) and a resistor ( $R_c$ ). Charging time of the external capacitor ( $C_{\text{ext}}$ ) can be chosen by selecting the resistance value of the external resistor ( $R_c$ ) which is depicted in figure 3.1(b). To generate nanoparticles which have desirable particle size distribution, the value of the external capacitor and the external resistor was determined. The high-voltage DC power supply (FuG HCP35-6500) with a maximum voltage of 6.5 kV was connected to one end of the resistor. High voltage power supply output ( $V_{\text{input}}$ ) was set at 6 kV to charge the external capacitor. The external capacitor which is much larger than the intrinsic capacitance between the two electrodes in SDG was connected in parallel to the electrode. Discharge voltage and spark frequency were measured with an oscilloscope (Agilent DSO-X 3014A) and a high voltage probe (Tektronix P6015A).

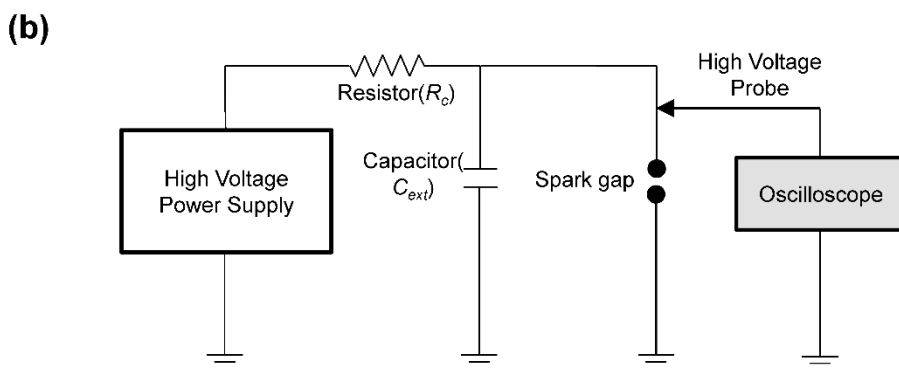
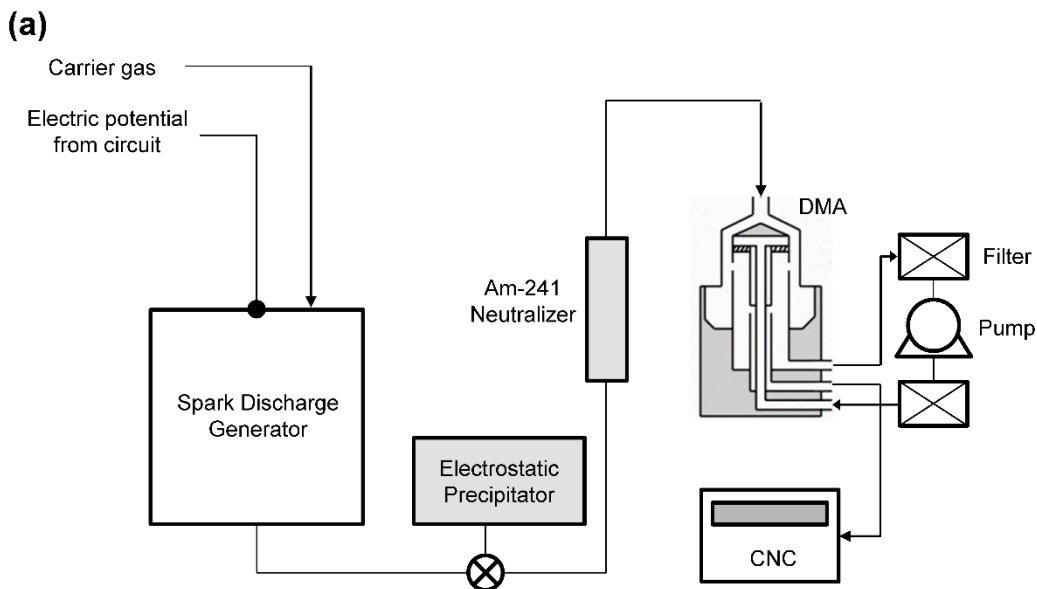


**Figure 3.1. Spark discharge system and experimental setup (a) experimental schematic of the particle generation and measurement system. (b) Schematic of the electric circuit in a spark discharge generator.**

We investigated the characteristics of four different electrode configurations as depicted in Figure 3.2: rod-to-rod, pin-to-plate, wire-in-hole and wire-to-plate configuration. For the rod-to-rod configuration, the diameter of cylindrical rod electrodes was 7 mm and the gap between the two electrodes was 0.75 mm. In the case of the pin-to-plate configuration, a pin electrode that had 7 mm diameter was machined to have a sharp tip with a radius of curvature of approximately 0.12 mm. The diameter of wire electrodes used in the wire-in-hole and wire-to-plate configuration was 0.5 mm and the wire electrodes were placed precisely in the center of the hole. The grounded electrode plate for the pin-to-plate, wire-in-hole and wire-to-plate configuration had the exit hole with a diameter of 2 mm in the center of the grounded plate electrode. The initial gap between the wire and the grounded plate was 0.75 mm for both the pin-to-plate type and the rod-to-rod type SDG.

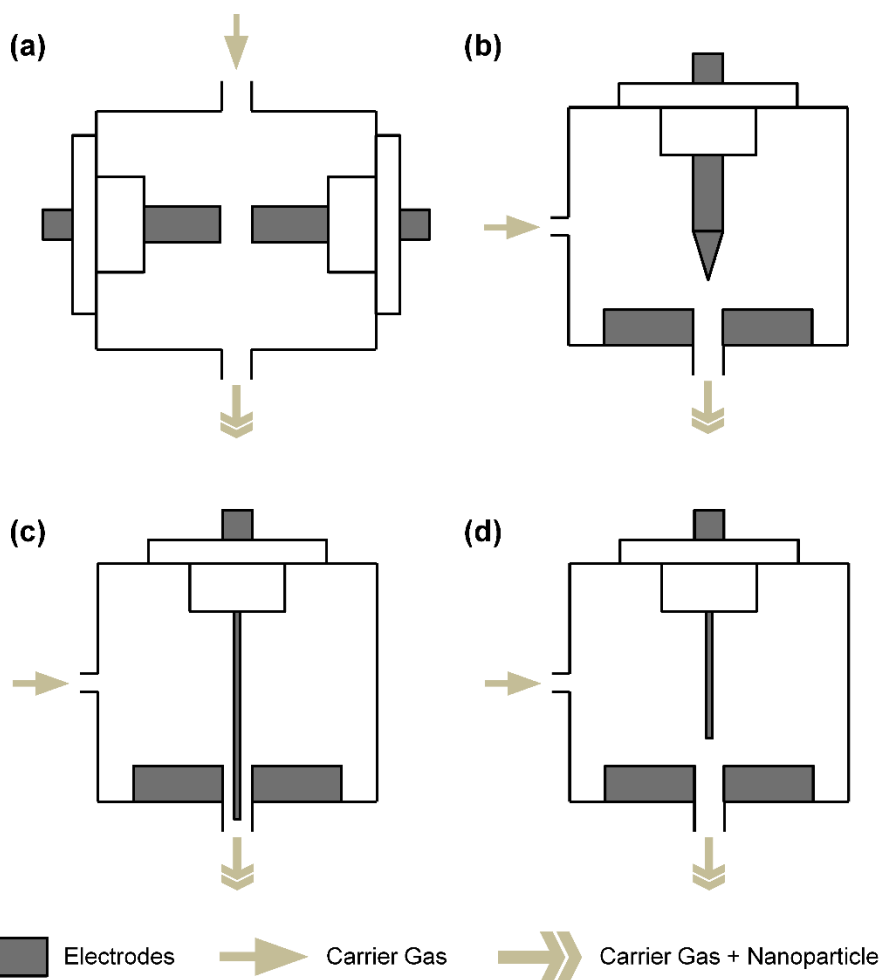


**Figure 3.2. Four different types of spark discharge generator. (a) Rod-to-rod type electrode configuration. (b) Pin-to-plate type electrode configuration. (c) Wire-in-hole type electrode configuration. (d) Wire-to-plate electrode configuration.**

## 3.4. Results and Discussion

### 3.4.1. Long-time Stability of Pin-to-plate and Rod-to-rod Type Spark Discharge Generator

The particle generation and size measurement were carried out continuously for 12 hours for the RR-SDG and the PP-SDG. Figure 3.3 shows the morphologies and size distribution of Ag nanoparticles generated by the rod-to-rod and pin-to-plate type generator. Each sub-figure shows a TEM image sampled before (Fig 3.3(a), 3.3(c)) and after tests which were conducted for 12 hours (Fig 3.3(b), 3.3(d)). SMPS measurements were also carried out every 3 hours to obtain the size distribution data (Figure 3.4).

The RR-SDG generated Ag particles with a wider size distribution than PP-SDG producing less agglomerated particles than RR-SDG. The geometric standard deviation ( $\sigma_g$ ) and the geometric mean diameter ( $d_g$ ) of the RR-SDG were 1.46 and 7.21 nm, respectively. On the contrary, the Ag nanoparticles generated by the pin-to-plate configuration showed a narrower size distribution with lower geometric standard deviation ( $\sigma_g = 1.36$ ) than that of the RR-SDG.

In the case of the PP-SDG, the size distribution of the particles became narrower over 12 hours. The diameter ( $d_g$ ) which was initially 7.32 nm declined gradually to 4.91 nm after 12 hours. The total number concentration of generated particles also decreased from  $1.12 \times 10^8 \text{ \#/cm}^3$  to  $5.70 \times 10^7 \text{ \#/cm}^3$ , as shown in Figure 3.4(b). For the rod-to-rod type generator, the size distribution did not change over time (with a minute difference of 0.21 nm in

diameter produced for 12 hours) as shown in Figure 3.4(a).

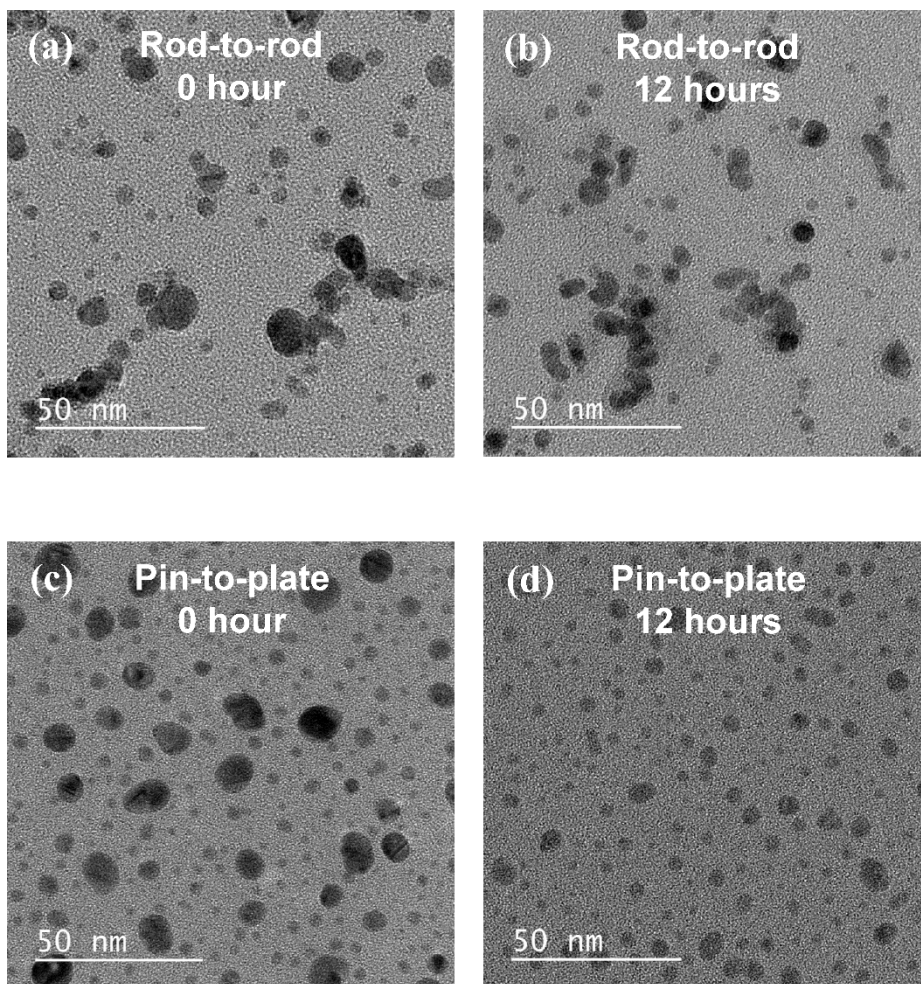


**Figure 3.3. TEM images of Ag nanoparticles generated via two different types of spark discharge generator. (a) Nanoparticles generated by rod-to-rod type SDG at the beginning of the experiment. (b) After 12 hours from the beginning. (c) Nanoparticles generated by pin-to-plate type SDG at the beginning of the experiment. (d) After 12 hours from the beginning.**

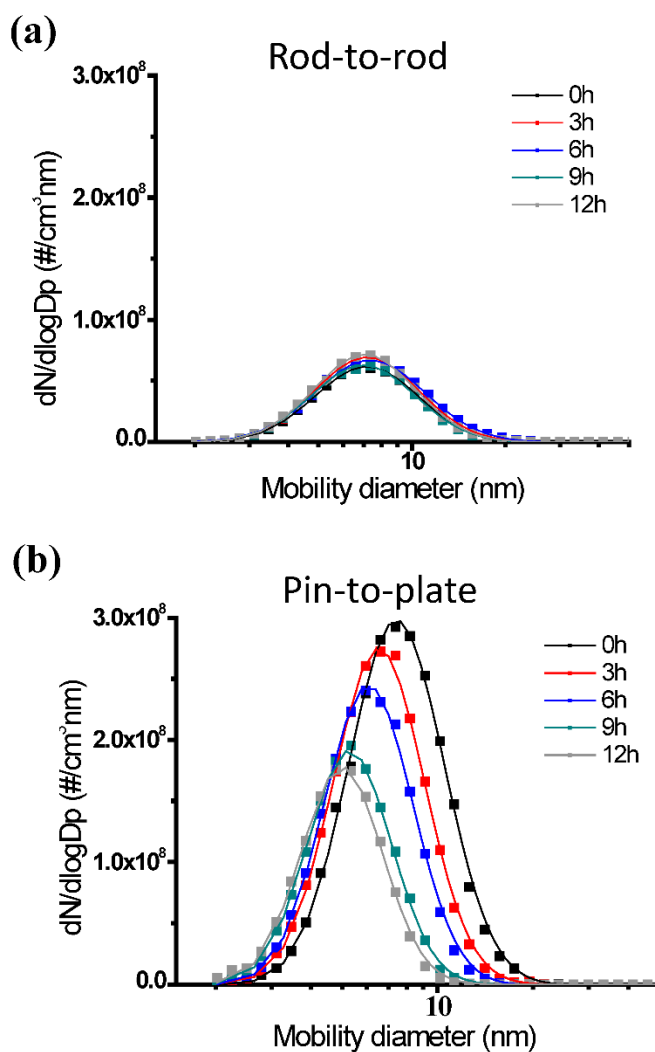


**Figure 3.4. Size distribution of Ag nanoparticles generated via two different types of spark discharge generator measured every 3 hours. (a) rod-to-rod type SDG (b) pin-to-plate type SDG.**

To investigate why the size distribution of PP-SDG generated particles gradually change over time, the tip shape of the pin electrode and spark characteristics were measured. During the spark discharge process, the tip of the pin electrode was eroded, consequently increasing both the radius of curvature of the pin electrode and the distance between the pin and the plate electrode.

Figure 3.5(a) ~ (e) show the changes in the shape of the pin electrode. The sharp pin electrode with 0.12 mm radius of curvature (Figure 3.4(a)) was eroded, thus the gap distance increased and the shape of the tip became blunt. The increase in the radius of curvature of the pin electrode and in the gap distance between the two electrodes affects the discharge characteristics such as discharge voltage and spark frequency. Due to these factors, increased electric field is required to produce sparks between the pin and the plate electrode, so consequently the discharge voltage gets increased. The electric potential of the electrode for RC circuit is defined as  $V_{electrode}(t) = V_{input}(1 - \exp(-t/RC))$ , where  $V_{input}$  is the output voltage of the power supply. As the resistance and the capacitance of the circuit are the same, increased discharge voltage requires more time for spark formation, which leads to a reduction in the spark discharge frequency.

Figure 3.5(f) shows that the measured discharge voltage ( $V_{discharge}$ ) increased from 3 kV at 0 hour to 4.2 kV after 12 hours and the spark frequency decreased from 101 Hz to 55.4 Hz during the time. Single spark

discharge energy which is expressed as  $E_{spark} = (1/2)C_{ext}V_{discharge}^2$ , where  $V_{discharge}$  is the voltage required to cause spark discharge, increased due to larger  $V_{discharge}$ . The spark discharge power is expressed as the product of the spark discharge energy and its frequency. The spark discharge power remained almost constant during the experiment. This means that the spark energy is dispersed in larger volumes as the gap between the two electrodes increases, and less energy is used for the evaporation of the electrodes. The decreased concentration of vaporized metal atoms causes the reduction in particle number concentration. In conclusion, tip erosion and gap distance increase can explain why the PP-SDG produces smaller particles as time passes whereas the RR-SDG produced particles with a constant size distribution regardless of the elapsed time.

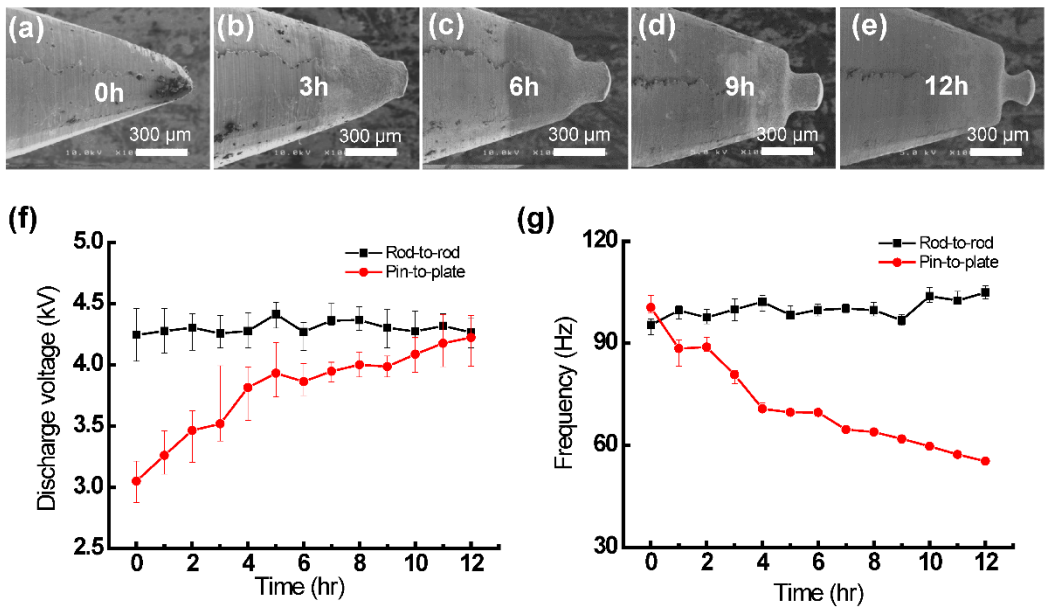


**Figure 3.5. (a) ~ (e) Morphological changes in the tip of the pin electrode in a pin-to-plate type SDG. Changes in (f) spark discharge voltage and (g) frequency versus time for both SDGs.**

### **3.4.2. 12-hour Continuous Generation of Ag Nanoparticles using Wire-in-Hole Type Spark Discharge Generator**

To maintain the fast local carrier gas velocity of the PP-SDG and to suppress the shape change of the positive electrode at the same time, we designed a new type of spark discharge chamber, called the wire-in-hole type spark discharge generator (WH-SDG) which exploits a metal wire located in the center of an exit hole in the plate. The size distribution and the morphology of particles generated by WH-SDG are depicted in Figure 3.6.

The size distribution did not change significantly for 12 hours, with  $d_g$  of 5.5 nm and  $\sigma_g$  of 1.35 maintaining the high number concentration of  $7.34 \times 10^7 \text{ \#/cm}^3$  as measured by an SMPS (Figure 3.6(c)). The TEM images of the particles after 0 hour and 12 hours elapsed confirm that the particle size distribution did not change. The particle size distributions from the TEM image were well consistent with that from SMPS measurements. The geometrical configuration of the WH-SDG can effectively restrain the change in the gap distance, and the changes in the electrode geometry were relatively insignificant. Thus, it was demonstrated that the WH-SDG can generate the unagglomerated nanoparticles with high number concentration consistently for several hours.

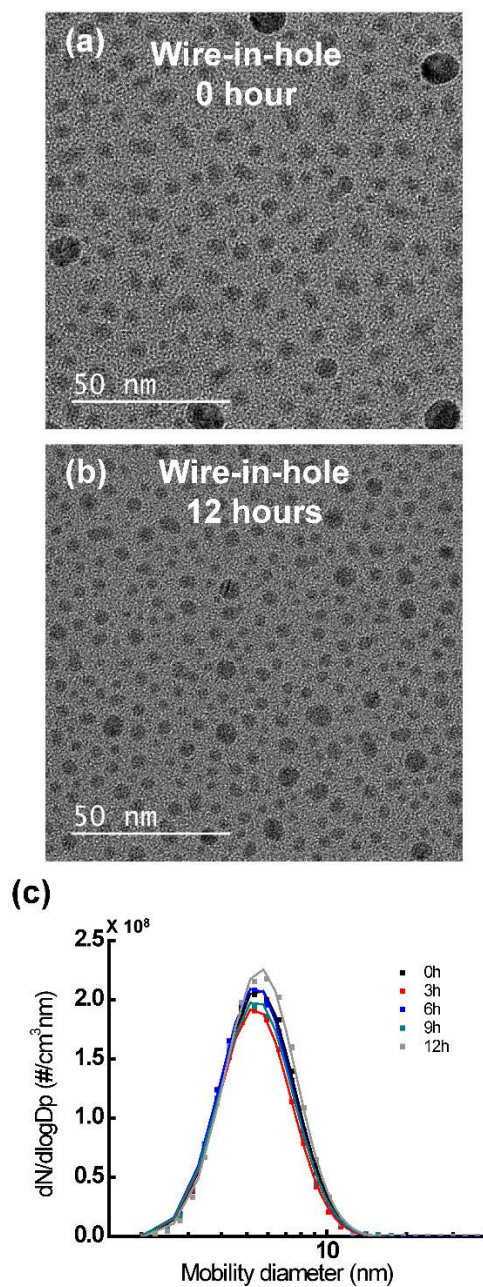


**Figure 3.6. Ag nanoparticles produced via wire-in-hole type SDG. (a) A TEM image of nanoparticles at the beginning. (b) A TEM image of nanoparticles after 12 hours from the beginning. (c) Size distributions of produced nanoparticles measured every 3 hours.**

Figure 3.7 (a) ~ (e) are the images of the wire electrode over time. The wire electrode was worn in the radial direction in the region less than 100  $\mu\text{m}$  from the tip. The spark discharge occurred at various points around the gap of the wire and the grounded plate, which resulted in evenly distributed sparks around the whole surface of the wire electrode. Since the surface area of the electrode subject to erosion is larger than that of the PP-SDG, the WH-SDG can maintain consistent spark discharge characteristics for a longer time. The discharge voltage and the spark frequency of the WH-SDG were measured with an oscilloscope. The discharge voltage ( $V_{\text{discharge}}$ ) stayed at approximately 3.28 kV and the spark frequency was stayed at approximately 90.8 Hz for 12 hours with small fluctuations ( $\pm 0.13$  kV and  $\pm 3.7$  Hz respectively), as shown in Fig 3.7(f) and 3.7(g).

The particle size distributions obtained from various types of the spark discharge generators for 12 hours are plotted in Figure 3.8. In addition to the PP-SDG and the WH-SDG, the wire-to-plate spark discharge generator (WP-SDG, see Figure 3.2(d)) was tested in the experiment to exclude the effects of tip shape changes, and determine the influence of the gap distance changes more clearly. From Figure 3.8(a), the geometric mean diameter of the WH-SDG was maintained at 5.5 nm for 12 hours, but in the case of the PP-SDG and the WP-SDG, the  $d_g$  were decreased from 7.32 to 4.90 nm, and from 7.72 to 4.60 nm, respectively. There was a similar trend for the number concentration. The WH-SDG showed the high number concentration of  $7.34 \times 10^7 \text{ \#/cm}^3$  steadily, while the number concentration of the PP-SDG and the

WP-SDG decreased (Figure 3.8(b)). The total number concentration of the PP-SDG was initially  $1.12 \times 10^8 \text{ \#/cm}^3$  and decreased to  $5.70 \times 10^7 \text{ \#/cm}^3$ . In the case of the WP-SDG, the total number concentration also decreased from  $1.30 \times 10^8 \text{ \#/cm}^3$  to  $3.59 \times 10^7 \text{ \#/cm}^3$ . This shows that the PP-SDG showed decreasing size distribution due to the change in both the tip shape and the gap distance. The increasing gap distance can reduce the particle size and quantity, which can be inferred from the case of the WP-SDG.

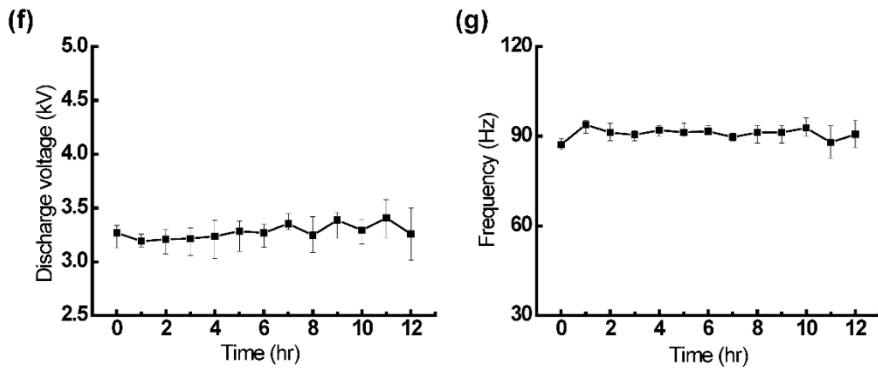
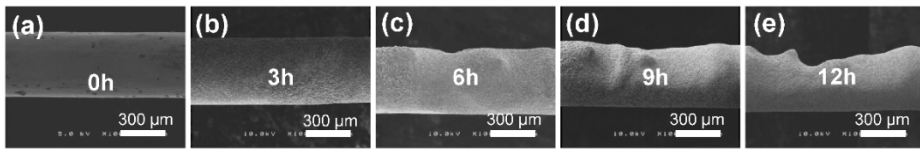


**Figure 3.7. (a) ~ (e) Morphological changes in the wire electrode in wire-in-hole type SDG. Changes in (f) spark discharge voltage and (g) frequency versus time for WH-SDG.**

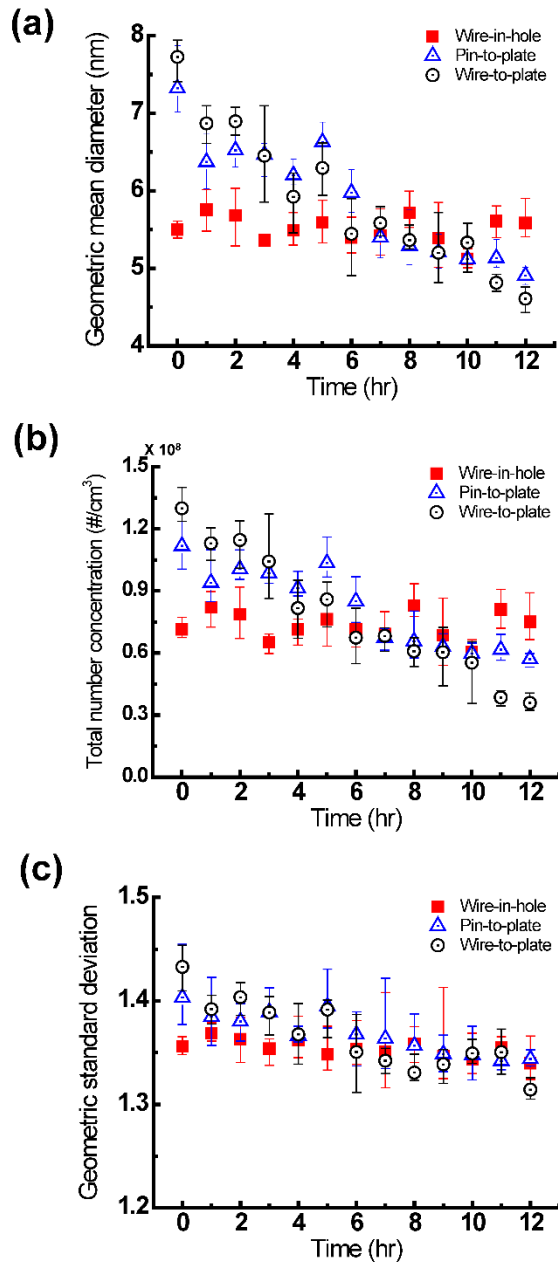


**Figure 3.8. Characteristics of particles generated via WH-SDG, PP-SDG and WP-SDG versus time. (a) Geometric mean diameter. (b) Total number concentration. (c) Geometric standard deviation.**

### 3.4.3. Control of Particle Size Distribution and Synthesis of Various Metal Nanoparticles

In order to utilize the generated nanoparticles as building blocks for nanostructures, it is important to control the size of the generated particles. Thus, we conducted an additional experiment for controlling particle sizes with respect to gas flow rate. Since the increased gas flow rate enhances cooling and dilution rate (Lehtinen and Zachariah, 2002; Tabrizi et al., 2009), the size of the generated nanoparticles is sensitive to the flow rate of the carrier gas. Hence, we measured the size distribution with using different carrier gas flow rates of 1 lpm, 2 lpm and 4 lpm. The discharge voltage and spark frequency of all experiments were maintained during the particle generation.

As shown in Figure 3.9, the particle diameter became smaller as the gas flow rate increased. The average mobility diameter is 6.50 nm, 5.51 nm and 5.15 nm for 1 lpm, 2 lpm and 4 lpm, respectively. For the flow rate of 1 lpm, the particle diameter was obviously larger than that of the case for 2 lpm due to the difference in residence time. But the difference in diameter between 2 lpm and 4 lpm cases was somewhat smaller than that between 1 lpm and 2 lpm cases. The geometric standard deviation of size distribution for 1 lpm condition was 1.38 and was slightly higher than the size distribution of 2 lpm condition ( $\sigma_g = 1.35$ ) as shown in Figure 3.9(c). The difference of  $\sigma_g$  between 2 lpm and 4 lpm cases was much smaller than that between 1 lpm and 2 lpm cases. These results imply that lower flow rate can make larger particles and

may cause agglomeration but the effect is insignificant. (Tabrizi et al., 2009) If the flow rate increases, the diameters of the generated particles become smaller because higher transport velocity in particle growth regions can lower the probability of aggregation (Han et al., 2012).

To show the versatility of the system, other materials such as copper and palladium were used in the WH-SDG as electrodes and the performance evaluation was carried out (Figure 3.10). The experimental conditions were set for generating nanoparticles of 5 nm in diameter. In the case of silver and copper, the electric circuit was comprised of a 5 M $\Omega$  charging resistor and a 2nF external capacitor. For palladium nanoparticles, the resistance and the capacitance of the circuit were 20 M $\Omega$  and 1 nF, respectively. The gas flow rate for Pd particle generation was set at 3 lpm to avoid agglomeration. As shown in Figure 3.10, the size distributions were maintained with little fluctuation. The average geometric standard deviations were 1.35, 1.32 and 1.31 for silver, copper and palladium, respectively.

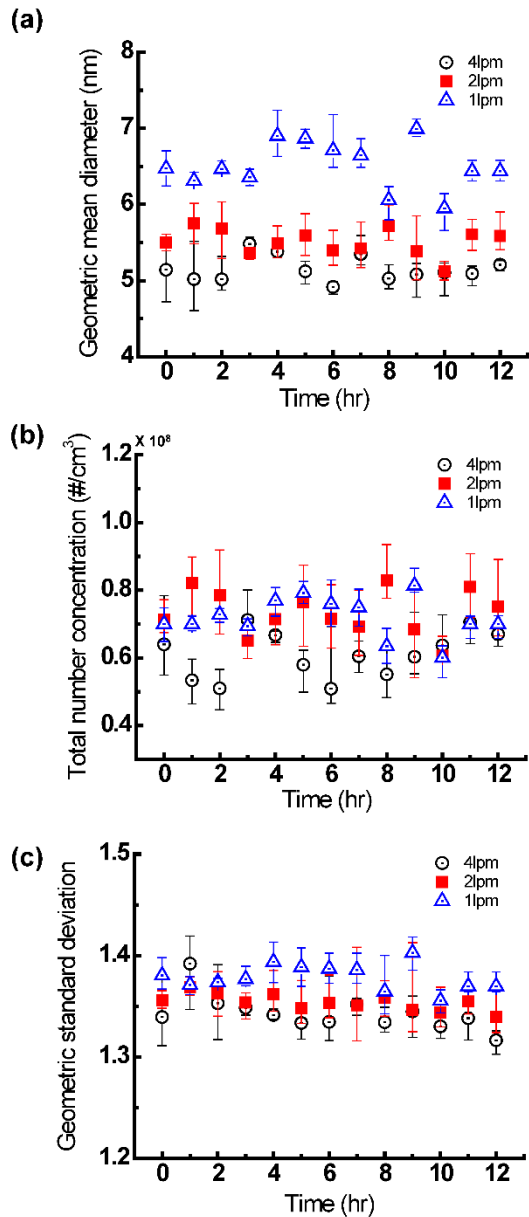


**Figure 3.9. Size distributions of generated nanoparticles with different gas flow rate. (a) Geometric mean diameter. (b) Total number concentration (c) Geometric standard deviation**

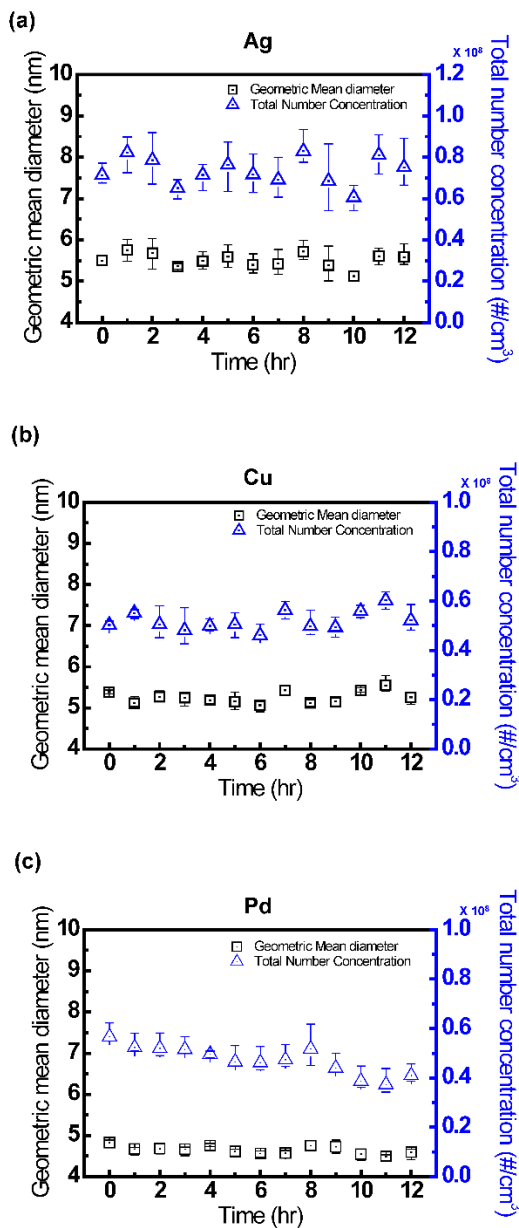


**Figure 3.10. Geometric mean diameters and total number concentrations of various metal nanoparticles generated by WH-SDG over 12 hours. (a) Silver (b) Copper (c) Palladium**

### 3.5. Conclusion

In this study, we developed and evaluated a new type of SDG, in which a metal wire was used as an electrode and the wire electrode was designed to be located in the center of the hole on the grounded plate electrode. Using this wire-in-hole type SDG, it was possible not only to generate unagglomerated nanoparticles with high concentration, but also to show more consistent size distributions for longer operations than the previous pin-to-plate type SDG. The change in the particle size distribution of the PP-SDG over time was found to be due to the changes in the geometry of the pin electrode caused by repetitive spark discharges. The transformed electrode geometry led to the change in spark discharge characteristics such as spark discharge voltage and frequency which could directly influence the generation of nanoparticles. On the other hand, the WH-SDG could effectively suppress the change of gap distance and the shape of the electrode and, hence, maintain its spark discharge properties for a longer time.

Further, to control the diameter of the generated nanoparticles, we carried out experiments varying the flow rates of the carrier gas. As expected, the increasing flow rates from 1 lpm to 4 lpm could produce smaller diameters of nanoparticles. In addition, WH-SDG was able to produce and maintain unagglomerated metal nanoparticles such as Ag, Cu and Pd for a long time.

Thus, the WH-SDG has a novel advantage over other electrode configurations as it can produce small and unagglomerated nanoparticles consistently for several hours. This capability will be especially advantageous

for utilization of produced nanoparticles as building blocks to fabricate nanostructures with complex morphologies.



## **Chapter 4.**

### **Concluding Remarks**

In order to expand the aerosol-based gas phase nanoparticle synthesis method, we established the selective production of magnesium oxide nanoparticles having different morphologies and investigated the optical properties. Moreover, the wire-in-hole type spark discharge generator was introduced to generate sub-10 nm particles consistently.

Using the flame metal combustion method, we discovered the parameters for selectively producing the terraced MgO nanoparticles, which have distinguished morphology and properties compared to general cubic MgO nanoparticles. The flame conditions for producing large proportion of terraced MgO nanoparticles were found and the short flame condition with oxygen carrier gas which was more abundant of oxygen was adequate for producing terrace-shaped MgO particles. With argon carrier gas, otherwise, the cubic MgO nanoparticles were mainly generated. Thus, it is found that the selectivity of produced MgO nanoparticles was determined with changing the flame conditions. For investigating the growth condition of nanoparticles, the particle size distribution of the produced MgO nanoparticles was also measured from electron microscope images. From those results, it could be concluded that optimized conditions for producing terraced and spherical MgO nanoparticles were established.

In Chapter 3, we demonstrated a wire-in-hole type spark discharge generator, which consists of a metal wire electrode and a grounded plate electrode with a hole, could produce sub-10 nm nanoparticles preventing from the change of the particle size distribution over time that exists on the rod-to-

rod and the pin-to-plate type spark discharge method. The newly developed WH-SDG could not only produce nanoparticles unagglomerated primary nanoparticles, but also to show more consistent size distribution for long hours than the previous pin-to-plate type SDG. From the study of long-time operation of the SDG, the change in the geometry of the pin electrode caused by repetitive spark discharge resulted the change in the particle size distribution of the PP-SDG with the lapse of time. The gap size between electrodes and the morphology of electrode geometry could change in spark discharge characteristics such as spark discharge voltage and frequency which could directly influence the generation of nanoparticles. On the other hand, the WH-SDG could effectively suppress the geometrical changes such as gap distance and the shape of the tip of the electrode. Thus the WH-SDG could maintain its spark discharge properties which were highly affected by the geometrical conditions of electrodes for 12 hour generation experiment.

## References

- Altman, I. S., Pikhitsa, P. V., and Choi, M. (2004). Key Effects in Nanoparticle Formation by Combustion Techniques. C. Granqvist, L. Kish, & W. Marlow (Eds.). In *Gas Phase Nanoparticle Synthesis* (pp. 43-67). Springer Netherlands.
- Altman, I. S., Pikhitsa, P. V., Choi, M., Song, H.-J., Nasibulin, A. G., and Kauppinen, E. I. (2003). Zero-phonon lines in the photoluminescence spectra of MgO:Mn<sup>2+</sup> nanocrystals. *Physical Review B*, 68 (12), 125324.
- Aritani, H., Yamada, H., Nishio, T., Shiono, T., Imamura, S., Kudo, M., Hasegawa, S., Tanaka, T., and Yoshida, S. (2000). Characterization of Li-doped MgO catalysts for oxidative coupling of methane by means of MgK-edge XANES. *Journal of Physical Chemistry B*, 104 (44), 10133-10143.
- Arndt, S., Laugel, G., Levchenko, S., Horn, R., Baerns, M., Scheffler, M., Schlogl, R., and Schomacker, R. (2011). A Critical Assessment of Li/MgO-Based Catalysts for the Oxidative Coupling of Methane. *Catalysis Reviews-Science and Engineering*, 53 (4), 424-514.
- Bau, S., Witschger, O., Gensdarmes, F., Thomas, D., and Borra, J. P. (2010). Electrical properties of airborne nanoparticles produced by a commercial spark-discharge generator. *Journal of Nanoparticle Research*, 12 (6), 1989-1995.
- Beaucage, G., Kammler, H. K., Mueller, R., Strobel, R., Agashe, N., Pratsinis, S. E., and Narayanan, T. (2004). Probing the dynamics of nanoparticle growth in a flame using synchrotron radiation. *Nature Materials*, 3 (6),

370-374.

- Buesser, B., and Pratsinis, S. E. (2012). Design of Nanomaterial Synthesis by Aerosol Processes. *Annual Review of Chemical and Biomolecular Engineering, Vol 3, 3*, 103-127.
- Byeon, J. H., Park, J. H., and Hwang, J. H. (2008). Spark generation of monometallic and bimetallic aerosol nanoparticles. *Journal of Aerosol Science, 39* (10), 888-896.
- Cai, H., Chaudhary, N., Lee, J., Becker, M. F., Brock, J. R., and Keto, J. W. (1998). Generation of metal nanoparticles by laser ablation of microspheres. *Journal of Aerosol Science, 29* (5-6), 627-636.
- Cao, C. Y., Qu, J., Wei, F., Liu, H., and Song, W. G. (2012). Superb Adsorption Capacity and Mechanism of Flowerlike Magnesium Oxide Nanostructures for Lead and Cadmium Ions. *ACS Applied Materials & Interfaces, 4* (8), 4283-4287.
- Chae, S., Lee, D., Kim, M. C., Kim, D. S., and Choi, M. (2015). Wire-in-Hole-Type Spark Discharge Generator for Long-Time Consistent Generation of Unagglomerated Nanoparticles. *Aerosol Science and Technology, 49* (7), 463-471.
- Chae, S., Pikhitsa, P. V., Shin, S., Kim, C. H., Jung, S., and Choi, M. (2015). Formation of non-cubic nanoparticles from cubic MgO in intensified self-burning of magnesium (Publication no. arXiv:1511.08554).
- Cho, J., and Choi, M. (2000). Determination of number density, size and morphology of aggregates in coflow diffusion flames using light scattering and local sampling. *Journal of Aerosol Science, 31* (9), 1077-1095.

- Dhal, J. P., Sethi, M., Mishra, B. G., and Hota, G. (2015). MgO nanomaterials with different morphologies and their sorption capacity for removal of toxic dyes. *Materials Letters*, *141*, 267-271.
- Ding, Y., Zhang, G. T., Wu, H., Hai, B., Wang, L. B., and Qian, Y. T. (2001). Nanoscale magnesium hydroxide and magnesium oxide powders: Control over size, shape, and structure via hydrothermal synthesis. *Chemistry of Materials*, *13* (2), 435-440.
- Feldheim, D. L., and Foss, C. A. (2001). *Metal nanoparticles: synthesis, characterization, and applications*: CRC Press.
- Geneste, G., Morillo, J., Finocchi, F., and Hayoun, M. (2007). Primary nucleation processes in binary oxide growth: The case of MgO. *Surface Science*, *601* (23), 5616-5627.
- Grossmann, H. K., Grieb, T., Meierhofer, F., Hodapp, M. J., Noriler, D., Gröhn, A., Meier, H. F., Fritsching, U., Wegner, K., and Mädler, L. (2015). Nanoscale mixing during double-flame spray synthesis of heterostructured nanoparticles. *Journal of Nanoparticle Research*, *17* (4), 1-16.
- Ha, K., Choi, H., Jung, K., Han, K., Lee, J. K., Ahn, K., and Choi, M. (2014). Large-area assembly of three-dimensional nanoparticle structures via ion assisted aerosol lithography with a multi-pin spark discharge generator. *Nanotechnology*, *25* (22).
- Hacquart, R., and Jupille, J. (2009). Morphology of MgO smoke crystallites upon etching in wet environment. *Journal of Crystal Growth*, *311* (21), 4598-4604.
- Han, K., Kim, W., Yu, J., Lee, J., Lee, H., Woo, C. G., and Choi, M. (2012). A study of pin-to-plate type spark discharge generator for producing

- unagglomerated nanoaerosols. *Journal of Aerosol Science*, 52, 80-88.
- Horvath, H., and Gangl, M. (2003). A low-voltage spark generator for production of carbon particles. *Journal of Aerosol Science*, 34 (11), 1581-1588.
- Huang, T., Nallathamby, P. D., and Xu, X.-H. N. (2008). Photostable Single-Molecule Nanoparticle Optical Biosensors for Real-Time Sensing of Single Cytokine Molecules and Their Binding Reactions. *Journal of the American Chemical Society*, 130 (50), 17095-17105.
- Jung, K., Hahn, J., In, S., Bae, Y., Lee, H., Pikhitsa, P. V., Ahn, K., Ha, K., Lee, J. K., Park, N., and Choi, M. (2014). Hotspot-Engineered 3D Multipetal Flower Assemblies for Surface-Enhanced Raman Spectroscopy. *Advanced Materials*, 26 (34), 5924-+.
- Kala, S., Theissmann, R., and Kruis, F. E. (2013). Generation of AuGe nanocomposites by co-sparking technique and their photoluminescence properties. *Journal of Nanoparticle Research*, 15 (9).
- Karch, J., Birringer, R., and Gleiter, H. (1987). Ceramics Ductile at Low-Temperature. *Nature*, 330 (6148), 556-558.
- Kim, H., Kim, J., Yang, H. J., Suh, J., Kim, T., Han, B. W., Kim, S., Kim, D. S., Pikhitsa, P. V., and Choi, M. (2006). Parallel patterning of nanoparticles via electrodynamic focusing of charged aerosols. *Nature Nanotechnology*, 1 (2), 117-121.
- Krinke, T. J., Fissan, H., Deppert, K., Magnusson, M. H., and Samuelson, L. (2001). Positioning of nanometer-sized particles on flat surfaces by direct deposition from the gas phase. *Applied Physics Letters*, 78 (23), 3708-3710.

- Kruis, F. E., Fissan, H., and Peled, A. (1998). Synthesis of nanoparticles in the gas phase for electronic, optical and magnetic applications - A review. *Journal of Aerosol Science*, 29 (5-6), 511-535.
- Lee, D., and Choi, M. (2002). Coalescence enhanced synthesis of nanoparticles to control size, morphology and crystalline phase at high concentrations. *Journal of Aerosol Science*, 33 (1), 1-16.
- Lee, H., Lee, D.-H., Song, Y.-H., Choi, W. C., Park, Y.-K., and Kim, D. H. (2015). Synergistic effect of non-thermal plasma-catalysis hybrid system on methane complete oxidation over Pd-based catalysts. *Chemical Engineering Journal*, 259, 761-770.
- Lee, H., You, S., Pikhitsa, P. V., Kim, J., Kwon, S., Woo, C. G., and Choi, M. (2011). Three-Dimensional Assembly of Nanoparticles from Charged Aerosols. *Nano Letters*, 11 (1), 119-124.
- Lee, J., Altman, I., and Choi, M. (2008). Design of thermophoretic probe for precise particle sampling. *Journal of Aerosol Science*, 39 (5), 418-431.
- Lehtinen, K. E. J., and Zachariah, M. R. (2002). Energy accumulation in nanoparticle collision and coalescence processes. *Journal of Aerosol Science*, 33 (2), 357-368.
- Li, M. J., Guo, W. L., Li, H. J., Dai, W., and Yang, B. H. (2014). Electrochemical bio sensor based on one-dimensional MgO nanostructures for the simultaneous determination of ascorbic acid, dopamine, and uric acid. *Sensors and Actuators B-Chemical*, 204, 629-636.
- Lunsford, J. H. (1995). The Catalytic Oxidative Coupling of Methane. *Angewandte Chemie-International Edition in English*, 34 (9), 970-980.

- Mädler, L., Kammler, H. K., Mueller, R., and Pratsinis, S. E. (2002). Controlled synthesis of nanostructured particles by flame spray pyrolysis. *Journal of Aerosol Science*, 33 (2), 369-389.
- Messing, M. E., Dick, K. A., Wallenberg, L. R., and Deppert, K. (2009). Generation of size-selected gold nanoparticles by spark discharge - for growth of epitaxial nanowires. *Gold Bulletin*, 42 (1), 20-26.
- Meuller, B. O., Messing, M. E., Engberg, D. L. J., Jansson, A. M., Johansson, L. I. M., Norlen, S. M., Tureson, N., and Deppert, K. (2012). Review of Spark Discharge Generators for Production of Nanoparticle Aerosols. *Aerosol Science and Technology*, 46 (11), 1256-1270.
- Mishakov, I. V., Bedilo, A. F., Richards, R. M., Chesnokov, V. V., Volodin, A. M., Zaikovskii, V. I., Buyanov, R. A., and Klabunde, K. J. (2002). Nanocrystalline MgO as a dehydrohalogenation catalyst. *Journal of Catalysis*, 206 (1), 40-48.
- Moodie, A. F., and Warble, C. E. (1971). Electron microscopic investigations of MgO morphology and surfaces. *Journal of Crystal Growth*, 10 (1), 26-38.
- Mullins, W. W. (1957). Theory of Thermal Grooving. *Journal of Applied Physics*, 28 (3), 333-339.
- Muraoka, T., Kashimura, T., and Iizuka, S. (2009). Spherical MgO microparticle deposition by RF impulse discharge with small coaxial electrodes. *Thin Solid Films*, 518 (3), 1012-1015.
- Nagappa, B., and Chandrappa, G. T. (2007). Mesoporous nanocrystalline magnesium oxide for environmental remediation. *Microporous and Mesoporous Materials*, 106 (1-3), 212-218.

- Nalwa, H. S. (1999). *Handbook of Nanostructured Materials and Nanotechnology, Five-Volume Set* (Vol. 3): Academic Press.
- Newman, R. N., and Payne, J. F. B. (1987). The Anomalous Brightness of Magnesium Air Flames. *Combustion and Flame*, 68 (1), 31-41.
- Pacchioni, G., Clotet, A., and Ricart, J. M. (1994). A theoretical study of the adsorption and reaction of SO<sub>2</sub> at surface and step sites of the MgO(100) surface. *Surface Science*, 315 (3), 337-350.
- Pacchioni, G., and Maria Ferrari, A. (1999). Surface reactivity of MgO oxygen vacancies. *Catalysis Today*, 50 (3-4), 533-540.
- Park, K. T., Farid, M. M., and Hwang, J. (2014). Anti-agglomeration of spark discharge-generated aerosols via unipolar air ions. *Journal of Aerosol Science*, 67, 144-156.
- Patil, K. C., Aruna, S. T., and Mimani, T. (2002). Combustion synthesis: an update. *Current Opinion in Solid State and Materials Science*, 6 (6), 507-512.
- Pfeiffer, T. V., Feng, J., and Schmidt-Ott, A. (2014). New developments in spark production of nanoparticles. *Advanced Powder Technology*, 25 (1), 56-70.
- Pikhitsa, P. V., Kim, C., Chae, S., Shin, S., Jung, S., Kitaura, M., Kimura, S., Fukui, K., and Choi, M. (2015). Two-band luminescence from an intrinsic defect in spherical and terraced MgO nanoparticles. *Applied Physics Letters*, 106 (18), 183106.
- Portillo, R., Lopez, T., Gomez, R., Bokhimi, Morales, A., and Novaro, O. (1996). Magnesia synthesis via sol-gel: Structure and reactivity. *Langmuir*, 12 (1), 40-44.

- Pratsinis, S. E. (1998). Flame aerosol synthesis of ceramic powders. *Progress in Energy and Combustion Science*, 24 (3), 197-219.
- Pratsinis, S. E. (2010). Aerosol-based Technologies in Nanoscale Manufacturing: from Functional Materials to Devices through Core Chemical Engineering. *Aiche Journal*, 56 (12), 3028-3035.
- Rao, N. P., Tymiak, N., Blum, J., Neuman, A., Lee, H. J., Girshick, S. L., McMurry, P. H., and Heberlein, J. (1998). Hypersonic plasma particle deposition of nanostructured silicon and silicon carbide. *Journal of Aerosol Science*, 29 (5-6), 707-720.
- Raouf, F., Taghizadeh, M., and Yousefi, M. (2013). Activity enhancement of Li/MgO catalysts by lithium chloride as a lithium precursor for the oxidative coupling of methane. *Reaction Kinetics Mechanisms and Catalysis*, 110 (2), 373-385.
- Refson, K., Wogelius, R. A., Fraser, D. G., Payne, M. C., Lee, M. H., and Milman, V. (1995). Water chemisorption and reconstruction of the MgO surface. *Physical Review B*, 52 (15), 10823-10826.
- Roth, C., Ferron, G. A., Karg, E., Lentner, B., Schumann, G., Takenaka, S., and Heyder, J. (2004). Generation of ultrafine particles by spark discharging. *Aerosol Science and Technology*, 38 (3), 228-235.
- Scheer, E. (2010). *Molecular electronics: an introduction to theory and experiment* (Vol. 1): World Scientific.
- Schwyn, S., Garwin, E., and Schmidtott, A. (1988). Aerosol Generation by Spark Discharge. *Journal of Aerosol Science*, 19 (5), 639-642.
- Shluger, A. L., Sushko, P. V., and Kantorovich, L. N. (1999). Spectroscopy of low-coordinated surface sites: Theoretical study of MgO. *Physical*

*Review B*, 59 (3), 2417-2430.

Siegel, R. W. (1993). Nanophase Materials Assembled from Atom Clusters. *Materials Science and Engineering B-Solid State Materials for Advanced Technology*, 19 (1-2), 37-43.

Stankic, S., Cottura, M., Demaille, D., Noguera, C., and Jupille, J. (2011). Nucleation and growth concepts applied to the formation of a stoichiometric compound in a gas phase: The case of MgO smoke. *Journal of Crystal Growth*, 329 (1), 52-56.

Stavale, F., Nilius, N., and Freund, H.-J. (2012). Cathodoluminescence of near-surface centres in Cr-doped MgO(001) thin films probed by scanning tunnelling microscopy. *New Journal of Physics*, 14 (3), 033006.

Sterrerr, M., Heyde, M., Novicki, M., Nilius, N., Risse, T., Rust, H. P., Pacchioni, G., and Freund, H. J. (2006). Identification of color centers on MgO(001) thin films with scanning tunneling microscopy. *Journal of Physical Chemistry B*, 110 (1), 46-49.

Strobel, R., and Pratsinis, S. E. (2007). Flame aerosol synthesis of smart nanostructured materials. *Journal of Materials Chemistry*, 17 (45), 4743-4756.

Sung, H., Lee, J., Han, K., Lee, J. K., Sung, J., Kim, D., Choi, M., and Kim, C. (2014). Controlled positioning of metal nanoparticles in an organic light-emitting device for enhanced quantum efficiency. *Organic Electronics*, 15 (2), 491-499.

Tabrizi, N. S., Ullmann, M., Vons, V. A., Lafont, U., and Schmidt-Ott, A. (2009). Generation of nanoparticles by spark discharge. *Journal of Nanoparticle Research*, 11 (2), 315-332.

- Thimsen, E., and Biswas, P. (2007). Nanostructured photoactive films synthesized by a flame aerosol reactor. *Aiche Journal*, 53 (7), 1727-1735.
- Tricoli, A., and Pratsinis, S. E. (2010). Dispersed nanoelectrode devices. *Nat Nano*, 5 (1), 54-60.
- Wang, J. A., Novaro, O., Bokhimi, X., Lopez, T., Gomez, R., Navarrete, J., Llanos, M. E., and LopezSalinas, E. (1997). Structural defects and acidic and basic sites in sol-gel MgO. *Journal of Physical Chemistry B*, 101 (38), 7448-7451.
- Yang, S., Jang, Y. H., Kim, C. H., Hwang, C., Lee, J., Chae, S., Jung, S., and Choi, M. (2010). A flame metal combustion method for production of nanoparticles. *Powder Technology*, 197 (3), 170-176.
- Yang, S. S., Yi, J. H., Son, S., Jang, J., Altman, I. S., Pikhitsa, P. V., and Choi, M. (2003). Fragmentation of Fe<sub>2</sub>O<sub>3</sub> nanoparticles driven by a phase transition in a flame and their magnetic properties. *Applied Physics Letters*, 83 (23), 4842-4844.
- You, S., Han, K., Kim, H., Lee, H., Woo, C. G., Jeong, C., Nam, W., and Choi, M. (2010). High-Resolution, Parallel Patterning of Nanoparticles via an Ion-Induced Focusing Mask. *Small*, 6 (19), 2146-2152.
- Zachariah, M. R., Mcmillin, B., and Shull, R. D. (1995). Synthesis and in-Situ Characterization of Superparamagnetic Nanocomposites from Vapor-Phase Condensation. *Abstracts of Papers of the American Chemical Society*, 210, 18-Pmse.
- Zolotko, A. N., Poletaev, N. I., Vovchuk, J. I., and Florko, A. V. (2004). Nanoparticle Formation by Combustion Techniques. In *Gas Phase Nanoparticle Synthesis* (pp. 123-156). Springer.

# 화염금속연소법과 스파크방전법을 이용한 기능성 나노입자 합성

서울대학교 대학원 기계항공공학부

채 석 병

나노입자는 벌크 상태의 물질과는 다른 고유의 특성을 갖고 이러한 나노입자를 합성하기 위한 기법은 나노기술의 주된 연구분야 중 하나이다. 다양한 종류의 나노재료가 전자, 광학, 촉매, 에너지 및 바이오 공학 분야에 응용되고 있어 우수한 특성을 갖는 나노재료의 효율적인 합성 기법에 대한 연구가 필요가 높아지고 있다. 현재까지 다양한 종류의 나노입자 합성 기법이 보고되었으며, 기능성 나노재료의 합성을 위해 적용되고 있다. 이 중, 에어로졸 기반의 기상 합성법은 이러한 나노재료를 합성하기에 보다 청정하고 효율적인 기법 중 하나로 여겨진다. 이는 현존하는 졸-겔 방법에서 만족시키기 어려운 부분으로, 전기 방전, 레이저 어블레이션, 증발-응축, 화염 연소법 등의 많은 에어로졸 기반의 기상합성법이 소개되고, 나노입자를 합성하는데 응용되고 있다. 이를 바탕으로, 본 연구에서는 형상과 특성이 다른 산화물 나노입자를 선택적으로 합성할 수 있는 화염 금속 연소법과 10 nm 이하의 나노입자를 장시간 안정적으로 생산할 수 있는 새로운 스파크 방전 장비를 이용한 스파크 방전법을 설명한다.

화염금속연소법은 기존의 수용액 상태의 전구체가 아닌 고체 분말 상태의 금속 분말을 전구체로 사용하여 이를 초고온의 수소-산소 확산화염에 주입하여 나노입자를 합성하는 기법으로, 손쉽고 효율적으로 나노입자를 합성할 수 있는 에어로졸 기반의 기상합성법이다. 화염금속연소법으로 산화아연, 산화마그네슘, 산화주석 등의 다양한 산화물 나노입자를 제조할 수 있다. 이 기법을 활용하여 산화 마그네슘 입자를 합성하였을 때, 기존의 산화마그네슘과 다른 음극발광 특성을 갖는 테라스/구형 산화마그네슘 나노입자가 생성되는 것을 발견하였다. 합성된 산화마그네슘 입자의 화염 위치별 입자 크기 분포를 측정하여 두 종류의 나노입자의 성장 메커니즘이 일반적인 정방형 입자와 다른 표면결함에 의한 빠른 성장임을 규명하였으며, 다른 종류의 이송 기체를 사용하여 산화마그네슘 나노입자를 합성하면 정방형 입자와 테라스/구형 입자가 생성되는 비율을 제어할 수 있음을 발견하였다. 또한 산화마그네슘 입자에 전이금속을 도핑하여, 금속 입자의 위치에 따라 음극 발광 특성이 달라지는 특성을 조사하였다.

스파크 방전법은 10 nm 이하의 입자를 제조할 수 있는 적절한 방법으로 여겨지고 있으며, 특히 나노패턴 제조를 위한 구성 입자로 활용되는 하전된 나노입자를 효율적으로 제조할 수 있는 기법이다. 스파크 방전은 방전 전극의 구성에 따라 입자가 생성되는 양상이 달라지는데, 일반적으로 사용되는 봉-봉 구조의 경우 국부적으로 생성 후의 유속이 적어 의도하지 않은 응집현상이 발생하는 것이 불가피하다. 반면에, 이전에 보고된 핀-판 구조의 경우 응집되지 않은 입자의 합성이 가능하나, 시간이 경과됨에 따라 전극이 마모되어 스파크 특성이 변하고 입자 크기분포가 변하는 현상이 있다. 이러한 문제를 해결하기 위해 선 전극을 판 전극의 가운데에 위치한 입자 출구에 위치시킨 새로운 전극 구조를

사용한 스파크 방전 장비를 개발하였다. 이는 전극의 기하학적인 변화와 전극간 거리 변화를 효율적으로 억제시켜 일정한 스파크 방전 전압과 방전 주파수를 장시간 유지하는 것이 가능하였고, 따라서 12시간 동안 입자의 크기분포 변화가 없이 안정적으로 나노입자를 발생시켰다. 이를 이용하여 입자 크기의 제어 실험 및 은, 구리, 팔라듐 등의 다양한 종류의 금속 나노입자를 제조하는 실험을 수행하였다.

**주요어:** 에어로졸기반 나노입자 합성; 화염금속연소법; 테라스 산화마그네슘 입자; 스파크 방전법; 선-구멍 구조 스파크 방전 입자 발생기

**학 번:** 2008-22895